Development of Lignin Carbon Fiber and Reinforced Composites

A Thesis Presented for the

Master of Science

Degree

The University of Tennessee, Knoxville

Nathan Kieran Meek

December 2016

DEDICATION

My master's work is dedicated to my loving family who unconditionally supported me throughout graduate school. Although I have so many to be grateful for, I want to thank my mother, Kristen, for always making sure I was well fed and taken care of, my father, John, for listening to my crazy theories about carbon fiber, and finally my closest friend and brother, Sean, for being the best brother anyone could ask for. They have been amazing during this process and I cannot thank them enough.

ACKNOWLEDGEMENTS

The work presented herein would not have been possible without the consistent guidance and wisdom from my principal adviser, Dr. Dayakar Penumadu who has been crucial to my development as a graduate student and engineer. Additionally, Dr. David Harper, whom I consider a great professor and mentor, has always given me helpful advice throughout my research. Dr. Kevin Kit, my undergrad adviser, helped and mentored me throughout my undergraduate career. I also want to thank Ken Thomas and Larry Roberts for their expertise and help in the CEE workshop. Finally, my colleagues in Dr. Penumadu's lab and the Center for Renewable Carbon have been an absolute joy to work alongside of for several years.

ABSTRACT

The aim of this work is to develop lignin carbon fiber for composite applications. This included mechanical testing of single lignin carbon fiber (LCF), interfacial shear strength determination for LCF-resin systems using single fiber fragmentation, x-ray diffraction for the evaluation of microstructural parameters, and finally composite manufacturing and testing. Through these focused areas of analysis, the carbon fiber is thoroughly characterized and composite performance is evaluated. This effort was a collaboration with the Center for Renewable Carbon (CRC) and the Civil and Environmental Engineering Department. LCF produced by the CRC resulted in fibers having tensile strength of 250-800 MPa and Young's modulus of elasticity of 29-40 GPa. The produced LCF consistently demonstrated superior interfacial shear strength properties when compared with commercially available PAN based carbon fibers. This finding is likely due to the functional groups remaining on the fiber surface because LCF is processed at a lower temperature relative to PAN based carbon fibers and there are fundamental differences in the molecular chemistry and arrangement of the precursor.

TABLE OF CONTENTS

LIST OF TABLES

LIST OF FIGURES

LIST OF SYMBOLS

Å	Angstrom
d	diameter (fiber)
σf	failure stress from Weibull statistics
τ_{IFSS}	Interfacial Shear Strength
lc	critical fragmentation length from SFFT
$\bar{l}$	average measured fragmentation length from SFFT
ε	engineering strain
E_0	initial Young's modulus at zero strain
γ	linear dependency of modulus on strain
$\mu \pm \sigma$	mean ± standard deviation (in tables)
E_M	Young's modulus of matrix material
V_M	volume fraction of matrix material
E_F	Young's modulus of fiber reinforcement
V_F	volume fraction of fiber reinforcement
E_c	predicted composite modulus
β	FWHM of the peak of interest
θ	theta, Bragg angle
K	constant for La, Lc determination
n	integer (0, 1, 2, 3…)
d'	d-spacing
χ	chi, WAXS diffraction axis
λ	lambda, wavelength
Lc	stacking height of graphene planes
La	average crystallite size
s	scattering, momentum length
B_{obs}	Observed breadth of the intensity
Bp	instrumental broadening by the primary beam

<L>	average length of scatterer or domain
Bg	true integral breadth of the orientation distribution
I(Q)	intensity at q
$\Delta\rho_k$	scattering contrast
$S_k(Q)$	structure factor
D	particle dimension
$F_k(Q, D_{ik})$	scattering form factor
$V_k(D_{ik})$	particle volume
$f_k(D_{ik})$	volume size distribution in k populations
ΔD	delta particle dimension
N_T	total number of scatterers
Ψ(D)	probability of occurrence of a scatterer of size D
gp	degree of graphitization
$d_{(002)}$	d-spacing of (002) plane
q_x	flow rate
$\delta P/\delta x$	differential in pressure as a function of distance, x
A	cross-sectional area
k_x	permeability at distance, x
μ	resin viscosity

INTRODUCTION

This brief section serves to introduce each area of testing including theory and analysis. Detailed explanations and results are presented in Chapters I-IV and written as articles intended for publication and, therefore, are stand-alone. Background and development of experimental materials is contained within each chapter and not presented in the introduction. The work presented here in the introduction focuses on the characterization techniques.

Single Fiber Mechanical Testing

As a crucial part of the development of lignin carbon fiber (LCF), the mechanical properties for each batch of LCF must be evaluated to determine the impact of various processing parameters, feedstocks, and additional treatments. Through testing and tracking, the LCF can be improved overtime with novel processing techniques and treatments. In this study, single fibers were analyzed for many reasons, including the lack of LCF tows. Tow testing is typical for industry in evaluating the mechanical performance of carbon fiber. If LCF tows were available, single fiber testing would still be preferred. With tow testing, there are several variables that can skew reported mechanical properties and improvements in the process maybe overshadowed by these defects or errors. Some common defects include dry spots (not fully impregnated) in tows, intra-tow effects (fibers not fully tensioned, aligned), and depending on the quality of resin used, early failure due to poor preparation leading to crack initiation and propagation. With single fiber testing, these variables are removed from the equation and small improvements in the process can be detected.

MTS Nano Bionix UTM

For testing and evaluating single fibers, a MTS Nano Bionix universal testing machine (UTM) system was employed. The UTM was modified to specifically test single fiber samples (grips, template mounting procedure), which is discussed in detail in the following section. The UTM is an ideal testing platform in the assessment of LCF mechanical properties due to its very high resolution. Within the UTM is the Nano-Mechanical Actuating Transducer (NMAT), which utilizes a capacitance gage, electromagnetic coil, and leaf springs to achieve ultra-high resolutions (Figure 11, Chap. 1). The NMAT sits in the base of the UTM while the top moving crosshead is an optically encoded stepper motor with 35 nm resolution [1]. The system applies force to the sample by controlling the position of the electromagnetic coil. The capacitance gauge measures vertical displacement of the electromagnetic coil and the UTM uses a PID feedback loop to keep the coil in a 'fixed' displacement. Thus, the system can apply load, either tension or compression, to the sample by controlling the position of the electromagnetic coil. The moving crosshead applies displacement to the sample, thus the system can control strain rate and loading very accurately.

Continuous Stiffness Measurement

The UTM has several unique capabilities, including the ability to determine static and dynamic properties within a single test. The NMAT can apply small, in-situ sinusoidal loads to the sample, which are superimposed onto the restoring force required to keep the electromagnetic coil in the needed position for loading. This sinusoidal loading is similar to the mechanism of a Dynamic Mechanical Analysis (DMA). Thus, two tests are performed during a single cycle: (1) small sinusoidal loading and (2) global tension or compression. Because of this, the UTM is

ideal in testing of carbon fiber and polymers in general. Details and equations regarding the UTM and Continuous Stiffness Measurement are found in Kant [1, 2].

Single Fiber Grip System and Sample Preparation

Kant and Penumadu developed a sample preparation procedure for testing single fibers based on ASTM C1557-03 and ISO 11566:1996. Typically, single fibers are mounted on a cardboard template and then transferred to a testing apparatus. There are many issues with using this mounting procedure regarding the use of a non-rigid template. Non-rigid templates are an issue with testing single fibers because (1) they can create bending moments about the edge of the fiber during testing and (2) the samples are difficult to handle without putting stress on the fibers. To overcome this issue, Kant moved to a rigid template testing system, which is described in detail in Kant, Penumadu [1, 2]. This system is ideal for evaluating LCF because LCF is relatively weak and brittle (<600 MPa failure stress, 40 GPa modulus). The UTM saves time and produces highly accurate results whereas using cardboard/plastic templates would be laborious, inefficient, and produce results with a large standard deviation [1, 2].

Fiber/Resin Interface Adhesion Characterization

In composite design and development, the adhesion between the fiber and resin is crucial to the overall composite performance. The ability of the composite to transfer stress from the resin matrix material to the fiber is key to achieving high mechanical properties. Therefore, evaluating this adhesion, also known as the interfacial shear strength (IFSS), is decidedly important in considering a fiber/resin system for a specific application. Currently, there are several different methods in evaluating interface shear strengths between fiber and resin matrix materials in fiber-reinforced composites. Microdroplet, single fiber fragmentation, pull-out, and

nanoindentation are to name a few. This area within composite technology is quite challenging, as all of these techniques have difficulty in quantifying the interfacial shear strength due to unusual force balance equations, variables in sample preparation, and the fact that they are time consuming. Currently, the single fiber fragmentation test (SFFT) is the most common procedure for evaluation of fiber-resin interfacial properties. [3-5].

Single Fiber Fragmentation

Single Fiber Fragmentation is the determination of fiber/resin interfacial shear strength through the tensile loading of single fiber composites (SFC). The SFC is a cured resin sample in a dogbone shape with an imbedded fiber in the middle neutral axis. As the SFC is loaded, stress is transferred to the fiber causing it to fracture. With increasing strain, fractures along the fiber increase. When the fiber fractures do not increase with additional strain, the sample reaches a point known as 'saturation'. While under loading, the number of fractures and the length of those fractures are measured. Once these measurements are complete, the IFSS can be determined using the following equation:

$$\tau_{IFSS} = \frac{\sigma_f * d}{2 * l_c} \quad [1]$$

In equation 1, τ_{IFSS} is the interfacial shear strength, σf is the failure stress based on Weibull statistics, d is the fiber diameter, and lc is the critical fiber length. Figure 1 shows the derivation of the equation. The interface boundary must be consistent leading to a force balance equation where the strain along the fiber must equal the stress experienced by the fiber.

The fiber length used in the equation for interfacial shear strength comes from the critical fiber length, not the measured fiber length. Critical fiber length is calculated from the average measured fiber length.

$$l_c = \frac{4}{3}\bar{l} \quad [2]$$

This difference in critical fiber length and average measured fiber length stems from definitions within SFFT. The stress distribution along the fiber is demonstrated in Figure 2 which shows that as stress increases, the fiber will break to a length of ~$2x_0$ which is the length required to reach ultimate tensile strength [6]. This fracture mechanism continues until all fiber lengths are between x_0 and $2x_0$. Thus, on average the average measured fragmentation length will fall between x_0 and $2x_0$ and therefore $\bar{l}$ is equivalent to 3/2 x_0.

Others have pointed out that the assumptions made in the Kelly model can lead to inconsistencies, and because of this, improvements can be made [7, 8]. Under the Kelly model, the failure stress, σ_f, is assumed to be linearly related to the fragmentation length. This is not always the case as specimens can strain harden or soften leading to nonlinear behavior [1]. In addition, there are many variables in the SFFT and therefore, it is generally accepted that for accurate results more than ten samples need to be tested per fiber/resin system [3]. Because of this, it is important to understand that the reported IFSS is an average and large standard deviations can exist.

There are a few things to consider when performing the SFFT. First, the ductility of the matrix material must be considerably more than the ductility of the fiber. Typically, chosen resins for matrix materials are close to five times more elastic than the embedded fiber. This ensures that the fiber will saturate with fractures before the matrix begins to fail. Second, this technique only works for optically transparent resins and, therefore is quite limited in that sense.

Epoxies, vinyl esters, and other resins that are opaque cannot be used with SFFT. Other methods, such as the pull-out or microdroplet, must be used for these resin systems, however, these techniques have numerous variables in sample preparation and therefore are subject to errors of their own.

Structural Property Determination Through X-ray Diffraction

X-ray Diffraction (XRD) is a common technique used in the analysis of structural features of various samples. XRD can give information regarding crystallinity, orientation, pore structure, and other structural parameters. There are several fields of XRD that give different kinds of information (grazing incidents, powder, texture, etc.); however, small and wide-angle transmission diffraction is used for the texture analysis of carbon fiber.

X-rays are electromagnetic radiation similar to ambient light but with a much shorter wavelength (0.5-2.5 Å). Typically, X-rays are produced by deaccelerating electrons with sufficient kinetic energy using an X-ray tube with a source of electrons and two metal electrodes. The voltage (25,000+ volts) across the electrodes causes the electrons to bombard the anode with very high velocity [9]. As the electrons deaccelerate in a fraction of a second, X-rays are emitted at the point of impact. The produced X-rays radiate in all directions and are refined to a point or small area through a series of masks and slits. Figure 3 shows a typical set-up for carbon fiber analysis including incident and diffracted optics.

Once the X-rays interact with the material, they follow Bragg's Law (eq. 3), which describes the spacing of crystalline planes or domains relative to an incoming beam and the resultant diffracted beam based on d-spacing.

$$n\lambda = 2d'\sin\theta \quad [3]$$

In equation 3, λ is the wavelength of diffraction (~1.54Å for CuKα), d` is the d-spacing or spacing between crystalline planes, θ is the angle of the incoming beam, and n is an integer also known as the order of diffraction which is equal to the number of wavelengths in the path difference [9]. The diffracted beam path must be a certain number of wavelengths or the interference is deconstructive and therefore not visible in the diffraction pattern. Based on Bragg's Law, it is easy to see that as the incoming diffraction angle becomes smaller, the spacing of the diffracted object or domain becomes larger. Therefore, XRD is separated into groups based on the diffraction angles to help with analysis (wide- and small-angle diffraction). This distinction between small and wide-angle diffraction is helpful because equations, analysis techniques, and diffracting objects are vastly different between the two [9-16].

Wide-Angle Diffraction of Carbon Fibers

Wide-angle X-ray Diffraction (WAXS) normally means diffraction angles larger than 10° 2θ. As previously discussed, with increasing 2θ objects diffracting become much smaller. Therefore, WAXS is used to identify and characterize crystalline regions or objects below ~50 nm. Carbon fibers form a structure that is similar to graphite known as turbostratic carbon. Planes of graphene are stacked in an ABA structure very comparable to a hexagonal close packed (HCP) lattice structure (Figure 4 and 5). The turbostratic structure of carbon fiber tends to contain more defects, and planes are not perfectly orientated relative to each other or the fiber axis. Thus, carbon fibers have typically a lower modulus than graphite.

In characterizing the morphology of carbon fibers, WAXS is mainly used to determine the (1) d-spacings of the (100) and (002) planes, (2) "stack height" of the graphene planes, L_c,

(3) the average crystallite size, L_a, and finally (4) the orientation of graphene planes within the fiber, however, it can also determine percent crystallinity, fiber orientation factors, and residual strain/stress [10]. Lc and La are calculated based on the position and full-width half-max of the (100) and (002) peaks [11]. Thus, the crystalline structure of the carbon fiber can be described by (100) and (002) planes (Figure 5). The procedure outlined here is modeled after Spruiell [10]. The parameters listed above can be determined from three basic scans: (1) 2θ scan around the (002) peak close to 25-26°, (2) full χ scan about the (002) peak, and (3) 2θ scan around the (100) peak near 43° at χ of 90°.

In addition to information about the crystalline regions (or lack thereof), the orientation of the graphene planes relative to the fiber axis can be determined from scans in Chi/Psi. As the planes become more aligned to the fiber axis, the resultant diffraction pattern is less broad indicating a smaller peak in Chi. Figure 6 displays an example wide-angle diffraction pinhole pattern to demonstrate this effect. As the planes orient, the breadth of the (002) peak in χ increases. To quantify this, the sample is varied in χ with the diffractometer held in 2θ at the (002) peak.

Small-Angle Diffraction (SAXS) of Carbon Fibers

Small-angle diffraction of carbon fibers scans for larger scattering domains such as amorphous regions or microvoids. The two analysis techniques selected to process that data are (1) Ruland's Streak Analysis developed specifically to process SAXS data from carbon fiber [12-14] and (2) Irena Analysis using Igor software which is an adopted standard practice by industry [15-16].

Ruland's Streak Analysis (RSA)

Ruland developed an analysis technique to determine the relative size and length of a diffracting pore based on the breadth of the pinhole pattern as the scattering length (denoted as s) increases. The original intension in exploring an alternative analysis method for fiber materials was to separate misorientation and size effects in the pinhole pattern [12-14]. It was discovered that orientation distribution can be described by fitting the intensity of the reflection with Gaussian functions as s increases. Ruland expanded on this concept and adapted this technique for fibrous materials. In addition, he pointed out that this technique only works with significant extension in the radial direction indicating that this technique begins to fall apart when applied to spherical diffracting domains [13].

Since the pole figure or pinhole pattern is in reciprocal space, the integral breadth as a function of s_{12} (perpendicular to fiber axis) of an ideal sample with perfect alignment would be equivalent to the inverse of average domain length (Figure 7 (a)). As misorientation is introduced, the breadth of the streak increases along s_{12}. The orientation distribution broadens through angular convolution and narrows with increasing s (Figure 7). Therefore, RSA functions by capturing the observed breadth at each s (B_{obs}) and then comparing this against s through fitting Gaussian distributions to the intensity. After the breadth is determined, the average scattering domain length is calculated from equation 4

$$s^2 {B_{obs}}^2(s) = {B_p}^2 + \frac{1}{\langle L \rangle^2} + s^2 {B_g}^2 \quad [4]$$

In equation 4, s is the scattering magnitude, B_{obs} is the observed integral breadth as a function of s, Bp is the instrumental broadening by the primary beam, <L> is the average length of the scattering domain, and Bg is the true integral breadth of the orientation distribution. If a

Lorentizan distribution is used to determine Bobs, the equation for average scattering domain length changes to equation 5 [13].

$$s\mathrm{B}_{\mathrm{obs}}(\mathrm{s}) = \mathrm{B}_{\mathrm{p}} + \frac{1}{\langle \mathrm{L} \rangle} + \mathrm{sB}_{\mathrm{g}} \quad [5]$$

The calculations for Ruland's Analysis were carried out in MatLab. The code for this analysis using a Gaussian distribution is listed in Appendix.

Irena/Igor Software – Maximum Entropy

In addition to RSA, other techniques were explored with the intention to (1) confirm the accuracy or inaccuracy of RSA, and (2) give more information about the pore/domain sizes and distributions. The Maximum Entropy (MaxEnt) method developed by Jemian was identified as a suitable technique to describe pore distributions assuming a cylindrical shape with aspect ratio of 5+. The MaxEnt technique attempts to solve equation 6 by limiting various constraints and matching histograms to the data based on scattering contrast and morphology (shape, degree of interaction, aspect ratio, orientation, etc.) [15-16].

$$I(Q) = \sum_{k} |\Delta\rho_k|^2 S_k(Q) \sum_{i_k} |F_k(Q, D_{ik})|^2 V_k(D_{ik}) f_k(D_{ik}) \Delta D_{ik} \quad [6]$$

In equation 6, the subscript *i* denotes all histogram bins in the size distribution, *k* denotes different populations with it's own binning index i_k, D is the particle dimension, S(Q) is the structure factor, F(Q, D) is the scattering form factor, V(D) is the particle volume, f(D) is the volume size distribution, and $|\Delta\rho|^2$ is the scattering contrast [15, 16]. The volume size distribution is calculated from the number size distribution (N(D)) the total number of scatters (N_T) the probability of occurrence of a scatter of size D ($\Psi(D)$), and V(D) by:

$$f(D) = V(D)N(D) = V(D)N_T\Psi(D) \quad [7]$$

MaxEnt is imbedded in the Igor Pro – Irena software package assembled by Jemian and Ilavsky [15]. Varying constrains in equations 6 and 7 allows a near perfect fit to the experimental data. Figure 8 displays an example file of a carbon fiber analysis. The graph shows the computed pore sizes and distribution from the inputs given. The data (green = raw, red = background subtracted) and fit (blue line) are nearly perfect demonstrating a successful model.

Through these two techniques, a full SAXS analysis can be completed on the carbon fiber. Ruland's Streak Analysis gives information on the length of the scatterer or pore while the Irena – Igor analysis gives the diameter of the pore. Accuracy for SAXS data analysis is confirmed through independent completion of each technique and observing parallel results [15-16].

REFERENCES

1. Kant, M. and D. Penumadu, *Dynamic mechanical characterization for nonlinear behavior of single carbon fibers.* Composites Part A: Applied Science and Manufacturing, 2014. **66**: p. 201-208.
2. Kant, M. and D. Penumadu, *Fracture behavior of individual carbon fibers in tension using nano-fabricated notches.* Composites Science and Technology, 2013. **89**: p. 83-88.
3. Drzal, L. and M. Mudhukar, *Fibre-matrix adhesion and its relationship to composite mechanical properties.* Journal of Materials Science, 1993: p. 569-610.
4. Hunston, D., et al., *Test Protocol for Single-Fiber Fragmentation Test - International Round Robin.*
5. Feih, S., et al., *Establishing a Testing Procedure for the Single Fiber Fragmentation Test*. 2004, Risø National Laboratory.
6. Ohsawa, T., et al., *Temperature Dependence of Crtical Fiber Length for Glass Fiber-Reinforced Thermosetting Resins.* Journal of Applied Polymer Science, 1978. **22**: p. 3203-3212.
7. Piggott, M.R., *Why Interface Testing by Single-Fibre Methods can be Misleading.* Composite Science and Technology, 1997. **57**: p. 965-974.
8. Zhandarov, S.F. and E.V. Pisanova, *Two Interfacial Shear Strength Calculations Based on the Single Fiber Composite Test.* Mechanics of Composite Materials, 1995. **31**(4): p. 446-461.
9. Cullity, B.D., *Elements of X-Ray Diffraction*. 1956: Addison-Wesley Publishing Company.

10. Paulauskas, F.L., T.L. White, and J.E. Spruiell, *Structure and Properties of Carbon Fibers Produced using Microwave-Assisted Plasma Technology, Part 2*, in *2006 SAMPE* 2006, Society for the Advancement of Material and Process Engineering.
11. Diefendorf, R.J. and E. Tokarsky, *High Performance Carbon Fibers.* Polymer Engineering and Science, 1975. **15**(3): p. 150-159.
12. Perret, R. and W. Ruland, *Single and Multiple X-Ray Small-Angle Scattering of Carbon Fibres.* Journal of Applied Crystallography, 1969. **2**.
13. Stribeck, N., *Ruland's Streak Method*, in *X-Ray Scattering of Soft Matter*. 2007, Springer Laboratory p. 201-205.
14. Thunemann, A. and W. Ruland, *Microvoids in PAN Fibers - A Small-Angle X-ray Scattering Study.* Macromolecules, 2000. **33**: p. 1848-1852.
15. Ilavsky, J. and P.R. Jemian, *Irena: tool suite for modeling and analysis of small-angle scattering.* Journal of Applied Crystallography, 2009. **42**(2): p. 347-353.
16. Jemian, P.R., et al., *Characterization Of 9Cr-IMoVNb Steel By Anomalous Small-Angle X-Ray Scattering.* Acta Metallurgica et Materialia, 1991. **39**(11): p. 2477-2487.

CHAPTER I: SYNTHESIS AND CHARACTERIZATION OF LIGNIN CARBON FIBERS AND COMPOSITES

A version of this chapter is currently under review for publication.

This paper is first authored by Meek. The work presented herein is completed by Meek. Penumadu, Young, Harper, and Rials served in advisory roles. Hosseinaei and Harper developed the lignin carbon fiber produced for this study.

Authors: Nathan Meek[1], Dayakar Penumadu[1], Omid Hosseinaei[2], David Harper[2], Stephen Young[1], Timothy Rials[2]

[1]Civil and Environmental Engineering, University of Tennessee at Knoxville. 325 John D Tickle Building, Knoxville, TN 37996 USA

[2]Center for Renewable Carbon, University of Tennessee at Knoxville. 2506 Jacob Drive, Knoxville, TN 37996, USA

ABSTRACT

In this study, authors fabricate uniaxial continuous lignin fibers, from switchgrass, via multifilament meltspinning and convert them into carbon fibers using optimized stabilization and carbonization techniques. Subsequent unidirectional, continuous carbon fiber composites were produced through vacuum assisted resin transfer molding (VARTM) using these carbon fibers. Lignin carbon fibers were characterized using Nano-Universal Testing Machine (Nano UTM), Single Fiber Fragmentation (SFFT), and X-Ray Diffraction (XRD). For the first time, lignin carbon fibers were precisely characterized using a Nano UTM. Modulus values of ~36 GPa and failure stress of ~600 MPa for single carbon fibers were obtained and follow the same nonlinear response observed in Poly-acrylonitrile (PAN) carbon fibers during tensile loading. Microscopy revealed few defects within and along the lignin carbon fibers, but the fibers possessed minimal crystalline regions and crystallite alignment relative to commercial PAN based fibers. SFFT of single fiber

composites indicate interfacial shear strength to be approximately 16.7 MPa (average fiber length of 228) with an average size of 100 μm delamination zone. Unidirectional composite coupons achieved tensile modulus of 9 GPa and strength of 85 MPa with 1 percent failure strain. Low composite strength is the likely result of fiber layup, fiber fusing, non-continuous fibers across the composite, and composite voids. Nano-UTM and SFFT results presented here have important implications for lignin carbon fiber use in a wide range of applications that optimize fiber/resin bonding. In addition, composite manufacturing procedures detailed here are a major step forward in lignin carbon fiber composite production.

Keywords: Lignin, Carbon Fibers, Biocomposites, Interface/interphase, Mechanical properties, Vacuum Infusion

1. INTRODUCTION

Carbon fiber composites due to their high strength to weight ratio are of interest to a wide range of industries including wind energy, aerospace, and automotive. Carbon-fiber reinforced polymers (CFRP) are of particular interest to the automotive industry because of recent US legislation requiring increased fuel economies of 35.5 mpg for 2017 and 54.5 mpg for 2025 [1]. It is estimated that CFRP's could reduce the weight of a car by 60 percent, which will dramatically increase fuel economy. Automotive companies are reluctant to switch to CFRP due to the high initial cost of materials [2]. This has led to a large effort to explore options for inexpensive carbon fiber manufacture.

A large portion of the overall cost of carbon fiber based composites comes from the development and processing of the precursor. Most carbon fiber used for commercial and industrial applications comes from petroleum-based precursors such as polyacrylonitrile (PAN) and mesophase pitch (MPP). These precursors are relatively expensive, contributing to more than 50

percent of the manufacturing costs of a carbon fiber. Several other polymers, such as lignin and silk, have been targeted as possible replacements for carbon fiber precursors [3]. There is a growing interest in lignin, due to its potential abundance, high carbon content, renewable nature, and potential low cost as a by-product of the paper industry and biofuel extraction processes. Lignin, a complex, three-dimensional network polymer, is comprised of aromatic alcohols with differing degrees of methoxy substitution based on parent plant material.

In this paper, authors use a modified organosolv fractionation process to produce lignin from an emerging bioenergy crop, switchgrass, which possesses high purity and desirable flow/rheological/extrusion characteristics for fiber processing [5-7]. Results associated with the synthesis of organosolv fractionated lignin-based polymer precursor fibers, suitable steps to stabilize and carbonize them to produce semi-continuous carbon fibers, and characterization techniques to develop mechanical, interfacial, and structural parameters are reported. Important structure-property relationships associated with the mechanical behavior of the single fibers subjected to tensile loading are determined using a highly precise nano-tensile testing system. Carbonized fibers are characterized using X-ray diffraction (XRD) for crystallinity, and scanning electron microscopy (SEM) for morphology. Using 100 percent lignin based carbon fibers, quasi-isotropic Vacuum Assisted Resin Transfer Molding (VARTM) bio-epoxy based composites were also produced and mechanical properties were evaluated utilizing dimensional digital image correlation (DIC) to identify failure modes corresponding to these lignin composite panels produced for the first time by the authors.

2. MATERIALS AND METHODS

2.1 Lignin Biomass and Fiber Production

The lignin used for the production of carbon fiber consisted of Alamo switchgrass (*Panicum virgatum*) feedstock supplied by TennEra, LLC. The lignin was isolated using a proprietary organosolv process resulting with high purity (98.1 percent) and low ash (0.12 percent) [4]. The lignin biomass was characterized using a Fisher-Johns melting point apparatus and Perkin Elmer Pyris 1 TGA [5-8]. The as-received switchgrass feedstock had a zero shear melt flow temperature (T_m) of ~170^{o}C observed and a glass transition temperature (T_g) of 109^{o}C. TGA results demonstrated that the lignin biomass contained an average of 6 percent moisture and began degrading in the 230-260 ^{o}C range.

Switchgrass lignin was melt-spun into fiber form using a pilot scale single-screw, pressure-controlled extruder (Alex James and Associates, Inc.), with temperature varied along the extruder barrel starting at 150 to 180°C at the die and optimized for a residence time on the order of several minutes. Initially, lignin was pelletized using a 19 mm diameter extruder attached to a metering pump with a 15 mm orifice. Pellets were dried in a vacuum oven at 80°C and 560 mmHg for 12 hrs. and subsequently melt-spun into fibers using a spinneret with twelve 150 μm diameter holes. Extruded green fibers were collected onto a winder at a take-up speed 300m/min. The lignin fibers were mounted on steel meshes and placed in a programmable convection oven and oxidatively stabilized using a rate of 0.02°C/min up to 250°C. Stabilized fibers were transferred to a carbonization furnace where they were carbonized in a nitrogen environment at 3°C/min to 1000°C and held for 15 minutes. Produced carbon fiber possessed a near circular cross-section and were relatively defect-free based on observations using scanning electron at

various locations along the length of the fiber (Fig. 9). The average fiber diameter was 16.3 μm with a standard deviation of 5.7 μm.

2.2 Material Selection for Carbon Fiber Reinforced Composite Panel Manufacturing

Super Sap Epoxy resin (Entropy Resins) consisting of epoxidized pine oils, was used as the matrix resin for carbon fiber composite panels due to its large biomass content (37 percent biobased carbon content from pine-based feedstocks) relative to other commercially available epoxies with the future goal of producing high biomass and sustainable composites [9].

Carbon fiber composites, approximately 13 cm x 13 cm square, were produced in this study using a modified Vacuum Assisted Resin Transfer Molding (VARTM) process (Fig. 10). Composite samples were then trimmed and cut to lengths for evaluating mechanical properties [10].

2.3 Single Carbon Fiber Mechanical Characterization

The mechanical properties of the single carbon fibers were determined using a MTS Bionix Nano-Universal Testing Machine (Nano UTM) equipped with custom grips specifically designed to test single fibers. The Nano UTM is a unique apparatus due to its high accuracy and resolution as well as its ability to measure static and dynamic properties. Accuracy is maintained by a rigorous set of internal electronic and mechanical calibrations before testing. The resolution for measuring load and displacement with this unique testing system are on the order of an nN and nm, respectively. Nano UTM (Fig. 11) offers the ability to obtain monotonic stress-strain data while continuously measuring the complex modulus as a function of applied tensile strain with a nano-mechanical actuating transducer (NMAT) [11].

After evaluating tensile properties for a representative batch of single fibers (typically 20 to 25), a two-parameter Weibull distribution is employed to obtain the shape and scale parameters

associated with the tensile behavior of these carbon fibers and used in the derivation of the interfacial shear strength [17].

2.4 Composite Mechanical Characterization

The produced composite was mechanically tested using a servo-hydraulic testing system (MTS-810) equipped with a 5 kip load cell at a rate of 0.5mm/min. Tensile test samples are prepared and tested according to relevant composite ASTM standards [10]. During the deformation of the composite sample, digital image correlation (DIC) system was used for obtaining local spatial variation of axial strains associated with potential heterogeneities in composite layup and processing. The DIC system has 50 micro-strain resolution at 1 Hz using dual 29 mega-pixel cameras from Correlated Solutions.

2.5 Fiber/Resin Interface Characterization

Interfacial properties were determined using single fiber fragmentation testing (SFFT) or single filament composite (SFC) where a single carbon fiber is embedded in a dogbone sample of resin [17]. SFFT was completed using a micro-load custom frame to apply tension to the SFC while observing fiber fractures in the composite *in-situ* under polarized microscopy. The procedure utilized in this study was developed based on prior art associated with the related standards and practices for SFFT [12, 13].

Using a custom developed load frame for SFFT, fiber fractures and their evolution under high magnification and polarized light were observed until saturation was reached in a systematic and consistent fashion. The broken fiber lengths and delamination zones are measured at saturation *in-situ*. From the fiber lengths, the interfacial shear strength (IFSS) is determined using Eq. 8:

$$\tau_{IFSS} = \frac{\sigma_f * d}{2 * l_c} \quad [8]$$

where τ_{IFSS} is the interfacial shear strength, σ_f is the tensile strength at given gauge length, d is the fiber diameters, and l_c is the critical fiber length.

2.6 Wide-Angle X-Ray Diffraction

Wide-Angle X-Ray diffraction (WAXS) was completed on a Philips X'Pert XRD Diffractometer to evaluate the structure of the carbon fiber. Several parameters of interest to the lignin based carbon fibers include the peak positions corresponding to basal atomic planar spacing, the stacking height of the turbostratic graphitic planes (Lc), the crystallite size (La), and orientation of the planes with respect to the axis of the fiber, which are all important for structure-property relationships in PAN based carbon fibers [14-17]. The basal plane d-spacings of interest are the (002) and (100) as these indicate the crystallite parameters. Although normally the Lc and La are determined as well, the lignin carbon fiber showed little crystallinity; thus, these parameters are not considered.

3. RESULTS AND DISCUSSION

This section refers to Figures 9 through 19 and Tables I through III.

3.1 Single Fiber Mechanical Results

The single carbon fibers possessed an average failure stress of ~590 MPa and a tensile modulus of ~35 GPa (Table 1, Fig. 12). Compared to previous lignin based carbon fiber studies, the organosolv lignin fibers based on switchgrass biomass have favorable mechanical performance [2] .

The Weibull parameters from 27 single carbon fibers are 3.66 (m) and ~630 MPa (σ_0) for shape and scale parameters respectively (Fig 12) which are developed to calculate the interfacial shear strength [18-21]. These parameters show a high scale parameter but lower shape parameter relative to other lignin Weibull parameters indicating higher strength lignin carbon fibers but a wider range of properties, probably due to variation in lignin molecule size from the feedstock after the

fractionation process [22]. Relative to other current and past studies associated with attempts to develop carbon fibers from lignin precursors, these mechanical properties are relatively high [23, 24]. In the authors' opinion, additional thermal treatments to improve the lignin-carbon structure and tensioning of the fibers during stabilization and carbonization phase will likely reduce defect density with further improvements in mechanical properties and possibly also increase the crystalline regions thereby, increasing the effect of tensioning/alignment and mechanical properties [25].

As consistent with other reported literature, there is a correlation between fiber diameter and mechanical properties. As the fibers decrease in diameter the modulus increases due to a more effective stabilization process where oxidation of the fiber is easier with a smaller diameter [26]. From Figure 13, it appears that a 5 μm fiber would have an approximate modulus of 36 GPa. This trend can be deceiving, as the experimental data does not fit to the linear trend-line well. The relationship of fiber diameter to modulus is not as well defined for lignin based carbon fibers relative to PAN based carbon fibers due to more variability in the lignin precursor fiber production process. Commercially available PAN carbon fibers are produced in highly controlled wet-spinning environments and there is a wealth of industrial experience for manufacturing PAN based fibers, therefore mechanical properties show less variation [11].

Interestingly, the lignin carbon fibers show a nonlinear increase in modulus with tensile strain which is similar with PAN based carbon fiber samples [11]. PAN carbon fiber shows a distinct relationship between the initial tensile modulus value and its increase with applied axial strain as described in Eq. 9. Lignin carbon fiber exhibits similar non-linear stiffening behavior but to a lesser extent than was found for PAN based carbon fibers (Fig. 14).

$$E(\varepsilon) = (\gamma E_0) * \varepsilon + E_0 \quad [9]$$

In this equation, γE_0 is the change in modulus versus strain and E_0 is the initial storage modulus. PAN carbon fibers typically follow the equation [11]:

$$\gamma E_0 = 29.36 * E_0 - 1010 \quad [10]$$

This study has demonstrated that lignin carbon fibers adhere to this equation as well indicating that this equation may describe a universal feature of all carbon fiber (Fig. 14).

3.2 Amorphous Microstructure

The wide-angle X-ray diffraction results for carbonized lignin fibers are shown in Fig. 15. Charts for evaluating the location of peaks near 26° and 43° 2θ, which are typically observed for PAN based carbon fibers, and the azimuthal scan about the (002) peak are shown. Little crystallinity can be observed for lignin-based carbon fibers based on these diffraction patterns. A fundamentally different microstructure develops in lignin-based carbon fibers compared to commercial PAN based fibers (Fig. 15). The diffraction analysis presented here is limited because the peaks are low in intensity, full-width half-max (FWHM) is undeterminable, and results yield little crystalline structure information.

The highly amorphous microstructure is likely a result of the complex nature of the lignin molecule. Several factors limit the growth of crystalline regions within the lignin molecule during stabilization and oxidation including entanglements, heterogeneous molecular backbone, small phenolic groups not a part of the primary polymer chain, and contaminants. In comparison, PAN involves simple chemical modifications to obtain a turbostratic graphitic structure (dehydrogenation, cyclization, and carbonization) whereas the lignin molecule involves a multitude of different reactions and bonds to resemble a structure that is remotely similar to graphite [27, 28] (Fig. 16).

3.3 Interfacial Results

The ability of the fiber to transfer stress to the polymer matrix is governed by interfacial shear strength (IFSS) and is one of the most important parameters governing the strength of fiber reinforced composites. Commercial PAN based carbon fibers undergo extensive surface treatment, including additional sizing, to provide a good interface with a target resin system. In this study, the interfacial shear strength of unmodified lignin based carbon fibers with an epoxy resin system are reported for the first time (Table II, Fig. 17). The SFFT results for the lignin carbon fiber indicate an interfacial shear stress of 16.7 MPa. Delamination zones tend to be smaller (~100 μm) due to the larger number of fractures along the fiber. This finding could be due to natural surface functionalization from lignin precursors.

The shape and size of the delamination zones suggest interfacial damage along the fiber during SFFT. The birefringent areas along the fiber, which indicate interfacial damage, tend to progress down the fiber as strain increases. Although the interface becomes damaged with increased strain, most fiber fractures tend to propagate into the resin signifying a strong interface. Thus, at larger strains the fiber interface will become damaged instead of fully transferring stress into the matrix resin [29] (Fig. 17).

Another finding is that while interfacial damage occurs, the fiber does not pull out of the matrix, indicating the presence of significant interfacial shear strength with the epoxy resin system. Other fiber/resin systems that are commercially available with tailored sizing tend to show interfacial shear strengths in the range of 20-43 MPa [30, 31]. Images from delamination zones (Fig. 17) illustrate significant bonding by propagating fractures into the matrix where the fibers fractures and large stressed regions signifying relatively effective stress transfer from untreated lignin carbon fiber to resin. Due to a lower carbonization temperature (1000°C) employed in this study for

producing lignin carbon fiber, it is likely that functional groups, such as hydroxyl, methoxyl groups, remain on the surface leading to a higher IFSS observed [32, 33].

Additional improvements to the manufacturing process of these lignin based carbon fibers such as optimal stabilization and carbonization, possible integration of suitable sizing agents, improved fiber properties should further enhance IFSS and resulting reinforced composite properties. A significant factor that affects the calculation of the interface shear strength is the tensile strength of the carbon fiber and increasing lignin carbon fibers strength properties will increase it's interface shear strength and the overall composite mechanical properties, an important finding for optimizing future lignin carbon fiber reinforced composite systems. Due to its relatively high interfacial shear strength for unsized carbon fiber, the lignin carbon fiber produced in this study would be ideal for various applications that take advantage of carbon fiber interfacial properties such as chopped fiber composites.

3.4 Mechanical Behavior of Lignin Based Carbon Fiber Composites

A reinforced composite laminate using the lignin carbon fibers was manufactured using VARTM resulted in a 14 cm by 14 cm panel as shown in Fig. 18 (a). The composite was then trimmed to 13 cm by 13 cm using a diamond blade saw. The trimmed composite possessed consistent density and uniform thickness (0.2 ± 0.02 cm) across the sample (Fig. 18 (b)).

High-resolution strain mapping through three-dimensional digital image correlation (DIC) was used to identify local tensile strain deformation on the surface of the fabricated composite. Samples were cut to 100 cm by 12.5 cm [10] and GS10 glass fiber tabs were attached (Fig. 19).The samples are speckled with a random pattern as DIC maps strain by tracking relative displacements in the applied random speckle pattern on the sample during deformation. Table III shows the results collected from DIC and tensile testing of along fiber axis samples of the square laminates.

Composite samples demonstrated an average failure strength of 85 MPa and average modulus of 9 GPa. The failure mode for the composite samples was either lateral or angled brittle failure in the gauge region as seen in Fig. 19 [10]. This type of failure indicates a high interfacial shear strength relative to fiber strength whereas a composite with an extremely high fiber strength relative to its interfacial shear strength tends to show explosive failure modes with failure largely along the fibers [34]. Having composites with non-explosive failures are preferable so that composite materials do not catastrophically fail.

The Voigt model (or rule of mixtures) is used to estimate the composite modulus based on volume fraction of fibers and carbon fiber properties along fiber axis. For the composite shown in Fig. 18, the composite modulus, E_{11}, is estimated to be 16.1 GPa using Eq. 11,

$$E_M V_M + E_F V_F = E_c \quad [11]$$

where V_f is fiber volume, E_f is fiber modulus, V_m is matrix volume, E_m is matrix modulus, and E_c is composite modulus. Experiments indicate a value of 9 GPa as per Table II and the lower observed value is expected due to a lack of highly aligned and continuous carbon fibers in the laminate. Manufactured composites were produced in non-optimal conditions due to misalignment of the fibers in the preform during VARTM. The produced lignin carbon fiber was cut from a spool and thus, it was difficult to achieve complete fiber alignment and uniform density across the composites. In addition, most fibers were non-continuous and voids were introduced during the VARTM process, although efforts were made to minimize defects. These factors affected the panel quality, led to out of plane deformation during tensile testing, and premature failure. Currently, panel production and quality is under continued development to address these needed areas of improvement.

Continued development in the mechanical properties of the lignin carbon fiber would also dramatically improve the overall composite performance as composite properties are a culmination of mechanical, interfacial, and structural properties [35, 36]. Current investigations are under way to improve the graphitic structure of lignin fibers, reduce fiber defects, optimize biomass precursors, modifying the extrusion equipment to handle lignin volatiles, and increase temperatures and/or modify temperature cycles during stabilization/carbonization. Currently, lignin based carbon fiber composites are suitable for non-structural and semi-structural applications, but increasing modulus and failure stress of the fibers further will enable structural composites by taking advantage of lignin carbon fiber's superior matrix interaction.

4. CONCLUSION

Organosolv fractionated lignin carbon fiber was produced and characterized via Nano-UTM, Single Fiber Fragmentation, and X-Ray Diffraction. In addition, a unidirectional carbon fiber reinforced polymer composite was manufactured with the lignin carbon fiber through a modified VARTM process. Lignin carbon fiber exhibited little to no surface defects from SEM and optical microscopy. Mechanical results for the carbon fiber indicated an average modulus close to 36 GPa and failure stress of ~600 MPa (3.66 and 630 MPa shape and scale parameters). Interfacial shear strength values were relatively high around ~15 MPa and delamination zones of 100 μm for unsized lignin carbon fiber. SFFT saturated samples revealed fiber fractures propagating into the matrix and no fiber pullout. These interface strength results indicate that lignin carbon fiber would be ideal for applications that take advantage of interfacial strengths such as chopped fiber composites or fillers. XRD results and analysis demonstrated little to no crystalline regions in the fibers, which is likely the reason for low modulus of the fibers compared to commercially available PAN based fibers. Nevertheless, lignin based carbon fibers tend to follow the same strain hardening trend found in

other carbon fibers, which may indicate a general rearrangement of amorphous carbon when strain is applied. After the lignin carbon fiber was fully characterized, unidirectional mats were placed in a preform inside a VARTM system and produced into a composite. Fiber alignment and quantity varied across the panel during production. The composite panel mechanical properties were ~9 GPa and ~85 MPa for modulus and failure strength, respectively. Composite samples demonstrated lateral brittle failures in the gauge region indicating a large ratio of interface to mechanical strength. Produced lignin carbon fiber composites exhibited non-explosive failure mechanisms with minimal fiber pullout as seen in SFFT.

Overall, the lignin carbon fiber demonstrated relatively high mechanical and interfacial properties for carbon fiber with no sizing. This advantage over commercial fibers that require additional sizing suggests that lignin carbon fiber would be preferable in some applications that mobilize the interface such as chopped fiber composites, consumables for additive manufacturing, and fillers. Results presented in this study are a significant improvement to current lignin carbon fiber characterization techniques and lignin carbon fiber composite manufacturing. Continued development and improvement of the mechanical performance will open more utilization of lignin carbon fiber, particularly in automotive applications.

ACKNOWLEDGEMENTS

We'd like to acknowledge TennEra, L.L.C. (www.tennera.com) for supporting this research project, Dr. Joseph Spruiell for his aid in XRD analysis, Dr. Joseph Bozell and Alexandra Peeden for their help with molecular weight determination, and Valeria Garcia-Negron for assisting with thermal characterization of the lignin. In addition, we'd also like to thank Dr. Ahmad Vakili for his contributions in thermal processing lignin fibers.

REFERENCES

1. *2017 and Later Model Year Light-Duty Vehicle Greenhouse Gas Emissions and Corporate Average Fuel Economy Standards*, in *Federal Register*. 2012, US Environmental Protection Agency. p. 62624-63200.
2. Baker, D.A. and T.G. Rials, *Recent advances in low-cost carbon fiber manufacture from lignin.* Journal of Applied Polymer Science, 2013. **130**(2): p. 713-728.
3. Khan, M.M.R., et al., *Carbon fiber from natural biopolymer Bombyx mori silk fibroin with iodine treatment.* Carbon, 2007. **45**(5): p. 1035-1042.
4. Sluiter, A., et al., *Determination of Structural Carbohydrates and Lignin in Biomass.* National Renewable Energy Laboratory, 2008.
5. Baker, D.A., N.C. Gallego, and F.S. Baker, *On the characterization and spinning of an organic-purified lignin toward the manufacture of low-cost carbon fiber*. Journal of Applied Polymer Science, 2012. **124**(1): p. 227-234.
6. Gunaratne, L. and R.A. Shanks, *Melting and thermal history of poly(hydroxybutyrate-co-hydroxyvalerate) using step-scan DSC.* Thermochimica Acta, 2005. **430**(1-2): p. 183-190.
7. Sammons, R.J., et al., *Characterization of Organosolv Lignins using Thermal and FT-IR Spectroscopic Analysis.* BioResources, 2013. **8**(2): p. 2752-2767.
8. Liu, P., et al., *Glass transition temperature of starch studied by a high-speed DSC.* Carbohydrate Polymers, 2009. **77**(2): p. 250-253.
9. *Super Sap 100/1000 Technical Data Sheet*. 2010; Available from: https://entropyresins.com/wp-content/uploads/2014/03/TDS_100_1000_v4-TDS-100-1000-System.pdf.

10. International, A., *ASTM D3039: Standard Test Method for Tensile Properties of Polymer Matrix Composite Materials*. 2014.

11. Kant, M. and D. Penumadu, *Dynamic mechanical characterization for nonlinear behavior of single carbon fibers.* Composites Part A: Applied Science and Manufacturing, 2014. **66**: p. 201-208.

12. Hunston, D., et al., *Test Protocol for Single-Fiber Fragmentation Test - International Round Robin.*

13. Feih, S., et al., *Establishing a Testing Procedure for the Single Fiber Fragmentation Test.* 2004.

14. Warren, B.E. and P. Bodenstein, *The Shape of Two-dimensional Carbon Black Reflections.* Acta Cryst, 1966. **20**(602).

15. Donnet, J.-B. and R.C. Bansal, *Carbon Fibers.* 1990.

16. Klug, H. and L. Alexander, *X-Ray Diffraction Procedures For Polycrystalline and Amorphous Materials.* 1974.

17. Warren, B.E., *X-ray diffraction.* 1969, Reading, Mass.: Addison-Wesley Pub. Co.

18. Van der Zwaag, S., *The Concept of Filament Strength and Weibull Modulus.* Journal of Testing and Evaluation, 1989. **17**(5): p. 292-298.

19. Wilson, D., *Statistical tensile strength of NextelTM 610 and NextelTM 720 fibres.* Journal of Materials Science, 1997. **32**(10): p. 2535-2542.

20. Beetz, C., *A Self Consistent Weibull Analysis of Carbon Fiber Strength Distributions.* Fibre Science and Technology, 1982. **16**: p. 81-94.

21. Naito, K., et al., *Tensile and Flexural Properties of Single Carbon Fibers,* in *ICCM-18.* 2011: Jeju Island, S. Korea.

22. Nordström, Y., R. Joffe, and E. Sjöholm, *Mechanical characterization and application of Weibull statistics to the strength of softwood lignin-based carbon fibers.* Journal of Applied Polymer Science, 2013. **130**(5): p. 3689-3697.

23. Kadla, J.F., et al., *Lignin-based carbon fibers for composite fiber applications.* Carbon, 2002. **40**: p. 2913-2920.

24. Lin, J., et al., *Improvement of Mechanical Properties of Softwood Lignin-Based Carbon Fibers.* Journal of Wood Chemistry and Technology, 2013. **34**(2): p. 111-121.

25. Liu, Y., H.G. Chae, and S. Kumar, *Gel-spun carbon nanotubes/polyacrylonitrile composite fibers. Part III: Effect of stabilization conditions on carbon fiber properties.* Carbon, 2011. **49**(13): p. 4487-4496.

26. Huang, X., *Fabrication and Properties of Carbon Fibers.* Materials, 2009. **2**(4): p. 2369-2403.

27. Beste, A., *ReaxFF study of the oxidation of lignin model compounds for the most common linkages in softwood in view of carbon fiber production.* J Phys Chem A, 2014. **118**(5): p. 803-14.

28. Chung, H. and N.R. Washburn, *Chemistry of lignin-based materials.* Green Materials, 2013. **1**(3): p. 137-160.

29. Kim, B.W. and J.A. Nairn, *Observations of Fiber Fracture and Interfacial Debonding Phenomena Using the Fragmentation Test in Single Fiber Composites.* Journal of Composite Materials, 2002. **36**(15): p. 1825-1858.

30. Zhao, J., et al., *A comparative study of fibre/matrix interface in glass fibre reinforced polyvinylidene fluoride composites.* Colloids and Surfaces A: Physicochemical and Engineering Aspects, 2012. **413**: p. 58-64.

31. Park, J.M., *Interfacial Properties of Two-Carbon Fiber Reinforced Polycarbonate Composites Using Two-Synthesized Graft Copolymers as Coupling Agents.* J Colloid Interface Sci, 2000. **225**(2): p. 384-393.

32. Sudo, K. and K. Shimizu, *A New Carbon Fiber from Lignin.* Journal of Applied Polymer Science, 1992. **44**: p. 127-134.

33. Brodin, I., et al., *Oxidative stabilisation of kraft lignin for carbon fibre production.* Holzforschung, 2012. **66**(2).

34. Okoli, O.I. and G.F. Smith, *Failure modes of fibre reinforced composites: The effects of strain rate and fibre content.* Journal of Materials Science, 1998. **33**: p. 5415-5422.

35. Yan, X., et al., *Relationship study between crystal structure and thermal/mechanical properties of polyamide 6 reinforced and unreinforced by carbon fiber from macro and local view.* Polymer, 2014. **55**(23): p. 6186-6194.

36. Lu, N., R.H. Swan, and I. Ferguson, *Composition, structure, and mechanical properties of hemp fiber reinforced composite with recycled high-density polyethylene matrix.* Journal of Composite Materials, 2011. **46**(16): p. 1915-1924.

CHAPTER II: INTERFACE STRENGTH AND SURFACE CHEMISTRY OF ORGANOSOLV LIGNIN CARBON FIBER FOR BIOCOMPOSITE APPLICATIONS

A version of this chapter is currently under review for publication.

This paper is first authored by Meek. The mechanical and interfacial testing as well as data analysis for mechanical, interfacial, and X-ray photoelectron spectroscopy was completed by Meek. Penumadu, Harper, Hosseinaei, and Foston served in advisory roles. Foston completed X-ray photoelectron spectroscopy testing.

Nathan Meek[1], Omid Hosseinaei[2], David Harper[2], Marcus Foston[3], Dayakar Penumadu[1], Timothy Rials[2]

[1]Civil and Environmental Engineering, University of Tennessee at Knoxville. 325 John D Tickle Building, Knoxville, TN 37996 USA

[2]Center for Renewable Carbon, University of Tennessee at Knoxville. 2506 Jacob Drive, Knoxville, TN 37996, USA

[3]Department of Energy, Environmental & Chemical Engineering, Washington University, 1 Brookings Drive, Saint Louis, MO 63130, USA

Corresponding Author:

Present/permanent address:

Keywords: Organosolv, Lignin Carbon Fiber, Single Fiber Fragmentation, X-Ray Photoelectron Spectroscopy, Nano-mechanical testing

ABSTRACT

The interfacial shear strength and surface chemistry of organosolv lignin carbon fiber (LCF) with an industrial epoxy are evaluated. Eight LCF samples were selected for the study with varying biomass feedstocks, processing parameters, and post-extrusion treatments. The LCF sets were studied with T700S selected as the commercial standard. To determine interfacial shear strengths, single fiber fragmentation testing (SFFT) is utilized. SFFT was completed using a custom-built testing frame for loading of single fiber composites under transmission microscopy. For mechanical properties, single carbon fibers were tested using MTS Bionix Nano-Universal Testing Machine (UTM) with unique grips and capabilities designed for testing single carbon fibers. LCF samples exhibited average failure stresses ranging from ~280 to 610 MPa and average modulus values varied from ~28 to 40 GPa. Determined interface values from SFFT were in the range of 7 to 23 MPa. With no sizing agents or surface treatments, samples with higher interface values (16+ MPa) show considerable interface strengths relative to the industrial standard. Fiber fractures tend to propagate into the resin indicating significant fiber-resin adhesion. To further characterize fiber/resin interfaces, LCF samples were analyzed using X-ray Photoelectron Spectroscopy (XPS). XPS results displayed similar results from sample to sample, however, a small C1 peak shift to higher binding energies was observed for LCF samples with better fiber-resin adhesion. A shift to higher binding energies would indicate the presence of more oxidized carbon groups (C-O, C=O, COOH) and therefore, a stronger interfacial chemistry.

1. INTRODUCTION

Carbon fiber materials have seen a historic rise in production and use within the last few decades and currently dominate several industries such as fishing rods, golf clubs, high-end automobile bodies, and aerospace. Widespread use of carbon fiber is limited due to high cost of precursor materials, processing, and composite manufacture. In addition, these materials are derived from petroleum based polymers and therefore, price-dependent on various external factors such as politics, other industries utilizing petroleum, etc. Petroleum is not renewable or sustainable and therefore, price will continue to rise over time. Consequently, there is a large need for carbon fiber produced from renewable and cheap precursors [1].

Lignin, a biopolymer fractionated from biomass, has received significant attention as a replacement to typical carbon fiber precursors such as polyacrylonitrile (PAN) due to it's high carbon content, price, and availability [1, 2]. Lignin is rather abundant due to the large availability of biomass sources. All biomass consists of cellulose, hemi-cellulose, and lignin with 20-30 percent of the total mass being lignin. Lignin is found in the plant cell walls as a reinforcing material. Currently there are numerous groups working on and developing lignin carbon fiber (LCF), however, little work has been completed on LCF interface and surface characterization, which would lead to improvements in composite performance and technology.

The aim of this study is to characterize the mechanical performance and interfacial adhesion/strength of a range of lignin carbon fibers for biocomposite applications. The current samples are unsized (except for the PAN carbon fiber control) and therefore, the interface chemistry can be improved and/or tailored by applying a sizing agent for a specific application. By optimizing the adhesion between the fiber and resin matrix in a carbon fiber composite, the overall composite mechanical performance increases due to successful transfer of stress from the

resin to the fiber. As seen in various composite models (Voigt, Reuss, Tsai, etc.), any off fiber axis loading (tensile or compression) is highly dependent on the interfacial adhesion [3]. Thus, the results presented here will aid in understanding LCF interfaces to optimize fiber-resin adhesion leading to increases in composite performance.

2. MATERIALS

2.1 Organosolv Fractionated Lignin Carbon Fiber

Eight different lignin carbon fibers were selected for this study to observe the effect of different feedstocks, processing parameters, and blends. Table IV shows a table summary of the lignin carbon fiber used in this study. Toray T700S was selected as an industrial comparison to the lignin carbon fiber.

The production process for the lignin carbon fiber begins with fractionation of the source biomass. The lignin is separated from the biomass and contaminants following an organosolv process [4, 5]. The resulting lignin is further purified and dried in preparation for the extrusion process. Lignin fiber is produced using a multi-filament dry spinning technique on a custom-built Alex-James and Associates (AJA) extruder. The AJA extruder is a single screw extruder with four heating zones. The spin head houses a Zenith metering pump and 12-hole (150 μm) spinneret assembly [6].To optimize the process, the lignin powder is initially extruder and evaluated on a lab-scale Haake Minilab extruder. The Haake MiniLab is a counter-rotating twin-screw extruder modified to have a 200 μm spinneret assembly with a heating band. The temperature zones on the AJA extruder are then adjusted based on the lab-scale extrusion and thermal data from Perkin Elmer Diamond Differential Scanning Calorimeter (DSC) and Perkin Elmer Pyris ThermoGravimetric Analysis (TGA). The DSC/TGA values for the samples used in this study are found in Table V.

2.2 High Biomass Epoxy Resin

The epoxy selected for use with the lignin carbon fiber is an Entropy Super Sap 100/1000 commercially available epoxy. This epoxy was selected due to its high biomass content in addition to it's mechanical and optical properties. Super Sap 100/1000 utilizes epoxied pine oils with biobased carbon content comprising approximately 40 percent of the total resin. While it has a considerable amount of biomass content, it is also transparent allowing for in-situ observable of interface testing. Similar to the lignin carbon fiber, this resin is derived from renewable, sustainable resources.

3. EXPERIMENTAL METHODS

3.1 MTS Nano-UTM Mechanical Testing

In evaluating the mechanical properties of single fibers, a MTS Nano Bionix Universal Testing Machine (UTM) was used. The UTM uses a Nano-Mechanical Actuating Transducer (NMAT) to achieve high resolution for load and displacement (nN and nm). The NMAT is comprised of supporting springs, a capacitance gauge, and an electromagnetic coil. The NMAT keeps a zero displacement and measures load on sample through the voltage feedback controlled by a PID loop. An in-depth discussion on the UTM and theory is found elsewhere [7].

The grip and fiber mounting procedure follows Kant, Penumadu [7]. This technique was developed to minimize bending moments about the fiber at the grip. It makes use of rigid aluminum templates instead of industry adopted plastic or cardboard templates. In addition, cut nylon strips glued to the templates to support the sample until it is mounted on the UTM for testing. Machined blocks are used to keep the rigid aluminum templates at a fixed gauge length during sample preparation (Figure 20).

Once the mechanical properties are determined, a two-parameter Weibull distribution is applied to the data to determine shape and size parameters as it provided the best fit. These parameters allow for easy comparison from sample to sample and the size parameter are used in the calculation of the interfacial shear strength [8-11]. The development of the Weibull parameters and equations are discussed further elsewhere [12, 13].

3.2 Single Fiber Fragmentation Testing

For determining interfacial strengths, the Single Fiber Fragmentation Test (SFFT) was used [9]. SFFT entails slowly applying tensile load to a dogbone shaped composite with a single imbedded carbon fiber or single filament composite (SFC). To produce SFC's, an open dogbone mold is used. Carbon fibers are mounted in slits half the height of the mold and resin is poured in the mold. Once the SFC is cured at room temperature, the dogbone samples are removed and placed in a custom frame for SFFT. As load is applied to the sample, the fiber begins to break thereby creating fiber fragments. The fiber in the SFC continues to fracture until the sample is saturated at which more stress or strain on the sample does not lead to more fractures in the fiber. At this saturation point several aspects about the SFC can be observed: (1) delamination zones, (2) fiber fragment lengths, and (3) failure characteristics of the fiber fractures. Delamination zones are areas around fiber fractures that indicate a damaged interface (no bonding between the fiber and resin). All of these features are observed under polarized microscopy as they are birefringent and give a complete interface profile [14].

A custom frame was designed and built specifically to handle SFFT samples (Figure 21). Briefly, the frame used a NEMA motor to turn an ACME screw that pulls/pushes the crosshead. Strain is measured using an external LVDT and load is measured using a Futek 250lb capacity load cell. The frame is controlled using a LabView cRIO system. It is designed for semi-

automatic and manual control. Typically, it operates in manual mode for SFFT allowing users to pause testing at various displacements to record the number of fiber fractures.

3.2 X-Ray Photoelectron Spectroscopy

X-ray Photoelectron Spectroscopy (XPS) was carried out on a PHI 5000 VersaProbe II equipped with a monochromatic AlKα (1486.6 eV) X-ray source. Data from XPS was analyzed using the PHI MultiPak software, after performing a Shirley background correction. Calibration was carried out by aligning of the spectra with reference to the C1s line at 284 eV.

4. RESULTS

4.1 Single Fiber Mechanical Properties

Table VI shows the summarized mechanical data for the single fiber testing. Lignin carbon fiber samples varied from ~250-610 MPa failure stress with a modulus variation of ~28-40 GPa.

To show the spread of data for the lignin carbon fiber, Figure 22 shows all tests for stress versus strain. Standard deviation of mechanical properties were the largest for C5 and C1. In addition, shape and size parameters are determined from the linear trend lines of the Weibull distributions presented in Figure 23.

4.2 Single Fiber Fragmentation – Interface Adhesion

Figure 24 displays several SFFT samples. The average fiber fragmentation length is measured in-situ during SFFT and is listed in Table 4. This length is defined as the length from one fiber break to the next fiber break (Fig. 24). The T700S samples demonstrated considerably larger fragmentation lengths and thus, it was difficult to capture an entire fragment at 20x magnification.

The experimental SFFT data and calculated interfacial shear strength (IFSS) values are summarized in Table VII. It seems that there are two groups of samples for interface values. There appears to be one set of LCF samples with lower IFSS values (7-10 MPa) and one with higher IFSS values (15+ MPa).

4.3 X-Ray Photoelectron Spectroscopy

Results for XPS are shown in Figure 25. Results demonstrate a trend between C-C bonds and IFSS. It appears that increasing oxidized carbon is creating a weaker interface.

5. DISCUSSION

This section refers to Figures 20 through 30 and tables IV through VII.

5.1 LCF Mechanical Properties

The lignin carbon fiber displayed decent mechanical properties with several sets performing near 600 MPa failure strength and 39 GPa modulus. C1 in particular demonstrated high mechanical properties with several fibers testing +800 MPa failure strength. In relation to other studies, these mechanical properties appear to be substantially high, particular for pure lignin carbon fibers. Blends with cellulose or other polymers have tested in this range, however, 600+ MPa failure stress with 39+ GPa modulus for pure lignin carbon fiber samples, few have produced lignin carbon fiber with these mechanical properties [2, 6, 15-17]. While the LCF samples presented in this study show higher mechanical properties, there is still a large discrepancy between lignin carbon fiber and commercial PAN carbon fiber as displayed by the control used in this study (T700S). Thus, it appears that LCF in the near future will be utilized for non-structural or low strength composite applications or any applications not requiring high strength (chopped fiber composites, fillers, etc.).

It is difficult to track the various parameters throughout processing and manufacture that lead to improved mechanical properties, however, the best performing LCF sets tend to come from the Haake Minilab extruder. Spinning on the Haake extruder may lead to better mechanical properties for a variety of reasons mostly relating to the size and design of the extruder. The Haake is a twin screw that allows for improved mixing and melting of the lignin powder. In regards to the size of the extruder, it is much easier to manage the spinning. The Haake is a mini-extruder and, therefore, is much less complex than the AJA extruder with not as many parameters and variability. With only one heating zone, a smaller spinneret, and smaller chamber, the Haake is easy to control and adjust during extrusion. In addition, internal pressures are much lower due to less material being processed and a smaller barrel. Furthermore, residence time for lignin powder is considerably lower in the Haake compared to the AJA. Residence times can differ between 10-20 minutes. This additional time in the AJA barrel may lead to degradation, onset of crosslinking, and low M_w phenolic groups becoming volatile. These factors would lead to lower mechanical properties.

While the Haake Minilab is preferred for LCF production, it is unreasonable to think that this would be a suitable production technique for industrial demands. Spinning on the Haake Minilab produces approximately 10 g of lignin fiber in 45 minutes. For any sort of composite application, this is not enough material. In contrast, the AJA can produce larger amounts of lignin fiber but produces poor quality fibers. It appears that for lignin carbon fiber to be adopted by industrial partners, modified or custom extrusion equipment will be required for large scale production.

5.2 Single Fiber Fragmentation Results

The LCF samples demonstrated significant interface strengths for no sizing. The IFSS values ranged from 8-23 MPa. While this interface strength is relatively weak for commercial carbon fibers, these fibers are untreated and therefore may provide some advantage in manufacturing. Furthermore, the IFSS values for the best samples are significant such that these fibers can be used in applications where interface adhesion is required or utilized. The T700S IFSS values were approximately ~10.5 MPa which is consistent with other T700S/epoxy IFSS reported values [18]. In relation to other commercial fiber/resin IFSS values, the values report here are generally lower, however, the T700S is not optimized for the Super Sap 100/1000 used in this experiment [10]. Regarding the samples in this study, several LCF samples performed better than their PAN counterpart and may suit certain applications better than PAN carbon fiber.

The crack and delamination zone behavior immediately after saturation is another indicator of interface adhesion in addition to IFSS values. The IFSS values are dependent on several variables (fiber diameter, mechanical performance) and do not capture interface behavior; thus, these values do not always give a complete interfacial strength profile. Qualitative interface adhesion can be determined from the analysis of fiber fractures and delaminations at saturation. In regards to the lignin, LCF samples showed substantial crack propagation into the matrix resin signifying considerable interface strength. Additionally, delamination zones do not progress down the carbon fiber but rather begin growing into the resin similar to the fiber fracture or crack. The T700S samples in contrast show no crack propagation and as samples near saturation, delamination zones progress down the fiber. No transfer of stress or fiber fracture into the matrix material (resin), which are a preferred failure mechanism, are usual signs for a non-optimized interface and weak bonding [14]. Delamination zones on average

for T700S samples measured 403 µm compared to ~75 µm for LCF samples. Figure 26 demonstrates the behavior of each set of samples.

Figure 27 presents the interfacial characteristic curves for the carbon fiber samples. It is clear to see that there are three distinct groups for the curves (excluding the control). Fiber fractures are dependent on several things including interface adhesion and mechanical performance. If a LCF has poor mechanical properties, it should be expected that the fiber would fracture more than a fiber with better mechanical properties. This is exactly what is observed for C7 and C8.

To isolate only the shape of the curve and eliminate the influence of mechanical performance on the data, the curves are normalized against the maximum value. This method allows only the shape of the curve to be displayed (Figure 28). Thus, most samples tend to fall into a similar curve. For example, although C7 and C8 were dramatically different in Figure 27, it appears that they behave similarly to the majority of the LCF samples. The two samples with the weakest interface values, C4 and C6, show a different curve. For most of the LCF sets, it appears that each set reaches saturation roughly at the same point but C4 and C6 are delayed in initial onset of fiber fractures. With a weaker interface, it's possible that the interface is not engaged until a small displacement occurs. This could possibly be due to slight fiber slippage at the start of tensile loading.

The T700S fiber set is unique relative to the other LCF sets. It's similar in that T700S shows a slight delay into fiber fracture and is one of the last sets to reach saturation. The T700S fiber is considerable stronger and therefore, fiber fractures may not begin initially especially in comparison to the weaker LCF sets. It is also the most ductile carbon fiber used in this study and therefore, would need higher strains for fiber fracture. Thus, on average, it requires more strain

to reach displacement than most of the LCF samples. It is important to note that the T700S evaluated is sized for industrial applications. Unsized T700S would not perform as well.

The overall best performing LCF set is C1, which is also the only blend of lignin biomass sources (hardwood and switchgrass). While it is not thoroughly understood, the differing biomass sources tend to work well together as the coniferyl alcohol (G) and *p*-coumaryl alcohol (H) groups are more susceptible to cross-linking while the synapyl alcohol (S) groups allow for easier melt spinning [6, 19]. Hardwood sources tend to have much higher S to G ratios ranging from ~1.2 to 2.8 depending on the exact source while softwood and switchgrass sources tend to have lower S to G ratios (~0.52) and therefore more G and H groups [20-22]. This difference in monolingol groups allows the hardwood biomass to act as a plasticizer and the combination of the two sources produces a high quality carbon fiber [23, 24].

5.3 Thermal properties and Interfacial Strength

Through comparison of the results, there is a small trend between the derivative thermogravimetry (DTG) peak value and the average fiber fragment length, which would also correspond to the interface strength and mechanical properties. While it is not a strong trend, it is significant enough to say that the DTG peak may possibly be an early indicator of mechanical and interfacial performance (Figure 29). The DTG curve is determined from the derivative of a TGA curve and the peak is lowest value along the curve. Thus, it determines the temperature at which most of the material degradation occurs. Subsequently, as this peak value decreases in temperature, the material is degrading faster which could be related to the polymer Mw, polydispersity, or low Mw phenolic groups.

5.4 X-Ray Photoelectron Spectroscopy

XPS was used to determine the surface chemistry of the carbon fiber samples. There only seems to be a slight correlation between the interfacial data and XPS results. This might be due to the variability in the SFFT method and data interpretation for XPS. SFFT is arguably the most utilized procedure for interface evaluation, however, it is well known that there are large deviations and variability in the data due to sample preparation and testing. Generally, most SFFT results are not acceptable unless 15+ samples have been tested [9]. XPS is different in that the procedure is well defined but the data is open to interpretation and therefore, is highly user dependent [25, 26].

In analysis of the XPS, there was a single notable trend. When the oxidized carbon content is normalized against the fiber diameter, there is a negative correlation to IFSS (Figure 30). Therefore, it appears that as oxidized functional groups increase, the interfacial adhesion decreases. Polarized groups, which are typically oxidized carbon groups, tend to lead to high interface values, however, this finding is still under investigation. This trend may be influenced by the incorporation of failure strength into the equation for IFSS. The overall C-C bond percentage increases with higher strength fibers (oxidized carbon burns off at lower temperatures). Thus C-C bonding, which is related to the strength of the fibers, is related to the IFSS because IFSS is determined using the failure strength of the fibers. This finding is currently under investigation to determine if C-C bonding and IFSS are actually related or not.

6. CONCLUSION

- Eight lignin carbon fiber samples were evaluated for mechanical and interfacial properties including surface chemistry.
- Results indicate that production of lignin carbon fiber using a Haake Minilab extruder rather than a large pilot scale extruder produces better carbon fiber.
- For no sizing, lignin carbon fibers performed well with some fiber sets outperforming the T700S control sample.
- XPS results demonstrated that less oxidized carbon groups normalized to surface area leads to higher IFSS values.
- LCF seems to be ideal for applications requiring higher interface adhesion such as chopped fiber composites, fillers, or other.

ACKNOWLEDGEMENTS

This work is supported by TennEra, LLC. We would like to thank Adam McCall and Don Naab for their continued support.

REFERENCES

1. Baker, D.A. and T.G. Rials, *Recent advances in low-cost carbon fiber manufacture from lignin.* Journal of Applied Polymer Science, 2013. **130**(2): p. 713-728.
2. Sudo, K. and K. Shimizu, *A New Carbon Fiber from Lignin.* Journal of Applied Polymer Science, 1992. **44**: p. 127-134.
3. Brody, H. and L.M. Ward, *Modulus of Short Carbon and Glass Fiber Reinforced Composites.* Polymer Engineering and Science, 1971. **11**(2): p. 139-151.
4. Bozell, J.J., et al., *Solvent fractionation of renewable woody feedstocks: Organosolv generation of biorefinery process streams for the production of biobased chemicals.* Biomass and Bioenergy, 2011. **35**(10): p. 4197-4208.
5. Sammons, R., et al., *Characterization of Organosolv Lignins using Thermal and Ft-IR Spectroscopy Anaylsis.* BioResources, 2013. **8**(2): p. 2752-2767.
6. Baker, D.A., N.C. Gallego, and F.S. Baker, *On the characterization and spinning of an organic-purified lignin toward the manufacture of low-cost carbon fiber.* Journal of Applied Polymer Science, 2012. **124**(1): p. 227-234.
7. Kant, M. and D. Penumadu, *Dynamic mechanical characterization for nonlinear behavior of single carbon fibers.* Composites Part A: Applied Science and Manufacturing, 2014. **66**: p. 201-208.
8. Feih, S. and A.P. Mouritz, *Tensile properties of carbon fibres and carbon fibre–polymer composites in fire.* Composites Part A: Applied Science and Manufacturing, 2012. **43**(5): p. 765-772.
9. Feih, S., et al., *Establishing a Testing Procedure for the Single Fiber Fragmentation Test*. 2004, Risø National Laboratory.

10. Sager, R.J., et al., *Effect of carbon nanotubes on the interfacial shear strength of T650 carbon fiber in an epoxy matrix.* Composites Science and Technology, 2009. **69**(7-8): p. 898-904.

11. Naito, K., et al., *The effect of gauge length on tensile strength and Weibull modulus of polyacrylonitrile (PAN)- and pitch-based carbon fibers.* Journal of Materials Science, 2011. **47**(2): p. 632-642.

12. Zhou, Y., et al., *Tensile behavior of carbon fiber bundles at different strain rates.* Materials Letters, 2010. **64**(3): p. 246-248.

13. van der Zwaag, S., *The Concept of Filament Strength and Weibull Modulus.* Journal of Testing and Evaluation, 1989. **17**(5): p. 292-298.

14. Kim, B.W. and J.A. Nairn, *Observations of Fiber Fracture and Interfacial Debonding Phenomena Using the Fragmentation Test in Single Fiber Composites.* Journal of Composite Materials, 2002. **36**(15): p. 1825-1858.

15. Ma, Y., et al., *High-Strength Composite Fibers from Cellulose-Lignin Blends Regenerated from Ionic Liquid Solution.* ChemSusChem, 2015. **8**(23): p. 4030-9.

16. Kadla, J.F., et al., *Lignin-based carbon fibers for composite fiber applications.* Carbon, 2002. **40**(15): p. 2913-2920.

17. Nordström, Y., R. Joffe, and E. Sjöholm, *Mechanical characterization and application of Weibull statistics to the strength of softwood lignin-based carbon fibers.* Journal of Applied Polymer Science, 2013. **130**(5): p. 3689-3697.

18. Ramirez, F.A., L.A. Carlsson, and B.A. Acha, *Evaluation of environmental effects on polymer matrix composites by micromechanical and macromechanical tests.* Journal of Materials Science, 2008. **43**: p. 5230-5242.

19. Baker, F.S., *Low Cost Carbon Fiber From Renewable Resources*. 2010, Oak Ridge National Laboratory.

20. Davison, B., et al., *Variation of S/G Ratio and Lignin Content in a Populus Family Influences the Release of Xylose by Dilute Acid Hydrolysis.* Applied Biochemistry and Biotechnology, 2006. **129-132**: p. 427-435.

21. Bose, S.K., et al., *Lignin content versus syringyl to guaiacyl ratio amongst poplars.* Bioresour Technol, 2009. **100**(4): p. 1628-33.

22. Hu, Z., et al., *Chemical profiles of switchgrass.* Bioresour Technol, 2010. **101**(9): p. 3253-7.

23. Paul, R., et al., *Recent Progress in Producing Lignin-Based Carbon Fibers for Functional Applications.* GrafTech Internation Holdings Inc, 2015. **1**.

24. Norberg, I., et al., *A new method for stabilizing softwood kraft lignin fibers for carbon fiber production.* Journal of Applied Polymer Science, 2013. **128**(6): p. 3824-3830.

25. Ishitani, A., *Application of X-Ray Photoelectron Spectroscopy to Surface Analysis of Carbon Fiber.* Carbon, 1981. **19**(4): p. 269-275.

26. Yumitori, S., *Correlation of C1s chemical state intensities with the O1s intensity in the XPS analysis of anodically oxidized glass-like carbon samples.* Journal of Materials Science, 2000. **35**: p. 139-146.

CHAPTER III: MICROSTRUCTURAL CHANGES OF NONLINEAR ELASTIC PAN CARBON FIBER IN RESPONSE TO TENSILE LOADING

A version of this chapter is currently under review for publication.

This paper is first authored by Meek. The work presented herein is completed by Meek. Penumadu and Kant served in advisory roles.

Nathan Meek[1], Matthew Kant[1], Dayakar Penumadu[1]

[1]University of Tennessee at Knoxville, Civil and Environmental Engineering. 325 John D Tickle Building, Knoxville, TN 37996 USA

Corresponding Author: Dayakar Penumadu, dpenumad@utk.edu

Present/permanent address:

851 Neyland Drive, John D Tickle Building Office 325, Knoxville, TN, 37996

Keywords: Carbon Fiber, Polyacrylonitrile, Nonlinear Elastic, Wide Angle Diffraction, Small Angle Diffraction

ABSTRACT

In this study, wide- and small- angle diffraction (WAXS, SAXS) are used to analyze the structure of polyacrylonitrile (PAN) carbon fiber. Wide angle diffraction is used to identify lattice parameters such as d-spacings, stacking height of crystalline planes (Lc), average crystallize size (Lc), and various other features (void content, degree of graphitization). Small angle diffraction results show orientation and size distributions of pores/amorphous regions. Several analysis techniques were applied to small angle diffraction results to ensure accuracy. XRD Data collected is correlated to single fiber mechanical properties and a fiber model is

developed. Fiber modulus is heavily related to crystallite dimensions and orientation as well as pore structure. Authors hypothesize that the non-zero elastic constant, C_{44}, of carbon fiber arises from elastic planar motion within turbostratic carbon. As crystalline regions grow and expand, the lattice structure improves lowering the barriers for (002) quasi-graphene plane motion. This miniscule elastic planar motion can lead to a large nonlinear response to tensile loading especially for high crystallinity carbon fibers.

1. INTRODUCTION

Carbon fiber is an engineered material with a wide variety of applications ranging from wind turbine, automotive, and aerospace industries. It is produced from polymeric fibers through a series of thermal processes to convert into carbon or graphitic fiber. Carbon fiber has unique properties including a very high strength-to-weight ratio, making it an ideal material for applications where weight must be minimized without sacrificing strength and rigidity. Due to these material properties, carbon fiber demand and implementation have been continually rising for the past few decades particularly in transportation applications [1, 2].

Carbon fiber has been characterized and studied ever since its original development in the later part of the twentieth century, however, it has only been recently that the nonlinear response to tensile loading has been described in detail [3-5]. As carbon fiber is loaded in tension, the elastic or storage modulus tends to increase. This nonlinear elastic response of the carbon fiber is also known as elastic stiffening. In addition, as fiber placement and alignment in carbon fiber composites improves, this nonlinear response is also observed in composite performance [6]. In the past, fiber non-linearity has been observed but not discussed in detail due to limitations in testing resolution and non-optimized composite manufacture [7]. Stiffening or elastic strain hardening of carbon fiber has been explained by the reorientation of the crystalline planes but the

mechanism surrounding this phenomenon is not well understand or described. It also appears to be related to several other material parameters.

This study aims to characterize various PAN carbon fiber samples to develop mechanical-structure property relationships and mechanisms on a micro- and nano-scale leading to a nonlinear response to tensile loading.

2. THEORY

2.1 Wide-Angle Diffraction

Wide-angle diffraction (WAXS) is a common technique to characterize crystalline or amorphous regions in polymer samples. It has also been used extensively to determine morphology of fibrous samples for decades. In use with carbon fibers, several parameters describe the structure of carbon fibers including d-spacings of various crystalline planes ((002) and (100)), the stacking height of the graphene planes (Lc), the average crystallite size (La), and the orientation of the (002) planes to the fiber axis. It is important to note that the structural parameters determined in WAXS are relating to a graphite crystal. which has a hexagonal lattice structure with AB stacking of planes (Figure 31) [8, 9].

D-spacings are determined from the peak positions of the diffracting planes, (100) and (002). The (002) d-spacing (peak near 26°, χ=0) indicates the packing of the planes and is one half of the lattice constant "c". The (100) d-spacing is the lattice constant "a" of the hexagonal lattice cell. Using the positions of these peaks as well as the full-width half-max (FWHM), Lc and La are calculated using the Scherrer equation (eq. 12).

$$L_i = \frac{K\lambda}{\beta cos\theta} \quad [12]$$

In equation 12, L_i indicates the crystal dimension (c for stacking height, a for crystal size), K is a constant (*0.9 for L_c and 1.8 for L_a*), λ is the source wavelength, β is the FWHM of the peak of interest corrected for instrument broadening, and θ is the Bragg angle [10]. The orientation of the graphene planes ((002) planes) relative to the fiber axis is determined from the FWHM of a full χ scan at the peak of the (002) position. The breadth of this peak (also known as the misorientation angle) indicates the spreading of planar orientation within the fiber. Thus, as the FWHM decrease, the orientation of graphene planes increases [8].

In addition to Lc, the degree of graphitization (gp) is calculated from the (002) d-spacing following equation 13.

$$g_p = (0.344 - d_{(002)})/(0.344 - 0.3354) \quad [13]$$

In equation 2, 0.344 nm and 0.3354 nm are the interplane spacing for turbostratic carbon and fully graphitic carbon respectively [10].

2.2 Small-Angle Diffraction

Two different methods were used to analyze the small angle diffraction data: (1) Ruland's Streak Analysis (RSA) and (2) Maximum Entropy (MaxEnt) developed by Jemian et al. RSA produced average lengths for microvoids while MaxEnt calculated pore diameters and distributions based on simple assumed geometries, such as a spheroid, cylinder, or disc [11-13]. While both techniques gave similar results, each analysis is slightly dependent on user inputs (q-range, smoothing functions, geometries). Therefore, there is some variation in the data depending on the user; however, correlation to other reported literature and an agreement between the two analysis techniques gave more confidence in the determined pore sizes [1, 13].

RSA was developed by Perret, Ruland and expanded on by Thunemann [12, 13]. Diffraction patterns (also known as pinhole patterns, pole figures) show streaking from the elongation and misorientation of the domains (Fig. 32). For carbon fiber, these domains are either amorphous regions or micropores depending on manufacturing temperatures of the carbon fiber.

The basic principle of RSA is to separate the effect of streaking from misorientation and the size of the scattering domains. Ruland expanded on Wilke and applied several analytical functions to the orientation distribution. Thus, RSA functions by fitting azimuthal scans at increasing s (scattering or momentum length) with Gaussian or Lorentzian distributions to determine the breadth of the intensity (Fig. 33) [14].

Once the observed breadth of the intensity is determined for each s, the length and misorientation of the scattering domains can be determined using equation 14 if Gaussian functions are fitted to the orientation distribution.

$$s^2 {B_{obs}}^2(s) = {B_p}^2 + \frac{1}{\langle L \rangle^2} + s^2 {B_g}^2 \qquad [14]$$

In equation 3 s is the scattering length, B_{obs} is the apparent breadth of the orientation distribution at s, B_p is the instrumental broadening, $\langle L \rangle$ is the average longitudinal extension, and B_g is true integral breadth of the orientation distribution (indicator of misorientation). If a Lorentzian is the proper model for the diffraction orientation distribution, equation 4 is used instead of equation 3. The differences in eqs. 3 and 4 stem from the differences in fitting functions used. The data presented in this study used Lorentzian fits and therefore, used equation

15 to determine misorientation and length of domain. This technique and derivations of equations are discussed in detail elsewhere [13, 14].

$$sB_{obs}(s) = B_p + \frac{1}{\langle L \rangle} + sB_g \quad [15]$$

While RSA gives accurate length information regarding scattering domains, it does not provide reasonable information on domain or pore diameter. Diameters can be determined making assumptions about the overall shape and aspect ratio of the domains, however, Irena – Igor software was used to determine these diameters. The Maximum Entropy (MaxEnt) macro program imbedded in the Irena software is used to determine pore diameters and distributions. It operates by attempting to solve the scattering equation (eq. 16).

$$I(Q) = \sum_k |\Delta\rho_k|^2 S_k(Q) \sum_{i_k} |F_k(Q, D_{ik})|^2 V_k(D_{ik}) f_k(D_{ik}) \Delta D_{ik} \quad [16]$$

In equation 16, the subscript *i* denotes all bins in the size distribution, *k* denotes different populations with it's own binning index i_k, D is the particle dimension, S(Q) is the structure factor, F(Q, D) is the scattering form factor, V(D) is the particle volume, f(D) is the volume size distribution, and $|\Delta\rho|^2$ is the scattering contrast. MaxEnt attempts to solve the equation by restricting several input parameters to minimize errors in the model. Further details are not discussed here as this is outside the scope of this paper [11, 15].

Reported SAXS results in this article use the combination of the two techniques since both techniques do not provide a full SAXS analysis. In processing the SAXS data, the structural model for the domain assumes a spheriod scatterer with an aspect ratio of five. Five was selected

as it corresponded well to the data using the Irena software; a cylinder with aspect ratio of five gave a length that was similar to RSA.

3. EXPERIMENTAL METHODS AND MATERIALS

3.1 Polyacrylonitrile Carbon Fiber

Several industrial PAN carbon fibers from Toray were selected for this study. T300, T400, T700S, T800, M40J, and M50J were analyzed. Table VIII summarizes their properties. These properties are reported by the manufacturer (Toray).

3.2 MTS Nano Bionix Universal Testing Machine (UTM)

To characterize the carbon fiber samples, single fibers were tested using a MTS Nano Bionix Universal Testing Machine (UTM), which utilizes a Nano-Mechanical Actuating Transducer (NMAT) to determine load on sample. The NMAT contains three components: (1) an electromagnetic coil, (2) capacitance gauge, and (3) supporting leaf springs. The equipment can precisely measure single fiber samples in load and displacement on the order of nN and nm respectively. In addition, the NMAT can apply nano-oscillations to a global tensile or compression test to determine static and dynamic properties in a single test. A more detailed explanation of this system including theory is outside the scope of this article and explained elsewhere [3].

3.3 PANalytical (Philips) X'Pert Diffractometer

A Philips X'Pert Diffractometer was used for characterization of the (002) plane, (100) plane, and orientation of the (002) plane. The X'Pert is a multi-axis diffractometer with a Cu Kα stationary source, double goniometer platform, and cradle with χ rotation of ±92°. With each reflection, the d-spacings and FWHM were determined leading to the calculation of Lc (*stacking height of graphene planes*) and La (*crystallite size parallel to graphene planes*). Carbon fiber

samples were scanned using transmission point diffraction following a procedure outlined by Spruiell [8].

3.4 SAXSLab Ganesha

For WAXS-SAXS pinhole patterns, carbon fiber samples were analyzed using a SAXSLab Ganesha Diffractometer located at the Shared Materials Instrumentation Facility located at Duke University. The Ganesha Diffractometer uses a Cu 50kV Xenocs Genix ULD SL X-ray source and 170um pixel-spaced, single photon counting Dectris Pilatus 300k 20Hz Detector. The q minimum range is 0.007-0.07$Å^{-1}$ and q maximum range is 0.18-2.8$Å^{-1}$.

The Ganesha Diffractometer allowed for the collection of small angle data and pinhole patterns, however, the maximum 2θ allowable is 40° and therefore, additional scans required for the (100) plane were needed on another diffractometer (Philips XRD).

3.5 Correlation between SAXSLab Ganesha and Philips XRD

To ensure accuracy and consistency, both diffractometers were calibrated with known standards and similar scans were collected on each diffractometer to compare results. Several (002) WAXS scans (d-spacing and FWHM) were compared and showed a difference of less than 0.01% or no difference.

3.6 Scanning Electron Microscopy

Scanning electron microscopy was used to capture the differences in fiber samples, measure fiber diameters, and if possible, observe micro-, nano- pores. Samples were prepared by mounting to a SEM sample block and cut using a razor blade. To remove any fiber fragments, compressed air was applied to the cut fiber tows. Once sample preparation was complete, the samples were placed in a FE-SEM LEO 1525 microscope to complete SEM work.

4. RESULTS

4.1 Wide Angle Diffraction

Table IX summarizes the WAXS data for the PAN carbon fiber samples from data collected in Figures 34 and 35. T300, T400, and T700 demonstrate similar results with d-spacings and crystallite dimensions that are generally the same. T800 shows slight larger crystallite dimensions and M40J/M50J display the largest crystallite dimensions.

4.2 Small Angle Diffraction

From the small angle pinhole patterns and exported data, RSA and Irena were used to process the data displayed in Figure 36. The summary of these results are presented in Table X. Results are similar for the T-series fibers but the M-series fibers (M40J, M50J) show significant pores size and distributions.

4.3 Mechanical Properties of Carbon Fibers

Table XI summarizes the mechanical properties for the carbon fiber and stress strain curves are presented in Figure 37. The behavior of the storage (elastic) modulus in response to tensile strain is displayed in Figure 38. The parameter SM (0) indicates the initial storage modulus upon testing and dSM/dε describes the slope of storage modulus versus strain (determined from Figure 38).

4.4 Scanning Electron Microscopy

SEM micrographs are visible in Figures 39 and 40. Fibers appear to be largely kidney bean shaped excluding T700 and T800. These two fibers are circular. Specimen diameters were taken from SEM for accurate results.

5. DISCUSSION

This section refers to Figures 31 to 48 and Tables VIII to XI.

5.1 Structure Property Relation to Nonlinear Response of PAN CF

The development of the elastic modulus of carbon fibers has been studied since the 1970's but only recently received significant attention due to improvements in testing and measurement [3-5, 7]. In addition, this nonlinear response to loading appears to be present in carbon fiber composites which affects overall composite properties and performance [6, 16, 17]. Kant, Penumadu completed an in-depth mechanical analysis of the same Toray carbon fiber samples presented here [3]. Mechanical properties were collected and analyzed in a similar fashion to Kant. Table XI and Figure 37-38 displays the mechanical data from the carbon fiber samples. Fiber diameters were collected from Figures 39-40 for mechanical data processing. Correlation of the nonlinear response to initial storage modulus is displayed in Figure 41 consistent with Kant.

As seen in the data from Table IX and Table XI, the stiffening response of the carbon fiber appears to be directly correlated to the crystallinity. To observe this relationship, crystalline parameters were plotted against mechanical data (Figure 42). Trends display a near perfect correlation between crystallinity and nonlinearity. This indicates that the crystalline regions are directly affecting the non-linear response of the carbon fiber. Several studies have suggested it is the reorientation and straightening of the crystallites that gives rise to the nonlinear response of the carbon fiber [18]. Crystallites are often warped or twisted within the fiber before any external forces are applied and in response to tensile loading these crystallites "straighten", however, the mechanisms for this structural reorganization is not well understood on a nano-structural level. In addition, this appears not to be the only factor in the non-linear response because carbon fiber

with more orientated graphene planes to the fiber axis display a higher non-linear response (Figure 43). Thus, more orientated carbon fiber shows a larger nonlinear response.

Samples that are more crystalline show a more perfect lattice structure in those crystalline regions; the degree of graphitization increases as these crystalline regions expand. As the structure becomes more similar to graphite, the nonlinear response increases (Figure 43). To understand what is happening as the degree of graphitization is increasing, one must first understand the crystal structure of graphite. Graphite is composed of stacked carbon layers known as graphene planes. These graphene planes stack in an AB sequence and form a hexagonal close packed structure (HCP). Bonding within the planes is covalent while bonding between the planes are weak Van der Wall interactions. This means that graphite is highly anisotropic depending on the direction of the graphene planes. Therefore, as crystalline regions grow within carbon fiber, the lattice structure of these crystalline regions improves to form a structure that increasingly becomes similar to graphite. Figure 44 demonstrates a simplified diagram showing the difference between the two structures [9, 19].

Within graphite, weak Van der Wall interactions between planes allow for graphene plane mobility. Planar mobility within the graphite structure leads to a small non-zero elastic constant. In addition, bond stretching within a monolayer of graphene can contribute to a nonlinear response. Consequently, as the lattice structure quality improves and the crystallite grows, there is a larger nonlinear response from the carbon fiber due to vertical quasi-graphene plane mobility and bond stretching [9, 19-22].

There are several barriers to plane mobility (movement and rotation), which are related shear and bonding energies. These energies are highly affected by defects within the lattice structure [21]. Turbostratic carbon is similar to graphite; however, it is not nearly as pristine, and

(002) planes usually contain imperfections such as with vacancies, twin planes, substitutions, and interstitials. These imperfections lead to relative misalignment of planes meaning that adjacent planes are not coordinated with one another. Certain areas of turbostratic carbon tend to contain perfect graphitic structure depending on the final temperature of fiber processing, but in general, turbostratic carbon is an imperfect lattice structure [23, 24].

As turbostratic carbon nears graphitic carbon and the overall quality of the carbon fiber improves, the ability for planar motion increases. Figure 45 demonstrates two example carbon fiber samples. As d-spacings decrease, defects and other barriers must decrease as well otherwise smaller d-spacings would not be possible. With an improved lattice structure, barriers to plane motion are lowered and a larger elastic constant is observed. This would also explain the relationship between misorientation angle and stiffening. With more orientated graphene planes to the fiber axis, the tensile forces on the fiber are more parallel to the graphene planes causing more planar motion and a larger nonlinear response (Figure 43). M50J shows the smallest misorientation meaning the quasi-graphene planes are highly orientated to the fiber axis relative to the other fibers. Based on planar motion, the highest stiffening or elastic constant expected would be for M50J as well and the results show this trend.

5.2 Pore Effect on Fiber Properties

Determined pore sizes range from approximately ~4 nm to ~9 nm in length and ~1 nm to ~3 nm in diameter as shown in Table X. These results appear to be approximately ± 1nm in difference relative to other studies on carbon fiber, however, the overall trends are similar [23, 25]. As crystallites grow within the fiber, pores begin to appear and grow as well (Figure 46). To explain the relationship of pore size to crystallite size, assume the fiber is a fixed cylindrical volume. Smaller crystallites fill the volume more efficiently, therefore, pores are smaller and

more numerous since they fill the small pockets between the crystallites. With larger crystallites, they do not fill the volume as efficiently and pores must fill in the spaces between these large elongated crystallites. Because of this, high modulus carbon fiber (and therefore high crystallinity carbon fiber) tends to have large pores [18, 26].

It's important to discuss pore size/volume in discussing crystallinity, reorientation, and the nonlinear response because with larger pores, the overall crystallites have more freedom to move. As discussed in 5.1, when crystalline regions expand, they tend to elongate but not in a perfect fashion. The crystallites become twisted and abnormal as they struggle for expansion volume within the fiber. Pores along the extended crystalline regions must develop to fill the overall fiber volume. Thus, crystalline regions have little room to elongate but can easily twist or "straighten" in response to tensile forces [18]. This has also been described as pore collapse and seems to be related to elastic stiffening [7]. Figure 47 demonstrates how as the average pore diameter increases, stiffening also increases. In addition, pore size seems to be loosely related to average failure strain. This would be expected as pores are large defects within the fiber and as these grow, the cross sectional area experiencing load would decrease leading to early failure.

5.3 RSA and Irena SAXS Data Analysis

Most of the data analysis of SAXS in comparison to WAXS and mechanical properties was completed using the Irena values, however, RSA was completed as an additional analysis technique and to provide more accuracy to the data. The relation of RSA data to Irena data is given in Figure 48. There is a near perfect trend for the two analysis techniques, which is logical. As the pore diameter increases (completed with Irena), the length of the pore also increases (completed by RSA).

6. CONCLUSION

- As crystalline regions grow within a carbon fiber, the crystal lattice becomes more perfect as seen in decreasing d-spacings and FWHM. In addition, pores must develop to accommodate large crystallites and fill the rest of the fiber volume.
- Due to weak Van der Wall interactions between quasi-graphene layers in the turbostratic carbon, planar mobility is less restricted as crystalline regions grow. These crystalline regions slowly become graphite as they develop and expand.
- The large crystalline regions, planar mobility, and pore volume allow nano- and microstructural "straightening" of the carbon fiber giving rise to a non-zero elastic constant and increase in storage modulus during tensile loading.

ACKNOWLEDGMENTS

We would like to thank Mr. Jimmy Thostenson at Duke University for his help with SAXS. This research is partially supported by the general infrastructure grant of DOE-Nuclear Energy University Program (DE-NE0000693) and the Nuclear Engineering University Program (NEUP) Award Number 12-3528.

REFERENCES

1. Diefendorf, R.J. and E. Tokarsky, *High Performance Carbon Fibers.* Polymer Engineering and Science, 1975. **15**(3): p. 150-159.
2. Park, S.-J., *Carbon Fibers*. 2015, Springer
3. Kant, M. and D. Penumadu, *Dynamic mechanical characterization for nonlinear behavior of single carbon fibers.* Composites Part A: Applied Science and Manufacturing, 2014. **66**: p. 201-208.
4. Djordjevic, I.M., et al., *Non-Hookean Elastic Behavior and Crystallite Orientation in Carbon Fibers.* Journal of Composite Materials, 2010. **44**(14): p. 1717-1727.
5. Djordjevic, I., D. Sekulic, and M. Stevanovic, *Non-linear elastic behavior of carbon fibres of different structural and mechanical characteristic.* Journal of the Serbian Chemical Society, 2007. **72**(5): p. 513-521.
6. Yokozeki, T., T. Ogasawara, and T. Ishikawa, *Nonlinear behavior and compressive strength of unidirectional and multidirectional carbon fiber composite laminates.* Composites Part A: Applied Science and Manufacturing, 2006. **37**(11): p. 2069-2079.
7. Voet, A., J.-C. Morawski, and J.-B. Donnet, *Dynamic Mechanical Properties of Carbon Fibers.* Carbon, 1975. **13**: p. 465-468.
8. Paulauskas, F.L., T.L. White, and J.E. Spruiell, *Structure and Properties of Carbon Fibers Produced using Microwave-Assisted Plasma Technology, Part 2*, in *2006 SAMPE* 2006, Society for the Advancement of Material and Process Engineering.
9. Chung, D.D.L., *Review Graphite* Journal of Material Science, 2002. **37**: p. 1-15.
10. Anderson, D., *Carbon Fiber Morphology - Expanded Wide Angle XRD Studies*, A.F.S. Command, Editor. 1991.

11. Jemian, P.R., et al., *Characterization Of 9Cr-IMoVNb Steel By Anomalous Small-Angle X-Ray Scattering.* Acta Metallurgica et Materialia, 1991. **39**(11): p. 2477-2487.

12. Perret, R. and W. Ruland, *Single and Multiple X-Ray Small-Angle Scattering of Carbon Fibres.* Journal of Applied Crystallography, 1969. **2**.

13. Thunemann, A. and W. Ruland, *Microvoids in PAN Fibers - A Small-Angle X-ray Scattering Study.* Macromolecules, 2000. **33**: p. 1848-1852.

14. Stribeck, N., *Ruland's Streak Method*, in *X-Ray Scattering of Soft Matter*. 2007, Springer Laboratory p. 201-205.

15. Ilavsky, J. and P.R. Jemian, *Irena: tool suite for modeling and analysis of small-angle scattering.* Journal of Applied Crystallography, 2009. **42**(2): p. 347-353.

16. Yokozeki, T., T. Ogasawara, and T. Ishikawa, *Effects of fiber nonlinear properties on the compressive strength prediction of unidirectional carbon–fiber composites.* Composites Science and Technology, 2005. **65**(14): p. 2140-2147.

17. Ishikawa, T., M. Matsushima, and Y. Hayashi, *Hardening non-linear behavior in longitudinal tension of unidirectional carbon composites.* Journal of Material Science, 1985. **20**: p. 4075-4083.

18. Zhou, G., et al., *Microstructure difference between core and skin of T700 carbon fibers in heat-treated carbon/carbon composites.* Carbon, 2011. **49**(9): p. 2883-2892.

19. Gray, D., A. McCaughan, and B. Mookerji, *Crystal Structure of Graphite, Graphene and Silicon.* Physics for Solid State Applications, 2009. **6.730**.

20. Kalosakas, G., et al., *In-plane force fields and elastic properties of graphene.* Journal of Applied Physics, 2012. **113**(13).

21. Popov, A., et al., *Barriers to motion and rotation of graphene layers based on measurements of shear mode frequencies.* Chem. Phys. Lett., 2012. **536**(82).

22. Popov, A.M., et al., *AA stacking, tribological and electronic properties of double-layer graphene with krypton spacer.* J Chem Phys, 2013. **139**(15): p. 154705.

23. Li, D., et al., *Structural evolution during the graphitization of polyacrylonitrile-based carbon fiber as revealed by small-angle X-ray scattering.* Journal of Applied Crystallography, 2014. **47**(6): p. 1809-1818.

24. Hoffman, W., *Material Science of Carbon.* 2004.

25. Ozcan, S., F. Vautard, and A.K. Naskar, *Designing the Structure of Carbon Fibers for Optimal Mechanical Properties.* 2014. **1173**: p. 215-232.

26. Zhua, C.-z., et al., *2D SAXS-WAXD Analysis of PAN Carbon Fiber Microstructure in Organic-Inorganic Transformation* Chinese Journal of Polymer Science 2013. **31**(5): p. 823-832.

CHAPTER IV: VACUUM ASSISTED RESIN TRANSFER MOLDING FOR COMPOSITE PRODUCTION

ABSTRACT

This chapter serves to present the procedure and knowledge obtained when lignin and PAN CF composites were produced. The development of the VARTM system and various modifications are discussed first followed by implementation of various in-situ monitoring systems. During the production of test composites, the VARTM system underwent a multitude of modifications to improve the manufacture of composites (addition of a double vacuum bag, alternative preform stack, support plate and heat sink). After a procedure was established, several fiber/resin composite systems were produced using the VARTM system.

Vacuum Assisted Resin Transfer Molding

Background and Development

Advanced fiber reinforced composites were developed in the 50's and 60's and have continued to rise in use and applications since their original development [1]. Fiber reinforced composites can be manufactured in a wide variety of methods usually tailored for the final composite application. For example, filament winding composite manufacture is ideal for producing composites in cylindrical shapes, which are implemented in pressure vessels, tubing, etc. Some other common manufacturing techniques are Resin Transfer Molding (RTM), open molding, pultrusion, and reusable bag infusion.

Vacuum-Assisted Resin Transfer Molding (VARTM) is a technique that allows for flexibility in part dimensions and complexity. It is also relatively cheap to implement, as it does not require high temperature for cure, expensive tooling/molds, and costly control systems. Because of these features, it is the manufacturing technique of choice for laboratories studying various composite types and layups, companies with complex parts or changing designs, or low

production runs (<500 units or less). VARTM utilizes a vacuum bag to infuse resin into the fiber fabric or, if prepregs are used, pulls a vacuum on the part during a high temperature cure. The final composite part is produced from carbon fiber fabrics placed within a preform or 'stack'.

Preform Stack for VARTM

For each composite part produced using the VARTM system, a preform is required. A preform or "stack" is a series of nettings, fabrics, and carbon fiber that produce the final part. The preform developed here uses a unique layup for several reasons. The preform is similar to other VARTM preforms, however, this preform utilizes a double resin flow netting and therefore does not require a resin brake which is discussed in the next section. Beginning from the bottom, the stack normally consists of (1) a sheet of mylar, (2) release ply, (3) carbon fiber fabric or prepreg, (4) release ply, (5) resin flow media or breather, and (6) a sheet of mylar. Mylar is certainly not necessary, however, it protects from defects in the mold or folds in the vacuum bag that can on occasion transfer to the part. The release ply is used to remove the part easily from the preform after it is finished curing and the flow media/breather allows for resin or air to flow depending on whether carbon fiber fabric or prepregs are used.

Double Netting and Removal of Resin Brake

The VARTM system developed in this study has a few differences from other VARTM systems (Figure 49). First in some VARTM systems, parts that are produced using a 'resin brake'. A resin brake is an area of netting after the preform stack that allows the resin to fully infuse the part and form a linear flow front before the vacuum line. The most important reason for implementing this feature in a VARTM system is that the part becomes fully infused before the resin reaches the vacuum line. As resin flows over the part, the edge of the part can "miss"

infusion because the resin reaches the vacuum line or begins gelation (onset of crosslinking). To counteract this phenomenon, a double resin flow netting was implemented: one on top and bottom (Figure 50). Using Darcy's Law (equation 17), the cross-sectional flow into the part is doubled by doubling the resin flow netting [2, 3]. This double netting dramatically increased flow over the part allowing for faster infusion and complete impregnation of the carbon fiber fabric even with aggressive-cure epoxies/resins. Therefore, the time for infusion is effectively reduced by 50 percent and double netting ensures complete infusion.

$$q_x = -\frac{k_x A}{\mu}\frac{\delta P}{\delta x} \quad [17]$$

In equation 17, q is the flow rate, k is the permeability, A is the cross-sectional area for flow, μ is the resin viscosity, and δP/δx is the differential in pressure as a function of x (distance).

Double Vacuum Bag

During the development of the VARTM system, it was found that a double vacuum bag (DVB) produced higher quality composites relative to a single vacuum bag. A double vacuum bag is an additional vacuum bag over the first vacuum bag. Having a DVB-VARTM system allows for the production of higher quality composites, ensures a seal around the part, and varying the vacuum of the inner to outer bag gives some flexibility in part geometry [4, 5]. In addition, the inner vacuum bag deforms and stretches quite dramatically in the production of large or complex composite parts. The second vacuum bag acts to hold the inner bag in place and adds further compaction to the part thus preventing the inner bag from relaxation or pulling away [6]. As consistent with other reported literature, a breather cloth or netting is placed in between the two bags (inner and outer) to facilitate air movement. Figure 51 displays the schematic for

the setup of the VARTM system. With double resin flow nettings around the part and double vacuum bags for infusion, composite produced were high quality with volume fractions typically above 50 percent.

Results for lignin composites manufactured are listed in Chapter I while data collected on PAN CF composites is outside the scope of this thesis. Produced composites are visible in Figure 52.

REFERENCES

1. Tsai, S., Three decades of composites activities at US Air Force Materials Laboratory. Composites Science and Technology, 2005. 65(15-16): p. 2295-2299.

2. Humbert, D., Modeling of Resin Transfer Molding of Composite Materials with Oriented Unidirectional Plies, in Chemical Engineering. 1995, Montana State University.

3. Grimsley, B.W., et al., Preform characterization in VARTM process model development. 2004

4. Hou, T.J., J.M. Bai, and J.M. Baughman, Processing and Properties of a Phenolic Composite System. Journal of Reinforced Plastics and Composites, 2006. 25(5): p. 495-502.

5. Hou, T.J. and B.J. Jensen, Evaluation of Double-Vacuum Bag Process for Composite Fabrication. 2004, NASA Langley Research Center.

6. Mahendran, M., An improved mouldness manufacturing method for foam-core composite sandwich structures. 2010, Ottawa-Carleton Institute for Mechanical and Aerospace Engineering.

CONCLUSION

1. Lignin fiber was successfully spun and converted into carbon fiber following stabilization and carbonization. LCF composites were produced as well using VARTM.
2. LCF mechanical properties ranged from 250-800MPa failure strength and 30-45 GPa Young's modulus. Structural analysis of the LCF showed the presence of largely amorphous carbon.
3. LCF demonstrated significant interfacial bonding with a high biomass epoxy indicating that although LCF is relatively weak, it may be well suited for chopped fiber composite applications.
4. X-Ray Diffraction of PAN carbon fiber results led to a new theory relating the elastic nonlinear response to graphene planar motion.
5. Modifications to the VARTM composite production technique, such as double bagging and a unique preform stack, produced high quality composites.

APPENDIX

Ruland's Analysis Through Matlab

The following is matlab code for the processing of SAXS data with Ruland's Streak Analysis. It processing the data using a Gaussian fit, however, it can be modified for a Lorentzian fit through changing the 'fit' command.

```
clear all;
clc;
close all;

%Put in filename for .txt export from SAXSGUI, file must be in working
%folder

filename = 'T800_SAXS_rotate180_samplethickness1-5_gauss5-1.txt';
Data = csvread(filename);

%Input parameters
%set phi bounds for analysis, NOTE: scale should be by 2 deg of phi
Phi_1 = 100;
Phi_2 = 250;
qslice = 100; %be aware of the range of q, [A^-1], 10,20,30,40 is usual
% SAXS data begins at 0.00153 and goes up in delq of 0.00153

% when going from SAXS to MAXS, etc. CHANGE LIMITS ON FIGURES, delq will
% also change

q = Data(:,1);
phi = Data(:,2);
I = Data(:,3);

%Log(I) calculation
    LogI = zeros(size(Data(:,1)));
    LogI = log(I);

%Remove NaN, -Inf from Data
    [row, col] = find(isnan(LogI));
    LogI(row,:) = [0];
    [row2, col2] = find(isinf(LogI));
    LogI(row2,:) = [0];
    %removing negative intensities
    LogI(:,1) = (LogI(:,1) > 0) .* LogI(:,1); %double check

%Reshaping matrices and separating q and LogI
gd =[q,LogI];
gd2=reshape(gd,181,[]);
gd2s = size(gd2,2);
qdata = wkeep(gd2,[181 gd2s/2],'l');% grabbing left side of matrix, q
LogIdata = wkeep(gd2, [181 gd2s/2], 'r');%grabbing right side of matrix, LogI
```

```
%Grab phi 100-250 in LogI
LogIdata1 = LogIdata([Phi_1/2:Phi_2/2],:);
phi1 = transpose(Phi_1:2:Phi_2);

%subtract background, zero if negative
for jj = 1:qslice;
    LogIdata1(:, jj) = squeeze(LogIdata1(:, jj)) - LogIdata1(1,jj); %subtract
background
    LogIdata1(:,jj) = (LogIdata1(:,jj) > 0) .* LogIdata1(:,jj);
end

% gaussian fit, pulling out c-parameter
CofM = zeros(qslice,3); %need to change based on data size
for jj = 1:qslice;
    m = max(LogIdata1(:,jj))+0.001;
    NormLogIdata1(:, jj) = squeeze(LogIdata1(:, jj)./m); %divide by maximum
to normalize
    f = fit(phi1,LogIdata1(:,jj),'gauss1');

    plot(f,phi1,LogIdata1(:,jj))
    axis([100 250 0 8])

    legend off
    hold on

    Cof = coeffvalues(f);
    CofM(jj,:) = Cof;
end
    xlabel('Phi')
    ylabel('Log(I)')

%Plotting q slices
figure
subplot(2,3,1)
    plot(fit(phi1,LogIdata1(:,5),'gauss1'),phi1,LogIdata1(:,5))
    axis([100 250 0 8])
    title('q slice 5')
    legend off
    xlabel('Phi')
    ylabel('Log(I)')
subplot(2,3,2)
    plot(fit(phi1,LogIdata1(:,10),'gauss1'),phi1,LogIdata1(:,10))
    axis([100 250 0 8])
    title('q slice 10')
    legend off
    xlabel('Phi')
    ylabel('Log(I)')
subplot(2,3,3)
    plot(fit(phi1,LogIdata1(:,15),'gauss1'),phi1,LogIdata1(:,15))
    axis([100 250 0 8])
    title('q slice 15')
    legend off
    xlabel('Phi')
    ylabel('Log(I)')
```

```
subplot(2,3,4)
    plot(fit(phi1,LogIdata1(:,20),'gauss1'),phi1,LogIdata1(:,20))
    axis([100 250 0 8])
    title('q slice 20')
    legend off
    xlabel('Phi')
    ylabel('Log(I)')
subplot(2,3,5)
    plot(fit(phi1,LogIdata1(:,25),'gauss1'),phi1,LogIdata1(:,25))
    axis([100 250 0 8])
    title('q slice 25')
    legend off
    xlabel('Phi')
    ylabel('Log(I)')
subplot(2,3,6)
    plot(fit(phi1,LogIdata1(:,30),'gauss1'),phi1,LogIdata1(:,30))
    axis([100 250 0 8])
    title('q slice 30')
    legend off
    xlabel('Phi')
    ylabel('Log(I)')

%Breadth is determined from FW(20)M = 2*sqrt(2*log(20))*c
%Exported matrix q_c is q values with c parameters from Gauss fits
cPar = CofM(:,3);
qtot = transpose(qdata(1,:));
q_c = [qtot(1:qslice) cPar]


% Tri-Surface Plot generation
figure
tri = delaunay(q,phi);
trisurf(tri,q,phi,LogIdata,'EdgeColor','none');
axis([0 0.15 100 250]);
view(60,20);
```

TABLES

TABLE I: AVERAGE SINGLE FIBER MECHANICAL RESULTS OF LIGNIN CARBON FIBER FOR COMPOSITE MANUFACTURE (AVERAGE ± ST. DEV.)

μ ± σ	**Specimen Diameter**	**Modulus**	**Failure Strain**	**Failure Stress**
# of Tests	**um**	**GPa**	**mm/mm**	**MPa**
27	16.2 ± 6.0	35.1 ± 6.1	0.017 ± 0.004	587 ± 192

TABLE II: THE INTERFACIAL RESULTS OF LIGNIN CARBON FIBER FOR COMPOSITE MANUFACTURE (AVERAGE ± ST. DEV.)

μ ± σ	**Fiber Length**	**Delamination Length**	**IFSS**
Measurements	**μm**	**μm**	**MPa**
431	228.1 ± 109.3	96.0 ± 35.5	16.7

TABLE III: THE MECHANICAL RESULTS FOR LIGNIN CARBON FIBER COMPOSITE USING VIC-3D AND MTS858 (AVERAGE ± ST. DEV.)

μ ± σ	**Failure Stress (MPa)**	**Failure Strain**	**Modulus (GPa)**
Samples	**MPa**	**mm/mm**	**GPa**
6	85.0 ± 11.5	0.0094 ± 0.001	9.1 ± 0.6

TABLE IV: PROCESSING CONDITIONS FOR LIGNIN CARBON FIBER SAMPLES USED IN INTERFACIAL TESTING

		Organosolv		Spinning		
	Precursor	**Temp.**	**Pre-processing**	**Equipment**	**Stab. Rate**	**Carb. Rate**
Sample	**NA**	**°C**	**NA**	**NA**	**°C/min**	**°C/min**
C1	Hardwood-Grass Blend	160	Blending of powders	Haake Minilab	0.05	3.8
C2	Hardwood	170	-	Haake Minilab	0.05	3.8
C3	Hardwood	160	-	Haake Minilab	0.05	3.8
C4	Grass, PEG	160	Pelletized	Haake Minilab	0.017	3.8
C5	Grass	140	Pelletized	AJA	0.26	3.0
C6	Hardwood	130-160	Additional drying	AJA	0.1	3.8
C7	Grass	140	Pelletized	AJA	0.025	3.8*
C8	Grass	140	Pelletized	AJA	0.025	3.8

AJA = Alex James and Associates *Carbonized in reducing environment

TABLE V: DSC AND TGA VALUES FOR LIGNIN POWDER SAMPLES

Sample	Tg °C	Delta Cp (J/g.°C)	DTG** peak °C	DTG** Peak value (%/min)	Temp. @ 5% mass loss °C	Temp. @ 10% mass loss °C	Char %
C1	120	0.43	378	-4.74	261	302	36.8
C2	128	0.34	378	-3.28	256	301	41.6
C3	121	0.38	375	-3.99	251	284	34.2
C4	108	0.28	388	-4.33	245	281	35.8
C5*	108	0.36	365	-4.3	243	281	33.7
C6	Thermal data not available						
C7*	108	0.36	365	-4.3	243	281	33.7
C8*	108	0.36	365	-4.3	243	281	33.7

*Same biomass precursor

**Derivative Thermogravimetry

TABLE VI: THE MECHANICAL PROPERTIES OF CARBON FIBER SAMPLES AND WEIBULL STATISTICS (AVERAGE ± ST. DEV.)

μ ± σ	**Fiber Dia.**	**Failure Stress**	**Failure Strain**	**Modulus**	**Shape***	**Scale***	**R^2***
Sample	**μm**	**MPa**	**%**	**GPa**	**N/A**	**MPa**	**N/A**
C1	16.3 ± 1.4	609.7 ± 189.3	1.16 ± 0.38	39.9 ± 6.3	3.78	664.8	0.881
C2	26.3 ± 1.0	448.4 ± 103.2	1.41 ± 0.33	33.9 ± 4.8	4.68	483.7	0.973
C3	15.2 ± 0.7	488.5 ± 136.6	1.27 ± 0.31	38.8 ± 6.6	3.30	537.8	0.932
C4	28.9 ± 3.2	297.7 ± 114.6	0.84 ± 0.34	36.9 ± 3.9	2.74	333.9	0.946
C5	16.2 ± 6.2	580.4 ± 159.1	1.74 ± 0.34	34.8 ± 4.0	4.19	625.4	0.896
C6	32.2 ± 4.9	305.5 ± 135.7	0.95 ± 0.36	30.6 ± 4.3	2.37	335.4	0.963
C7	15.6 ± 1.2	281.9 ± 87.3	1.08 ± 0.27	27.9 ± 1.8	3.09	301.5	0.941
C8	14.6 ± 1.9	360.4 ± 88.7	1.11 ± 0.22	33.6 ± 2.7	3.71	387.7	0.905
T700S	6.8 ± 0.3	3342.1 ± 1342.1	1.52 ± 0.42	247.4 ± 13.9	3.59	3767.4	0.952

**From two parameter Weibull Distribution*

TABLE VII: PARAMETERS FROM SFFT AND CALCULATED IFSS

Sample	Weibull σ_f	Fiber Diameter	Avg. Fiber Frag. Length	L_{crit}	IFSS
	MPa	**µm**	**µm**	**µm**	**MPa**
C1	664.8	16.3	194.1	258.8	20.9
C2	483.7	26.3	285.6	380.8	16.7
C3	537.8	15.2	282.1	376.1	10.9
C4	333.9	28.9	445.8	594.4	8.1
C5	573.8	16.2	228.1	304.1	15.2
C6	335.4	32.2	472.3	629.8	8.6
C7	301.5	15.6	84.7	112.9	20.8
C8	387.7	14.6	91.0	121.3	23.3
T700S	3767.1	6.8	909.9	1213.2	10.5

TABLE VIII: TORAY REPORTED PROPERTIES FOR PAN CARBON FIBER

Fiber	Tensile Strength (MPa)	Tensile Modulus (GPa)	Strain (%)	Density (g/cm^3)
T300	3,530	230	1.5	1.76
T400	4,410	250	1.8	1.80
T700	4,900	230	2.1	1.80
T800	5,880	294	2.0	1.80
M40J	4,410	377	1.2	1.81
M50J	4,120	475	0.8	1.88

TABLE IX: WIDE ANGLE DIFFRACTION PROPERTIES OF PAN CARBON FIBERS

	002 Peak		100 Peak		Crystalline Parameters		
Fiber	FWHM (°)	d-spacing (Å)	FWHM (°)	d-spacing (Å)	L_c (Å)	L_a (Å)	Mis-orientation Angle
T300	4.65	3.55	4.54	2.10	17.5	37.8	36.2
T400	4.92	3.51	4.20	2.10	16.5	40.8	36.3
T700	4.49	3.50	4.25	2.10	18.2	40.2	37.5
T800	4.34	3.49	3.87	2.10	18.9	44.4	32.3
M40J	2.62	3.45	1.90	2.12	31.4	89.7	24.9
M50J	1.97	3.44	1.41	2.12	41.4	121.0	18.4

TABLE X: THE DETERMINED PORE SIZES FROM SAXS

Sample	Pore Diameter*	<L>	Bg
	nm	nm	rad
T300	1.7	4.2	1.2
T400	1.3	3.3	0.4
T700	1.2	3.8	0.4
T800	1.8	4.1	0.7
M40J	2.6	5.8	1.8
M50J	3.4	9.3	2.3
	*From Irena Software		

TABLE XI: UTM SINGLE FIBER MECHANICAL PROPERTIES OF CARBON FIBER SAMPLES

μ ± σ	Failure Strain	Failure Stress	SM (0)	dSM/dε
Sample	mm/mm	MPa	GPa	GPa
T300	0.013 ± 0.002	3018 ± 656	224 ± 11	5651
T400	0.016 ± 0.002	3932 ± 673	227 ± 14	5038
T700	0.015 ± 0.004	3518 ± 1117	219 ± 31	4440
T800	0.017 ± 0.002	5206 ± 930	284 ± 26	6686
M40J	0.012 ± 0.001	5096 ± 869	391 ± 27	10428
M50J	0.009 ± 0.001	4429 ± 696	472 ± 22	11607

FIGURES

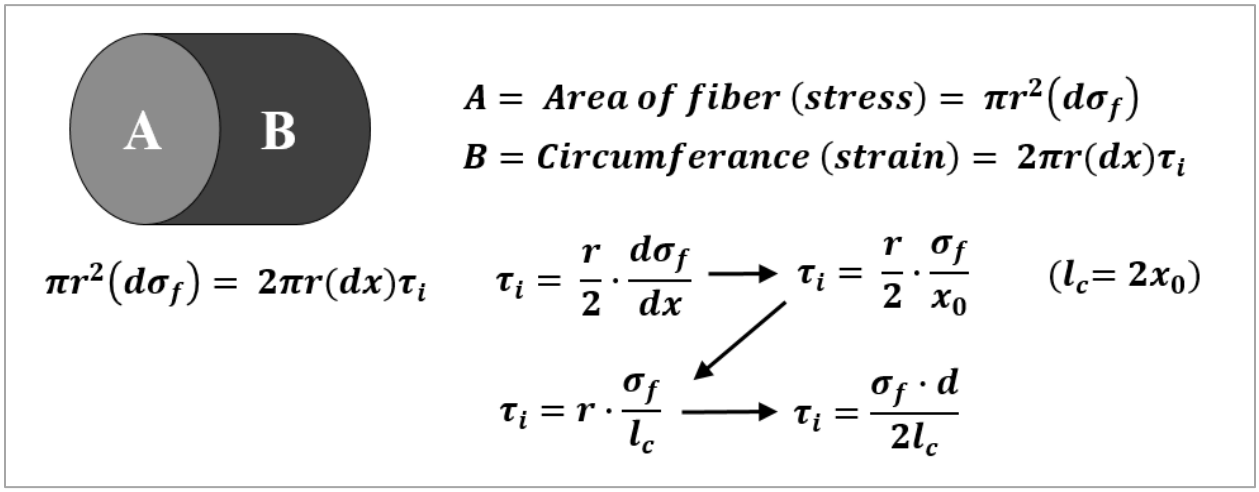

Figure 1: Diagram showing derivation of interfacial shear strength equation

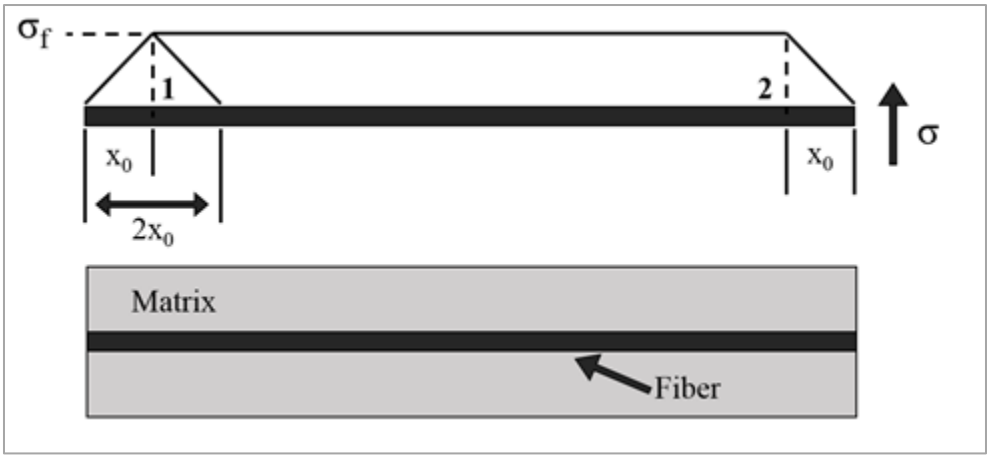

Figure 2: Schematic of stress along fiber and explanation of $2x_0$ and x_0.

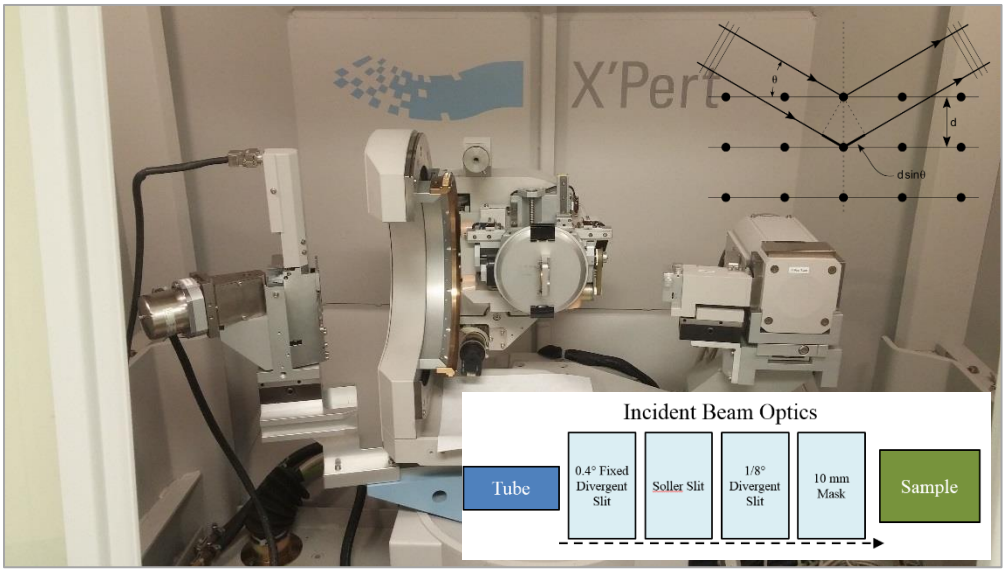

Figure 3: A PANalytical/Philips X'Pert Diffractometer with optics setup for carbon fiber analysis. In the upper right is a simple diagram demonstrating Bragg's Law and lower right shows the optics used for carbon fiber analysis.

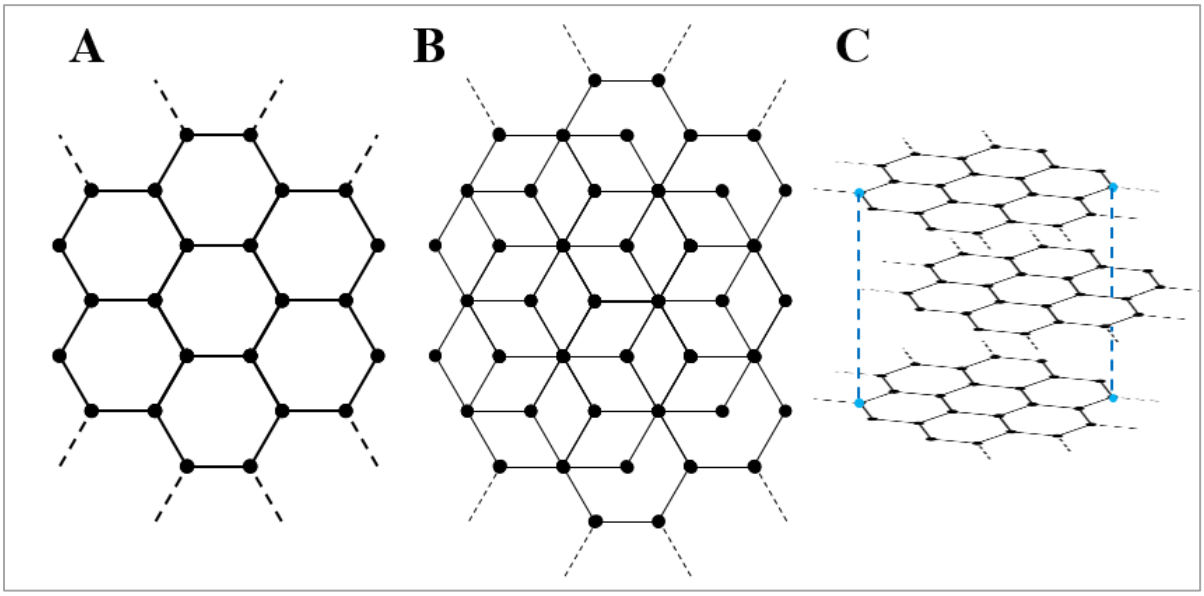

Figure 4: (A) A single plane of graphene, (B) planes of graphene stacked observed top down, and (C) a graphite crystal.

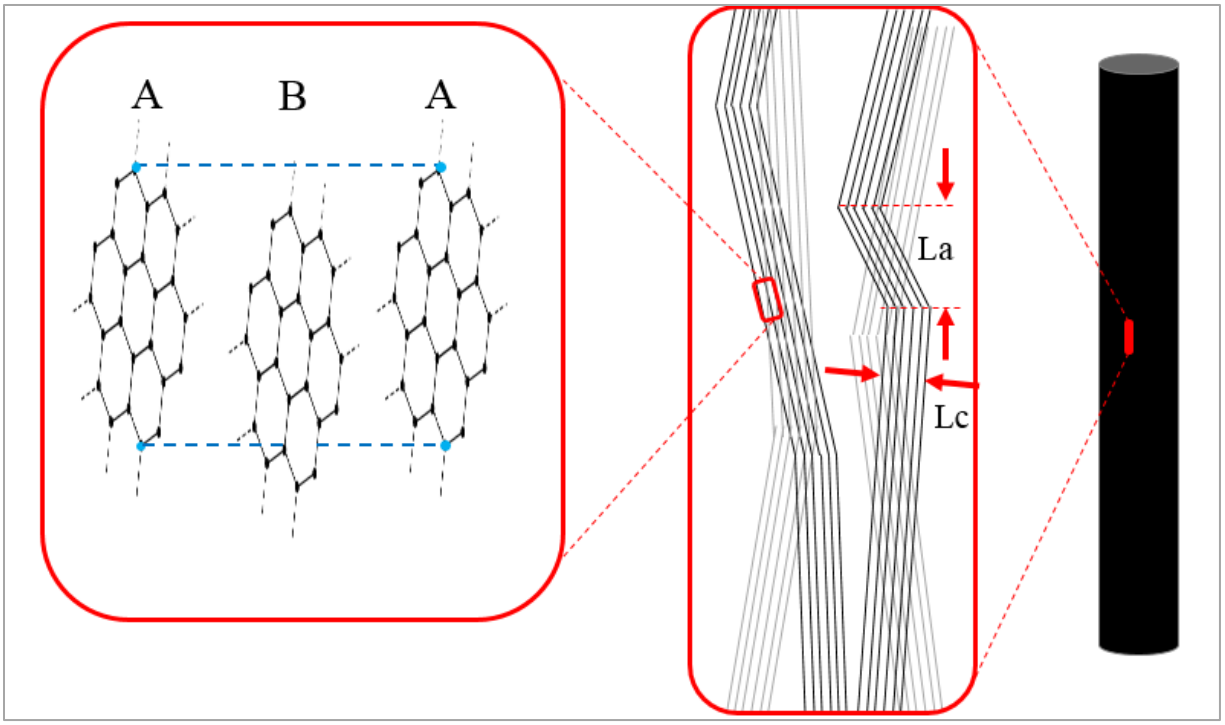

Figure 5: Schematic showing the graphene planes that make up elongated crystallites within a typical carbon fiber.

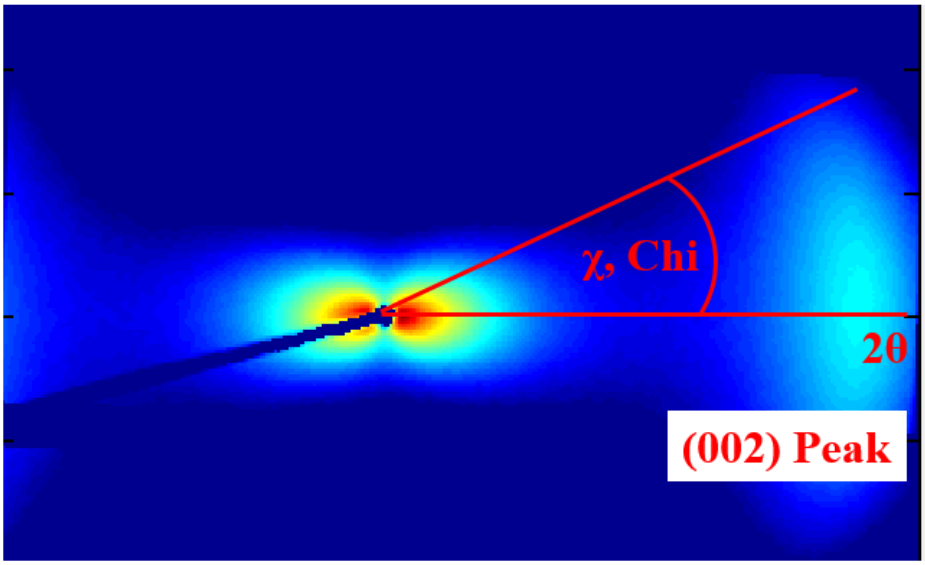

Figure 6: An example wide angle pinhole pattern for carbon fiber with the (002) peak indicated to demonstrate how it is quantified.

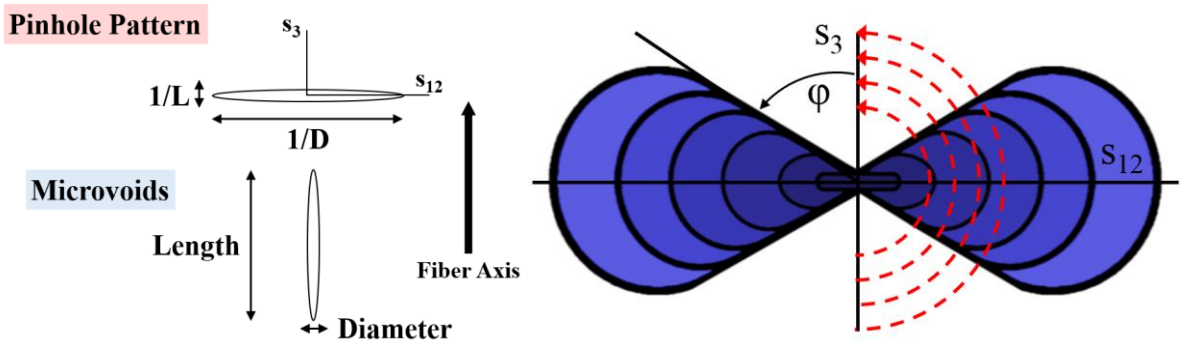

Figure 7: (A) Diagram demonstrating the correlation between projection on pinhole pattern and real scattering object (pore) and (b) streaking of pinhole pattern and fitting of intensity with either Gaussian or Lorentzian distributions (red dotted lines).

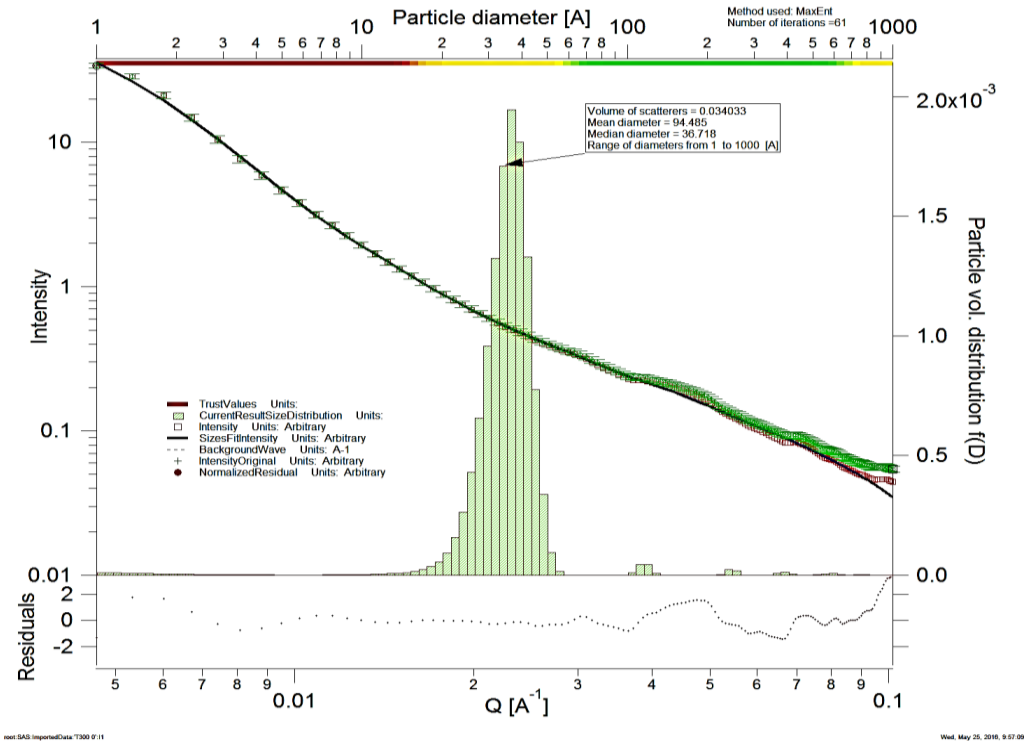

Figure 8: An example analysis of pore size for carbon fiber using the Irena – Igor software

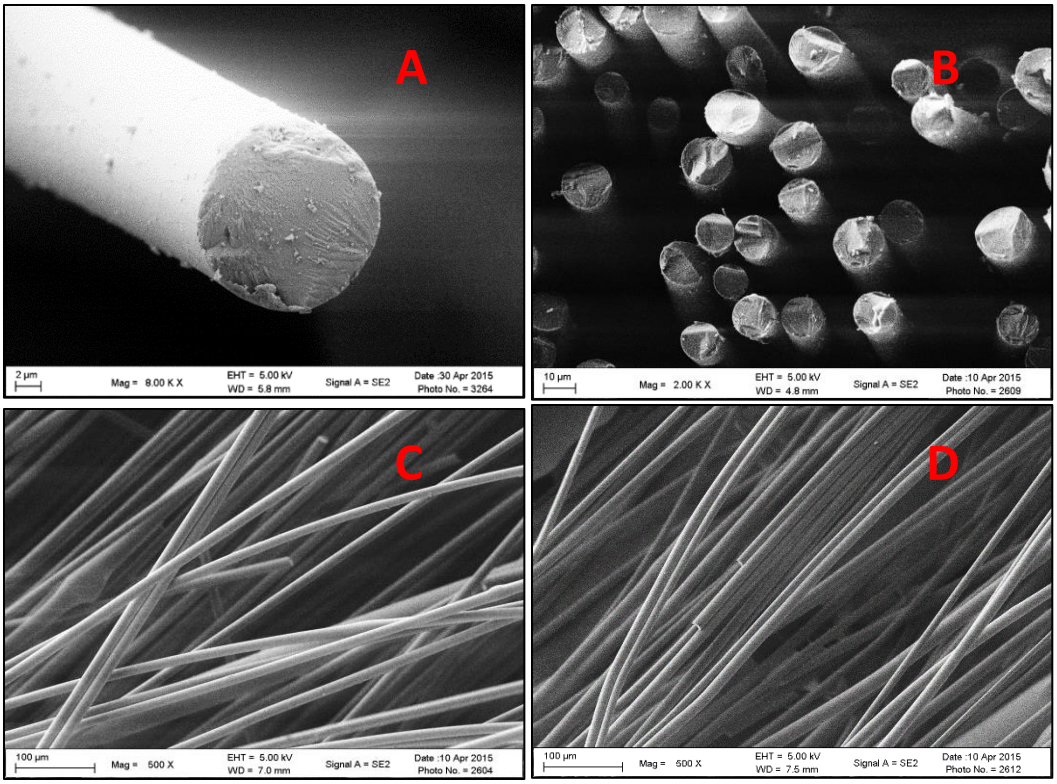

Figure 9: (A) A SEM micrograph of a single carbon fiber, (B) cluster of carbon fibers showing the cross-sectional area of the fibers and void content. (C) and (D) SEM micrographs showing the surface morphology where fibers showed minimal defects.

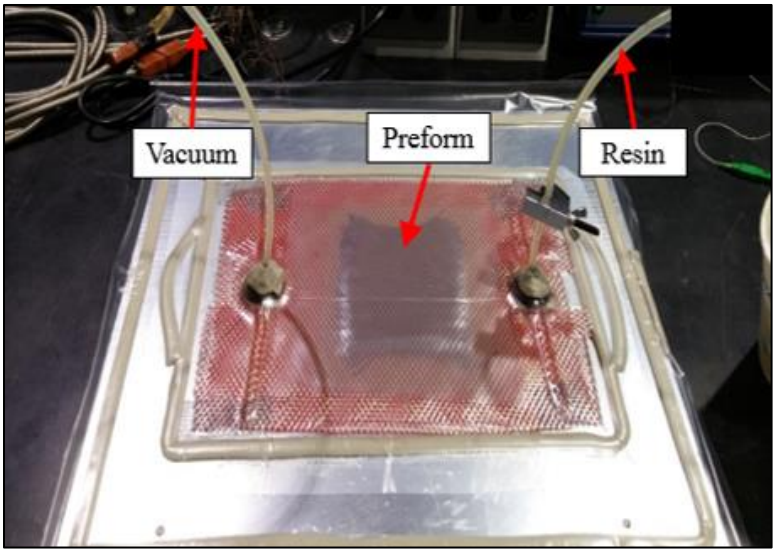

Figure 10: The experimental set-up for resin infusion. The carbon fiber and preform can easily be seen in the middle of the set-up.

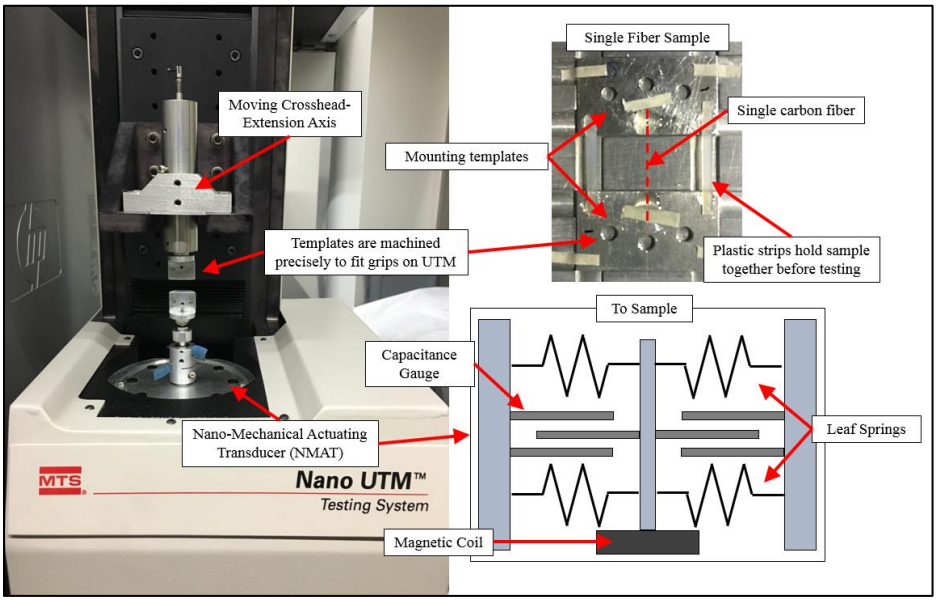

Figure 11: The MTS-UTM testing apparatus (left). Mounted sample and schematic of the NMAT (right)

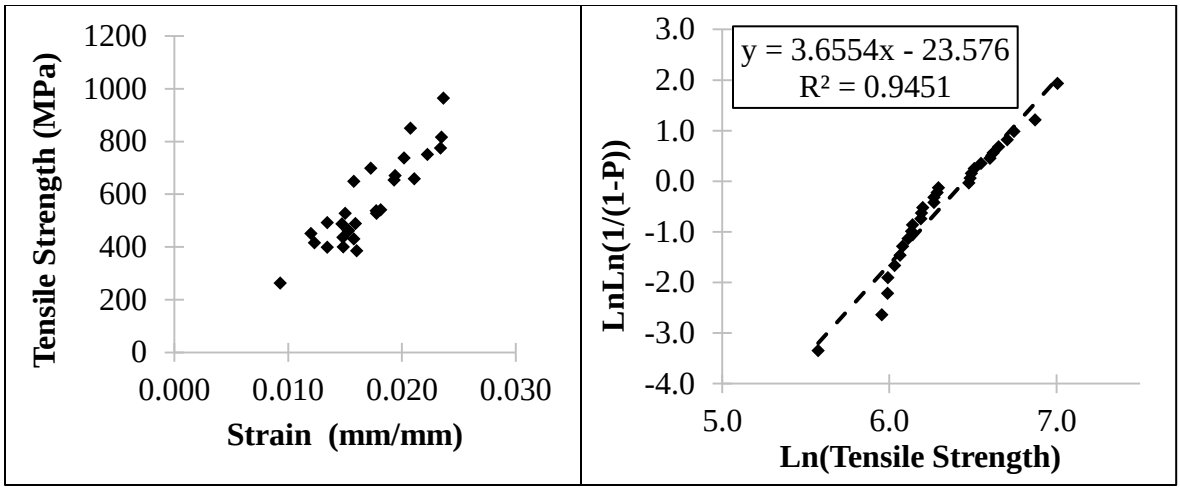

Figure 12: (A) Failure stress vs strain for single fiber samples. (B) The Weibull distribution for the mechanical results of single fibers. The Weibull parameters determined are a shape parameter of 3.66 and scale parameter for ~630 MPa.

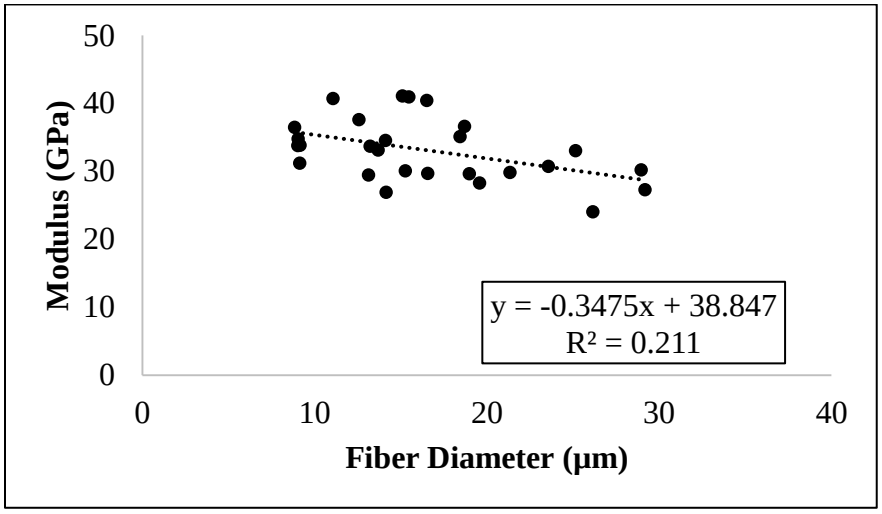

Figure 13: Modulus versus fiber diameter. A linear trend-line was fitted to the data. The trend shows as fiber diameter gets smaller, the modulus tends to increase.

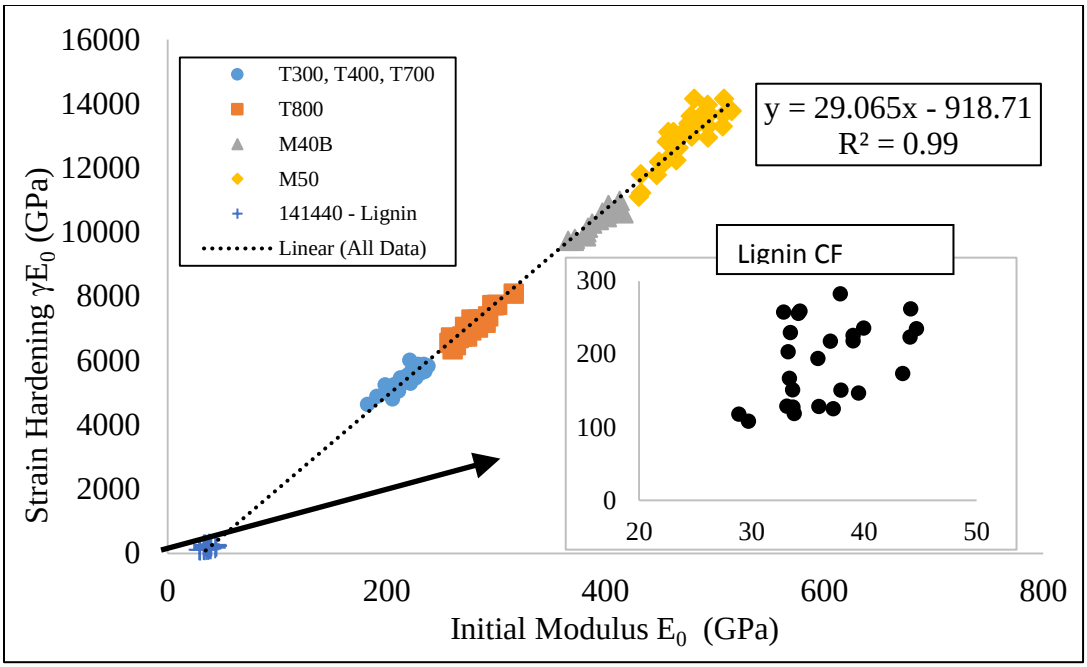

Figure 14: Strain Hardening (Stiffening) vs. Initial Modulus from Kant and Penumadu [11] with additional lignin carbon fiber data. Inset: lignin carbon fiber data.

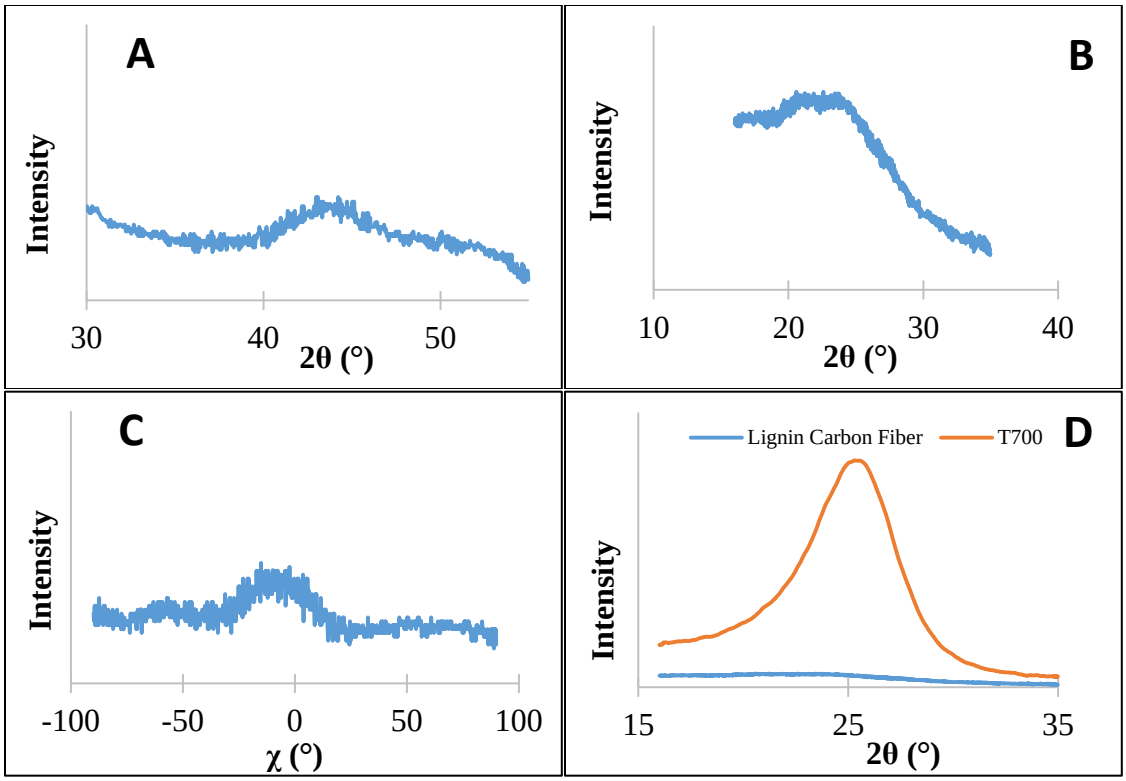

Figure 15: (A) Diffraction pattern for the 2θ scan from 30 to 55°. (B) Diffraction pattern for the 2θ scan from 16 to 35°. (C) Diffraction pattern for the χ scan from -90 to 90°. A small peak exists around 0° χ indicating some orientation of the fiber. (D) Diffraction patterns for the Lignin Carbon Fiber and T700.

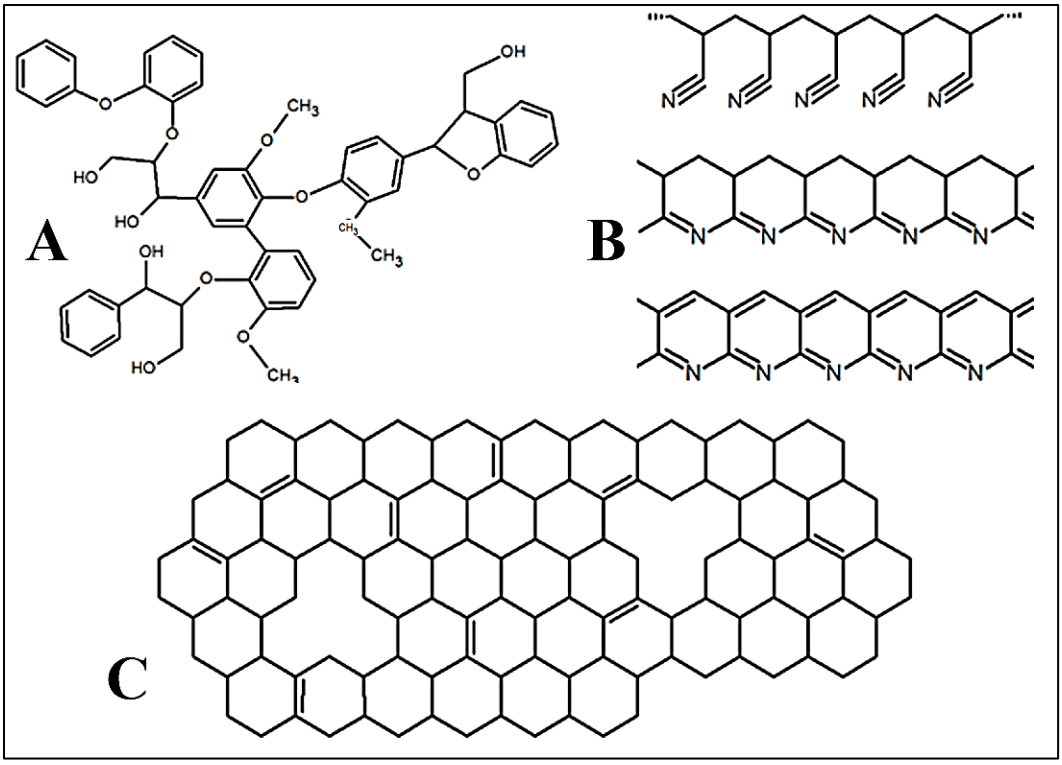

Figure 16: (A) A simplified lignin molecule, (B) a PAN molecule with steps showing cyclization and dehydrogenation, and (C) a simplified plane of a turbostratic graphitic crystallite.

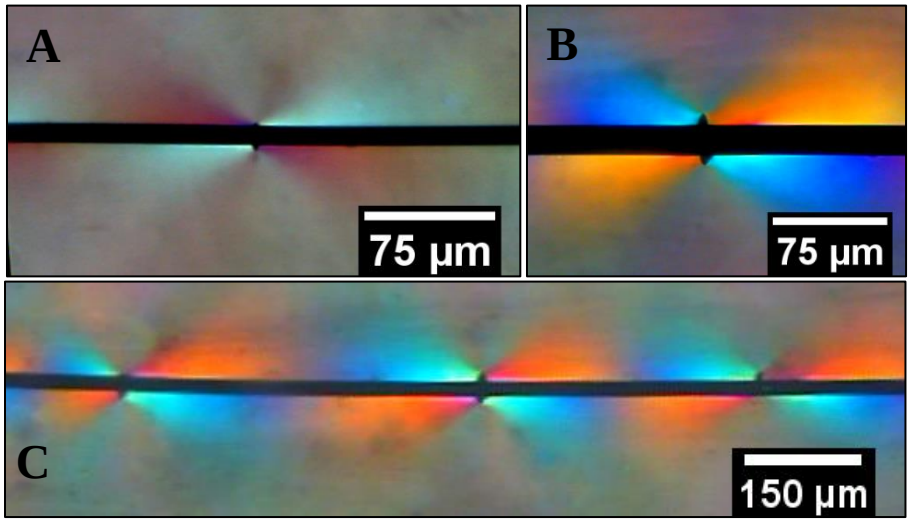

Figure 17: Two high magnification optical micrographs of fiber fractures (A, B) and a large section of a SFFT sample showing several breaks along the fiber (C). Both examples shown here demonstrate crack propagation into the matrix, stressed regions around the fiber break, and interfacial damage along fiber. The characteristic bowtie delamination zones can be seen around each break.

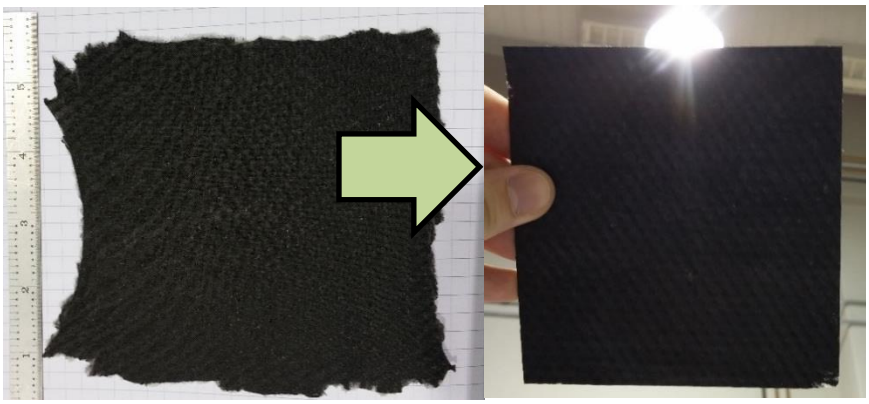

Figure 18: (A) The resulting 14 cm by 14 cm composite from the VARTM system reduced to (B) the 13 cm by 13 cm composite after trimming.

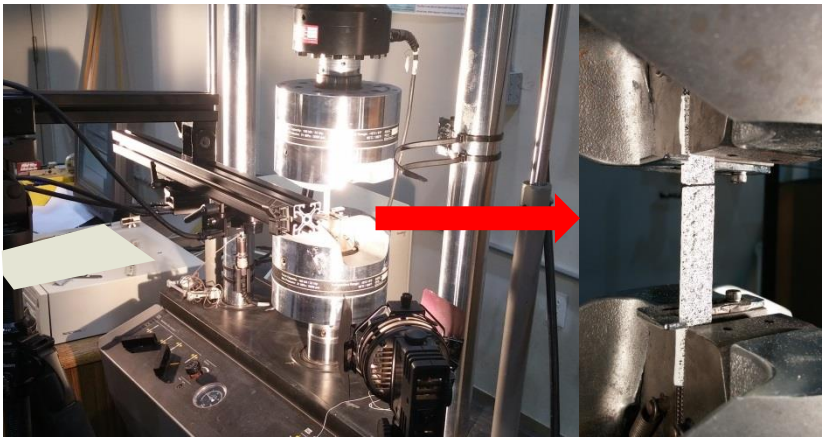

Figure 19: (left) Testing set-up for DIC and tensile testing of composite samples and (right) a failed composite specimen.

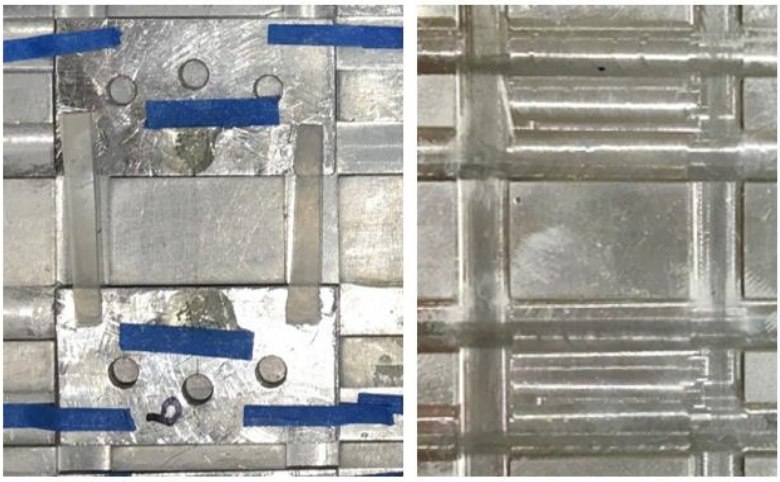

Figure 20: (left) A prepared sample for single fiber mechanical testing and (right) a blank machined block. The nylon strips that support the sample are easily visible in the prepared sample.

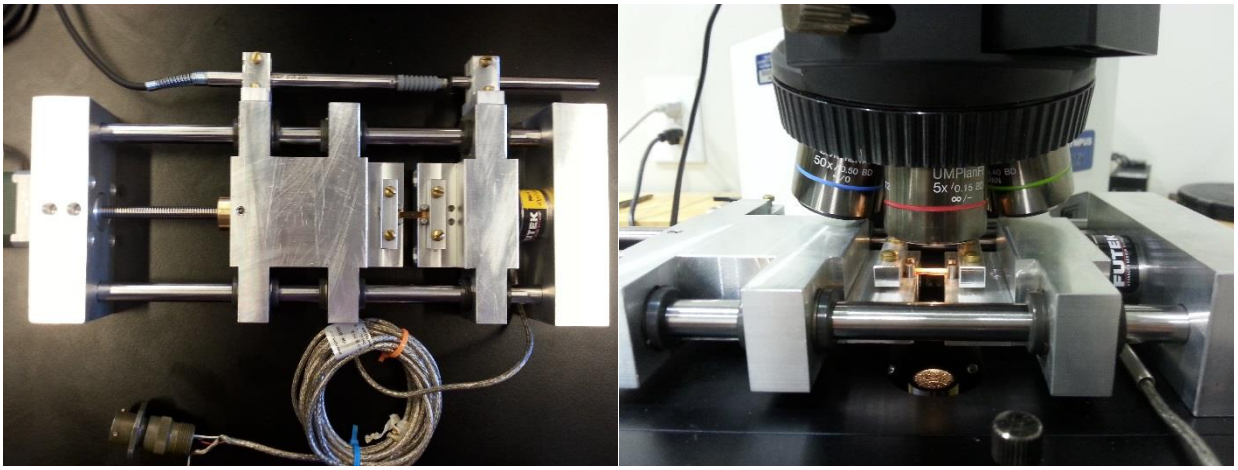

Figure 21: (left) The custom testing frame for SFFT and (right) in-situ image capture with transmission microscopy.

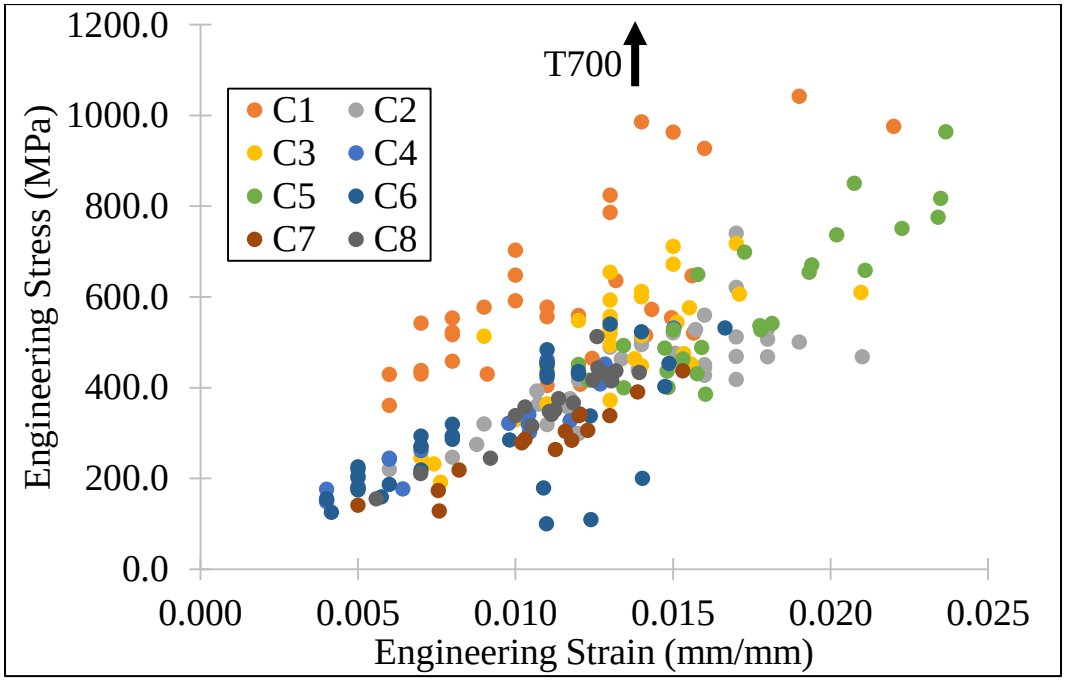

Figure 22: Stress vs. strain values for all lignin carbon fibers. T700S results are at approximately 3500 MPa tensile strength and therefore, are not presented here.

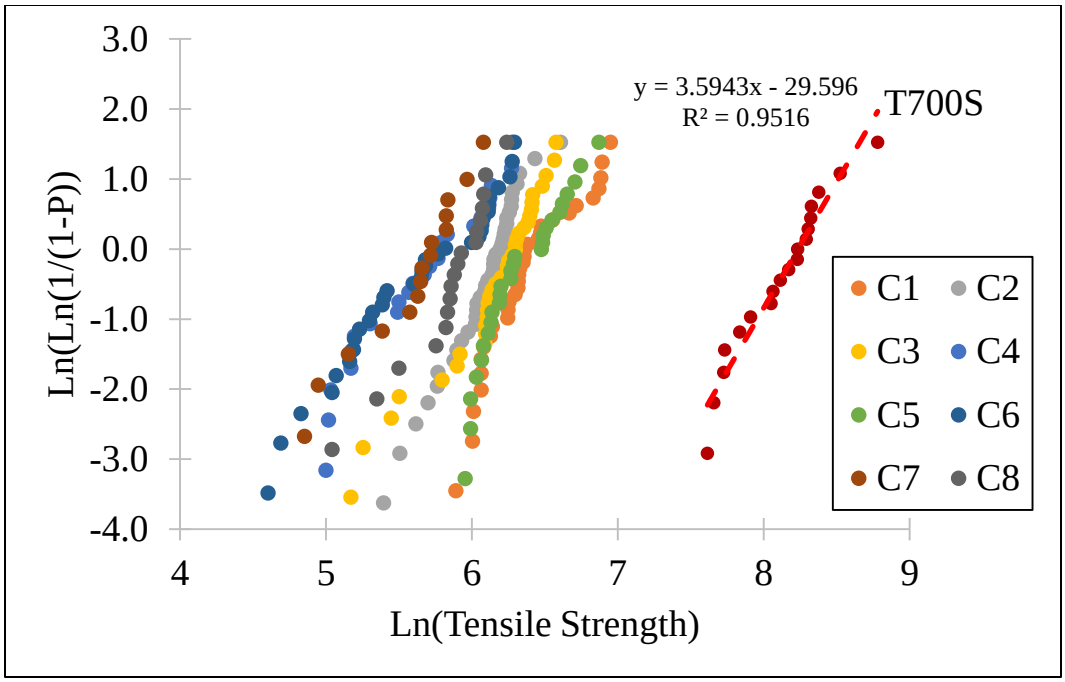

Figure 23: Weibull distributions for lignin carbon fiber samples and T700S control. An example of the determination of the shape and scale parameter is given for T700S (labeled separately).

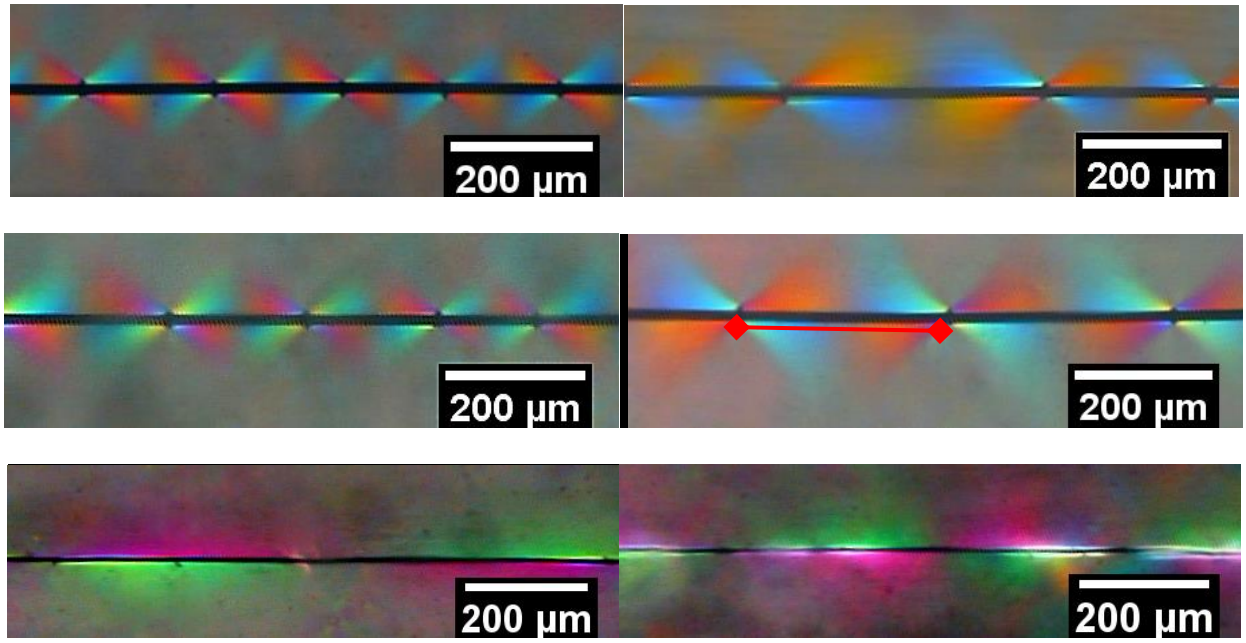

Figure 24: Four examples of Lignin SFFT samples (top) and two examples of T700S samples (bottom) showing fragmentations along the fiber and delamination zones. The red line in the middle right indicates the length of one fiber fragment.

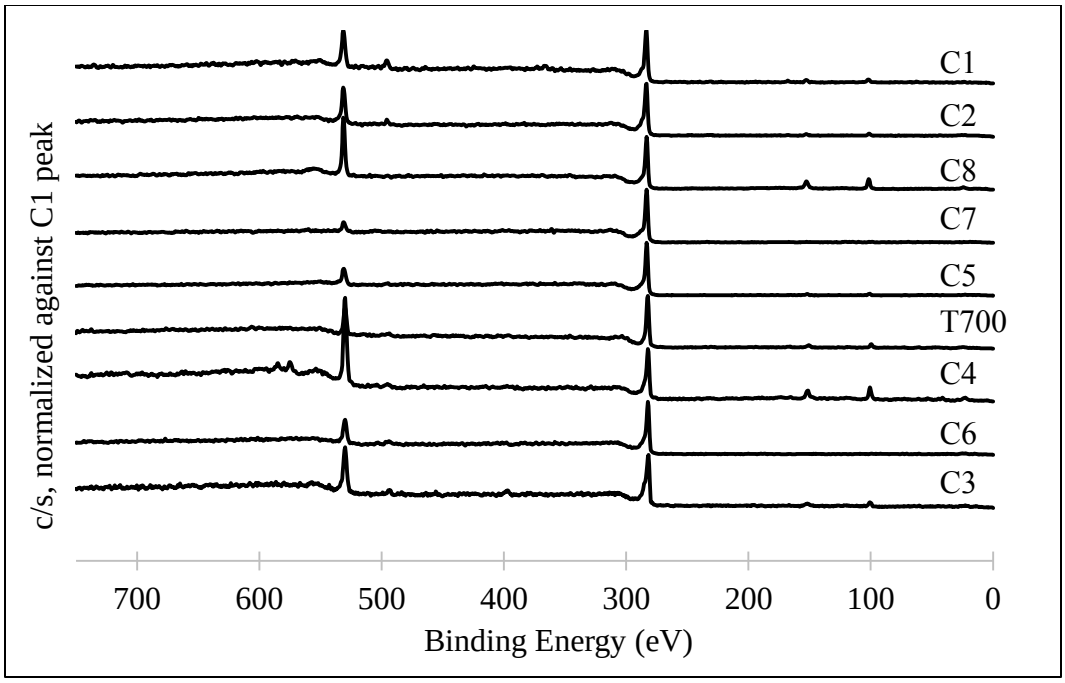

Figure 25: The XPS spectra for lignin carbon fiber samples. The C1 and O1 peak are roughly 284.4 and 531.0 eV.

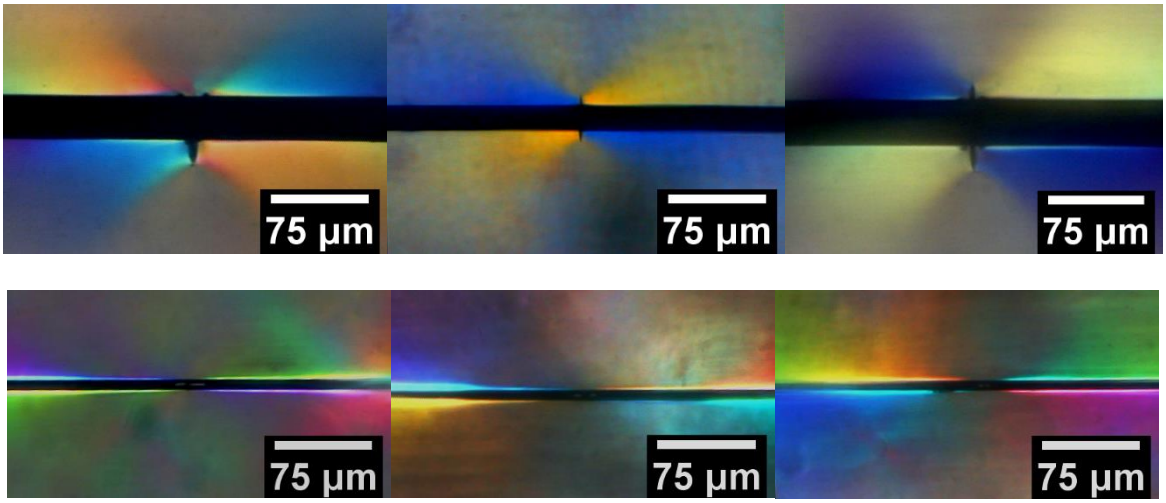

Figure 26: Three examples of lignin fiber fractures (top) and three examples of T700S fiber fractures (bottom).

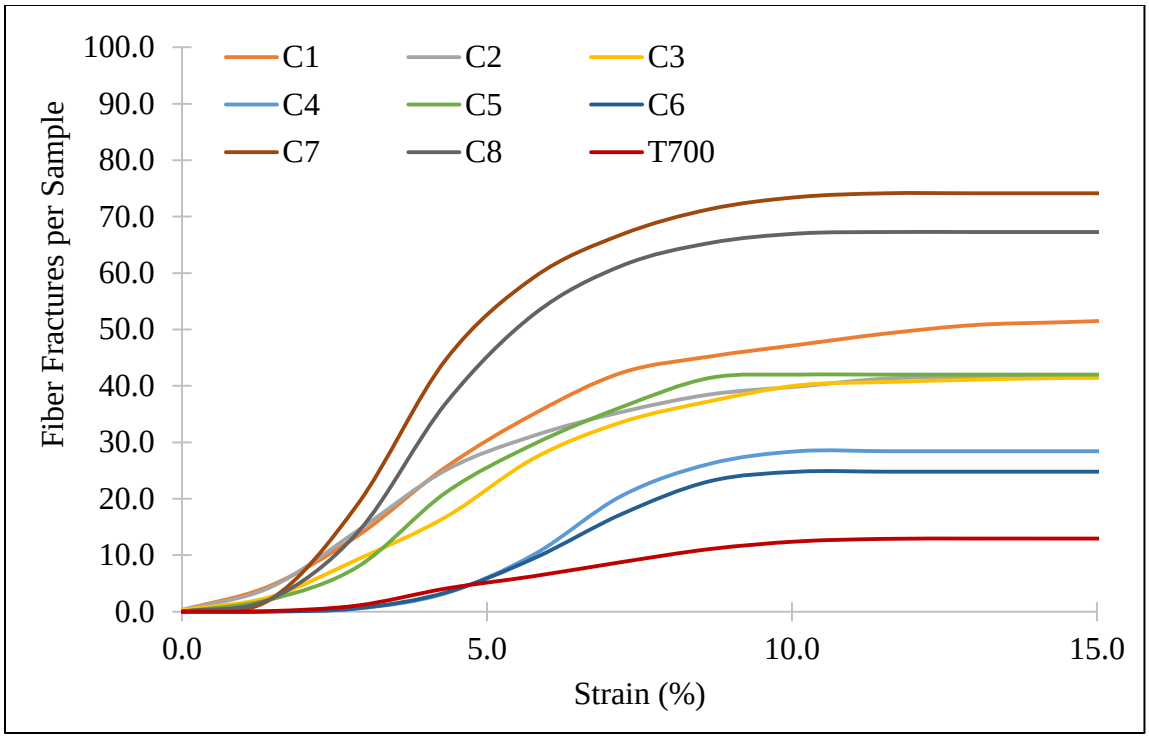

Figure 27: Fiber Fractures per sample vs. Strain Percentage for Single Fiber Fragmentation Testing.

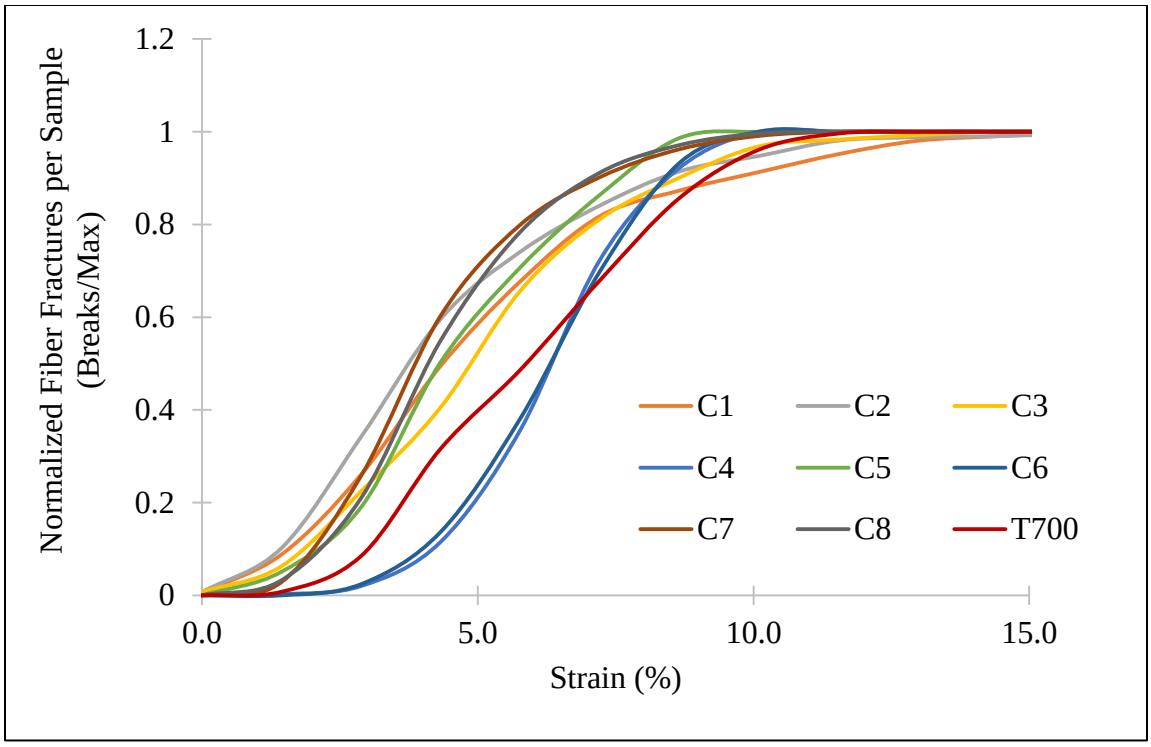

Figure 28: Normalized Fiber Fractures per Sample vs. Strain.

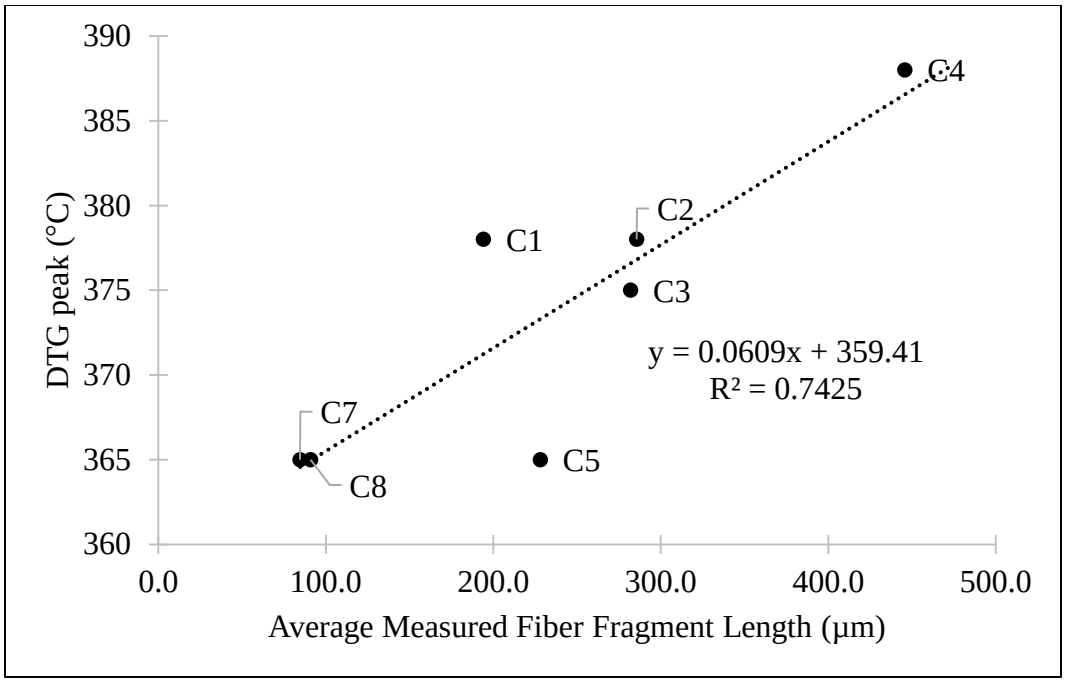

Figure 29: The Derivative TGA Peak value vs. Fiber Fragment Length

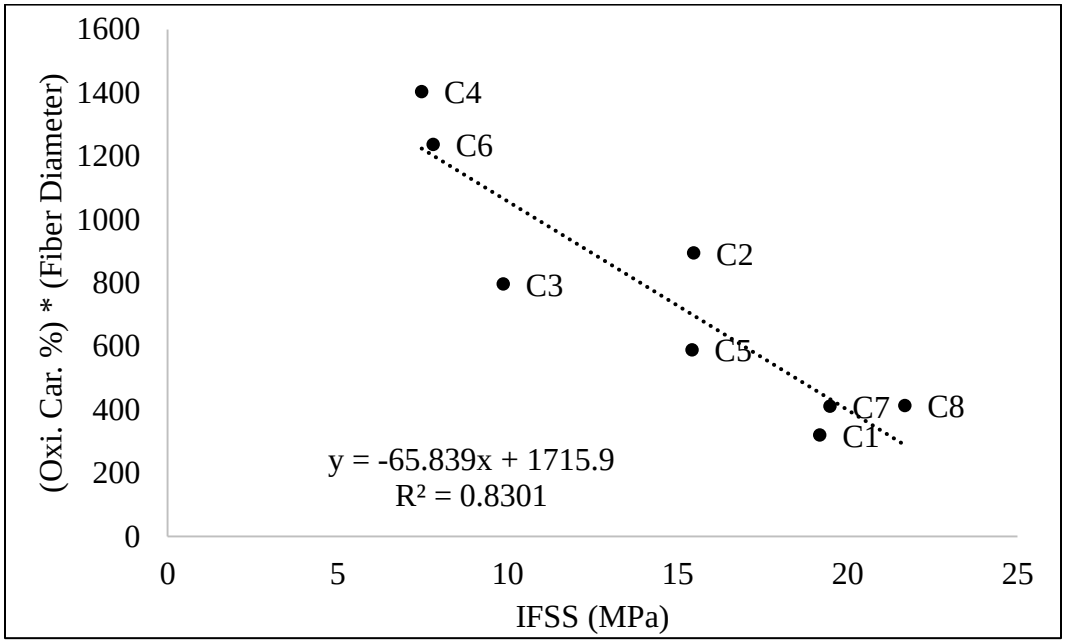

Figure 30: Oxidized Carbon times Fiber Diameter vs. IFSS for Lignin Carbon Fiber samples.

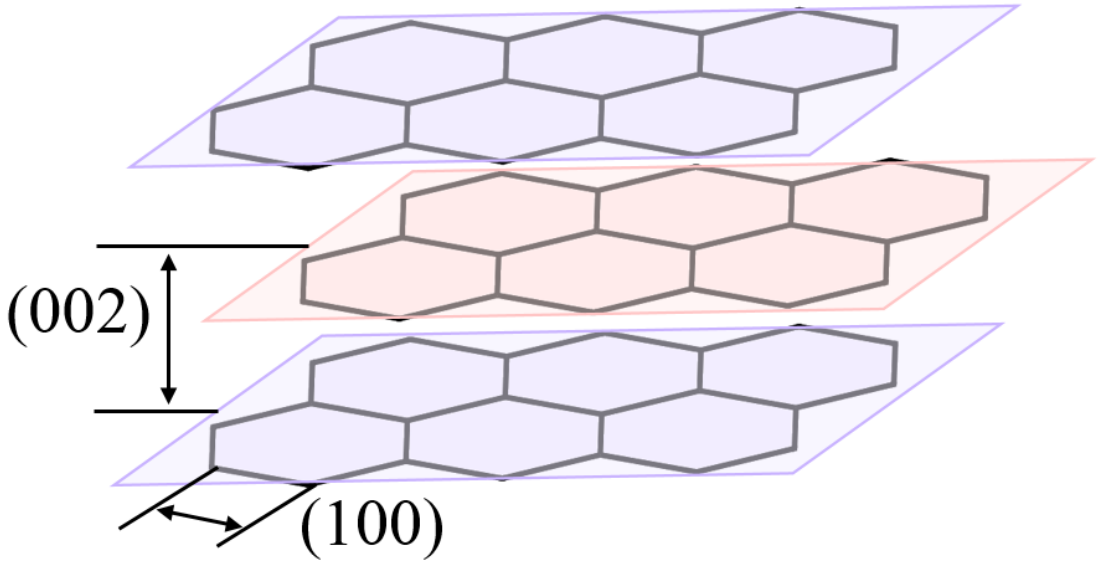

Figure 31: A simple graphitic lattice structure with (002) d-spacing and (100) d-spacing labeled. Planes are colored to help display AB stacking sequence of graphene.

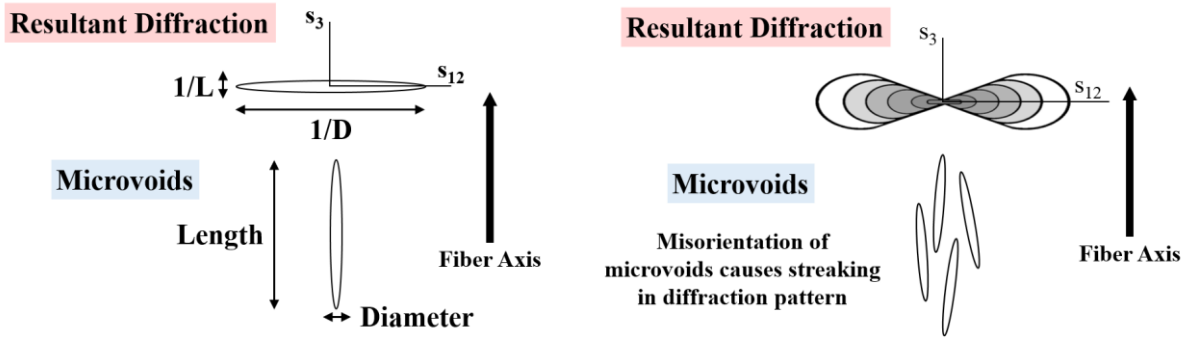

Figure 32: (Left) Diffraction pattern from a single ideal scatterer or microvoid and (right) the diffraction pattern for a typical carbon fiber sample.

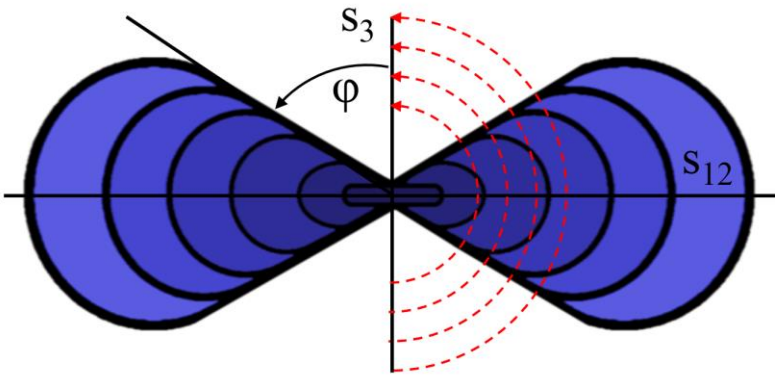

Figure 33: An example diffraction pattern typical of a carbon fiber sample. Red lines represent slices of q that are fitted with Gaussian or Lorentzian functions.

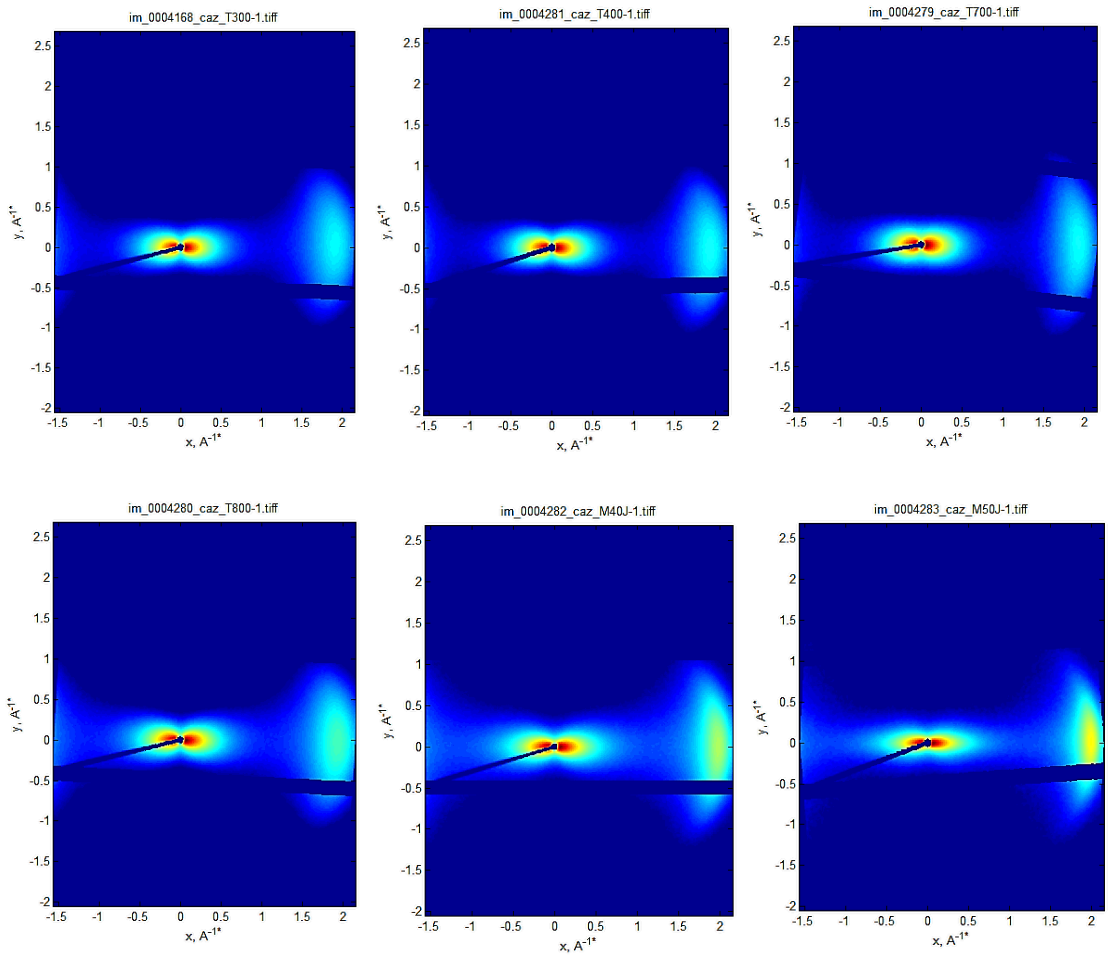

Figure 34: The wide-angle x-ray diffraction pinhole patterns for Toray PAN carbon fiber samples.

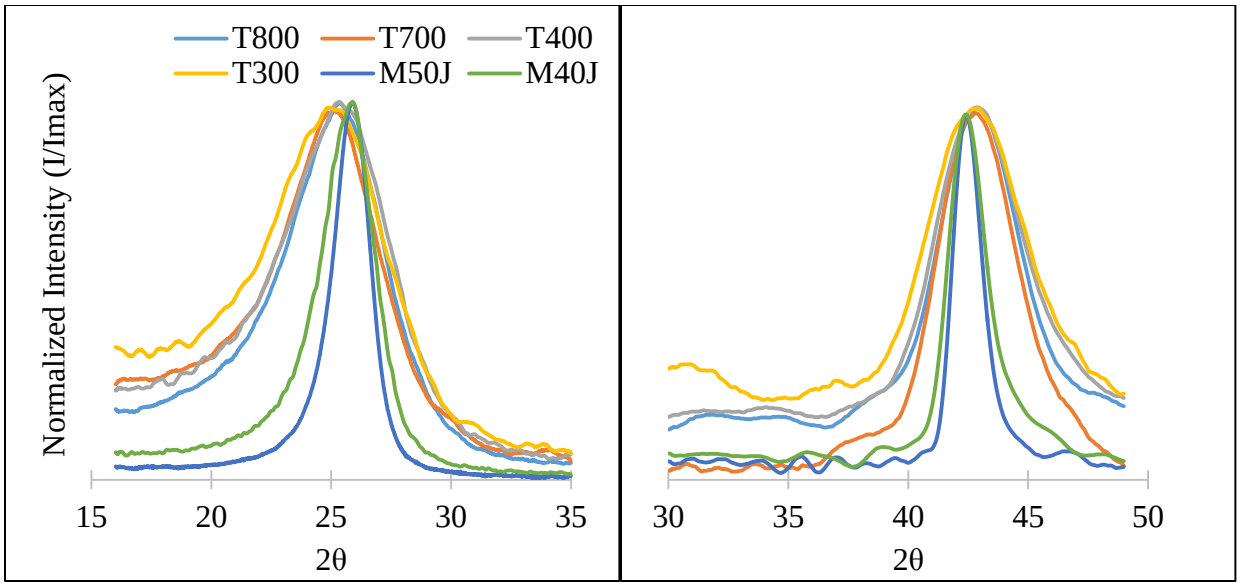

Figure 35: (002) reflection ad (100) reflection for Toray PAN carbon fiber samples from Philips XRD. It is important to note that the (100) is collected at χ=90°.

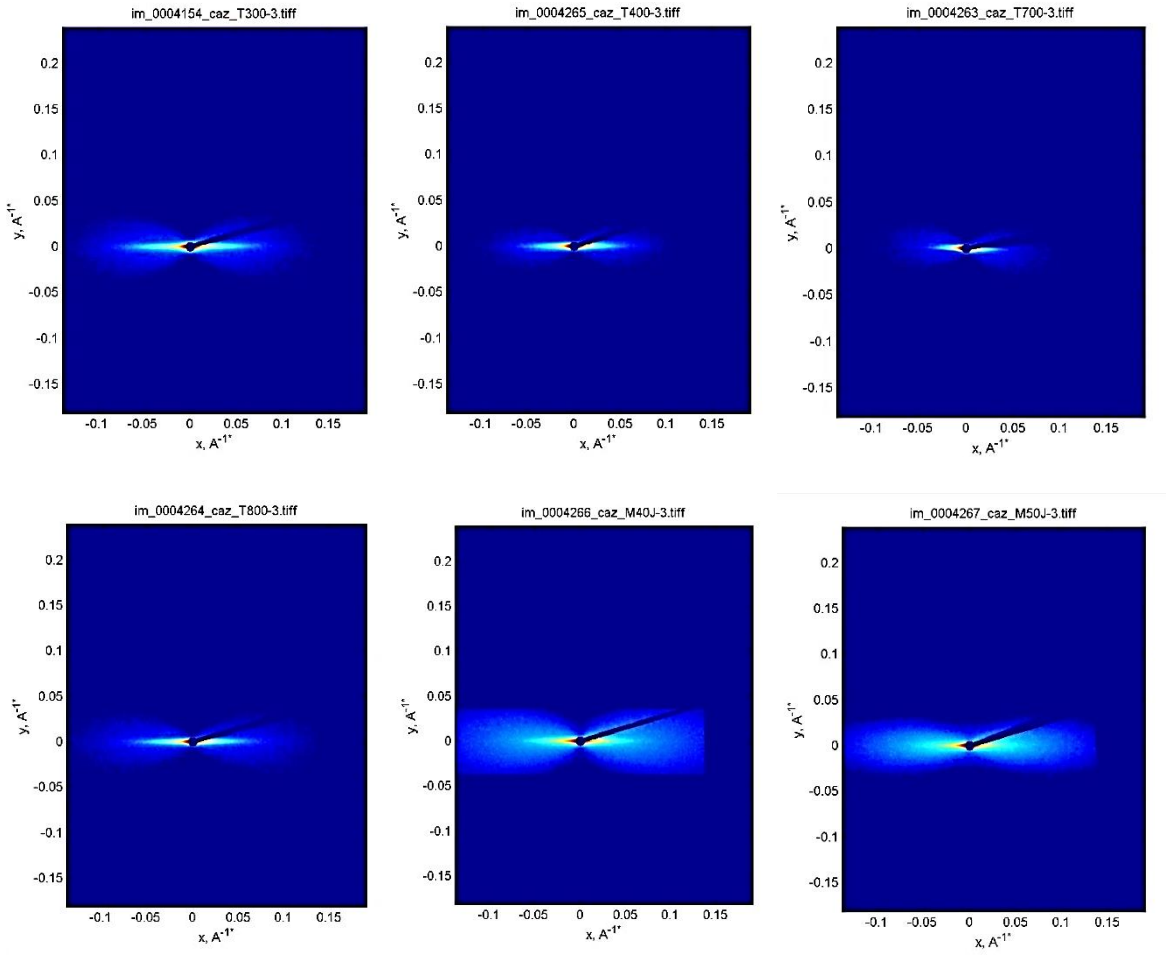

Figure 36: The small angle x-ray diffraction pinhole patterns for the Toray PAN carbon fiber samples.

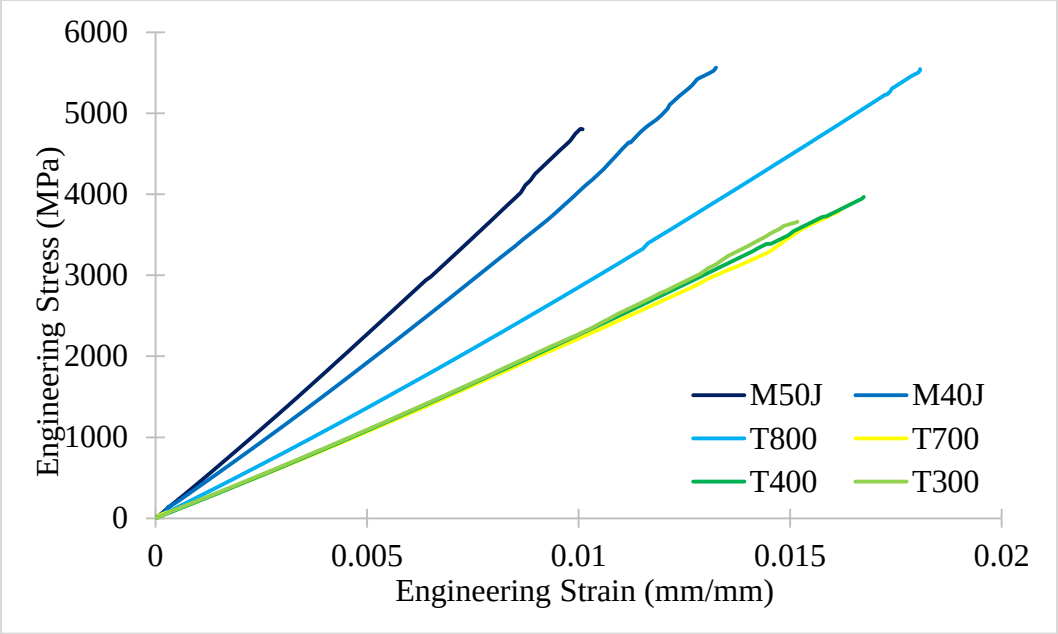

Figure 37: Stress versus Strain curves for PAN carbon fiber samples.

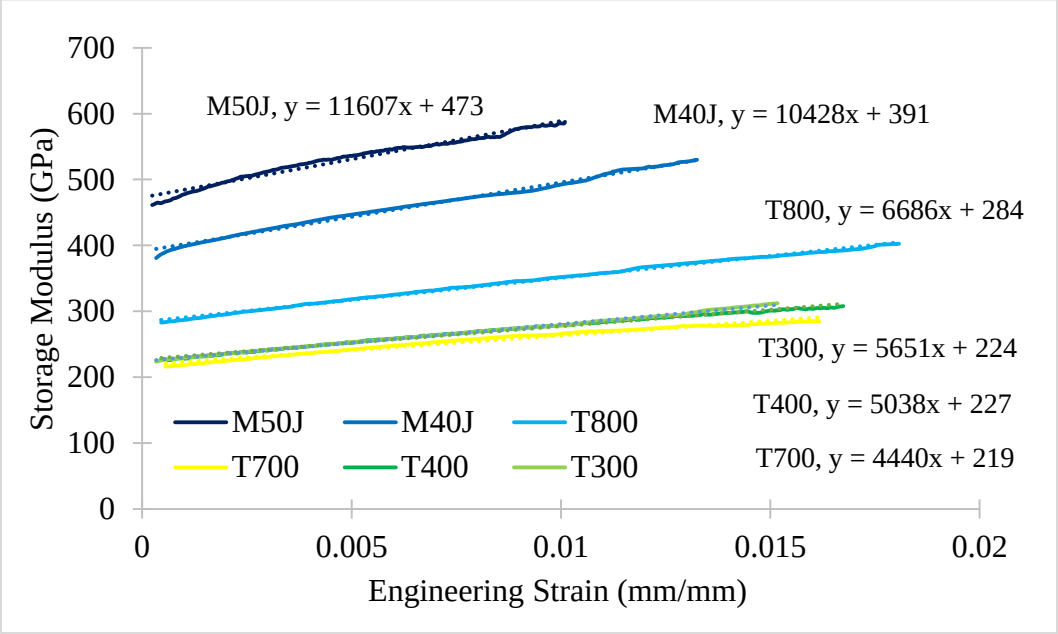

Figure 38: Average Storage Modulus versus Strain for PAN carbon fiber samples. Linear trends are labeled to display calculation of dSM/dε.

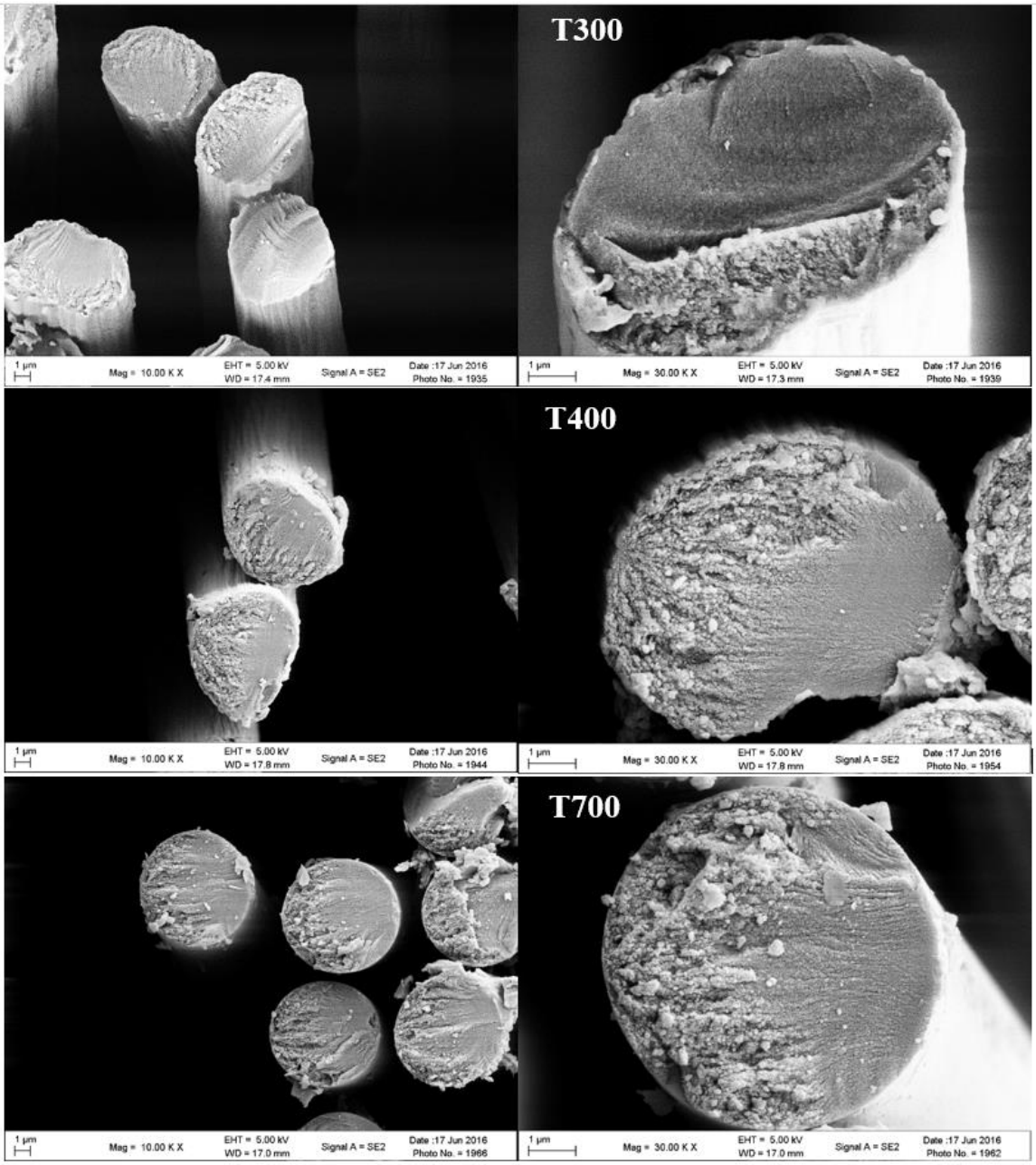

Figure 39: 10KX (left) and 30KX (right) SEM images for T300, T400, and T700.

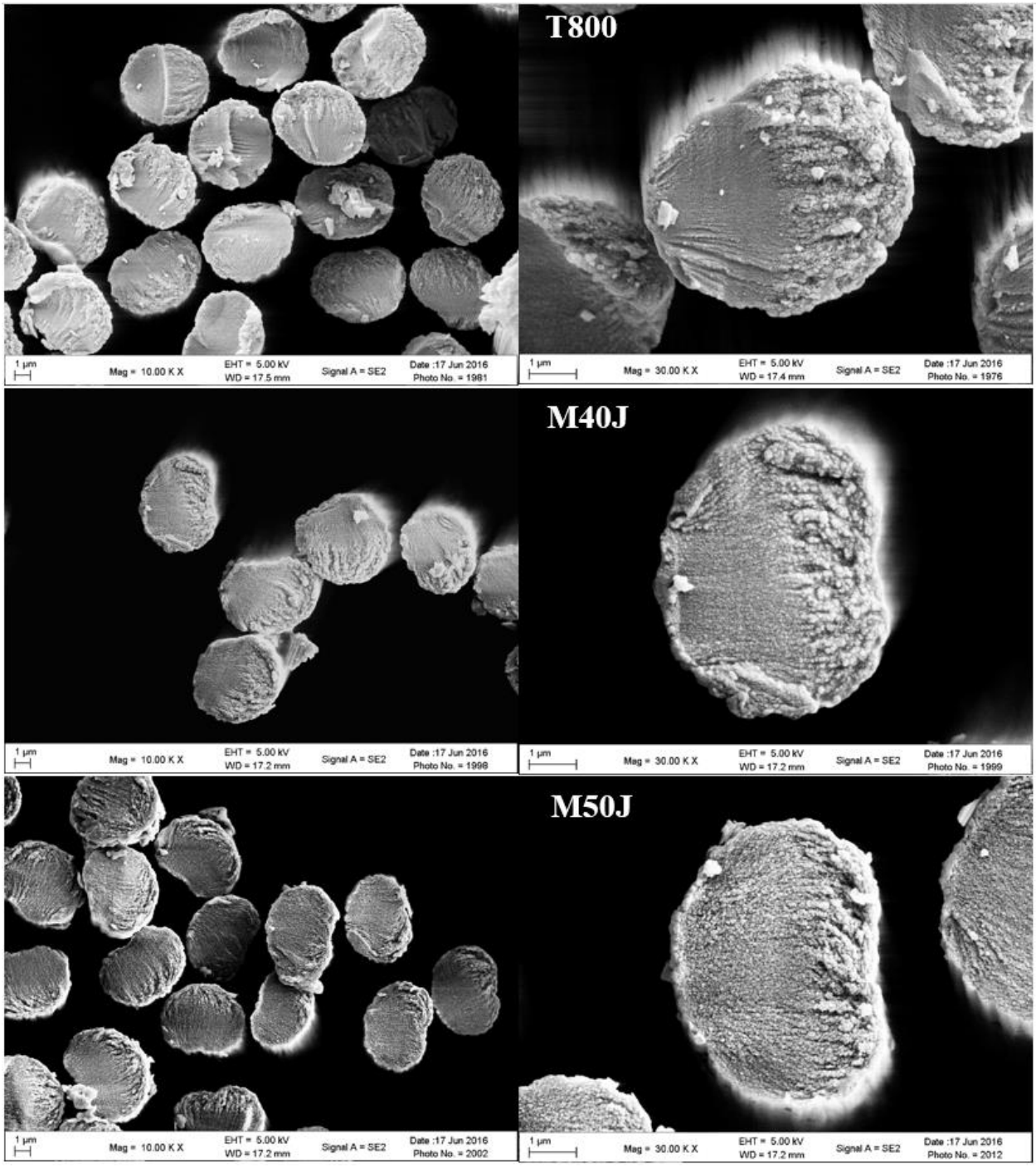

Figure 40: 10KX (left) and 30KX (right) SEM images for T800, M40J, and M50J.

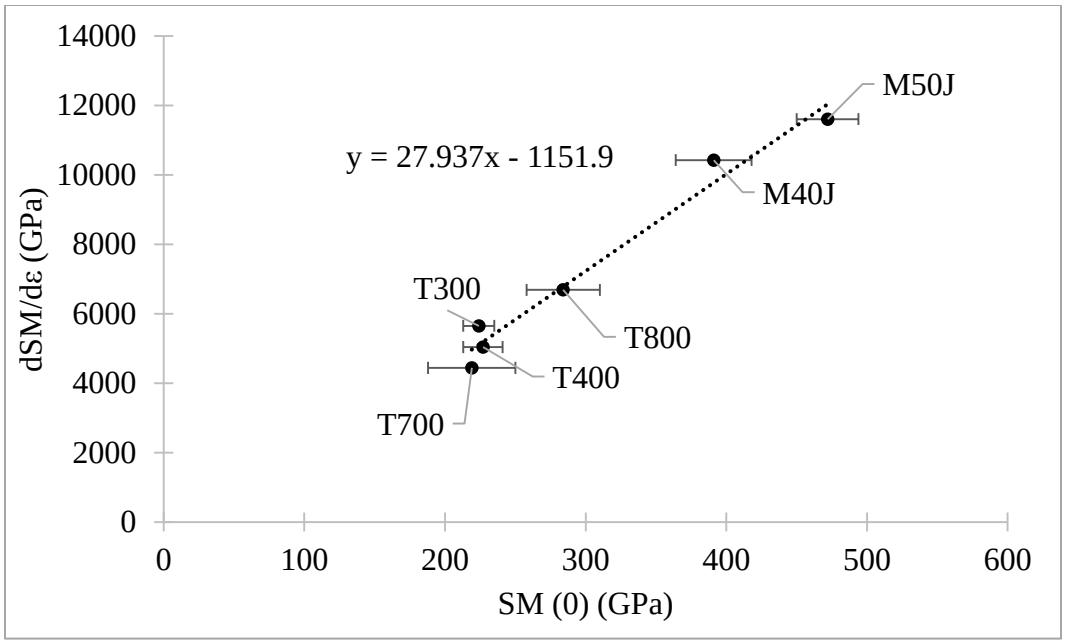

Figure 41: The determined dSM/dε versus initial storage modulus.

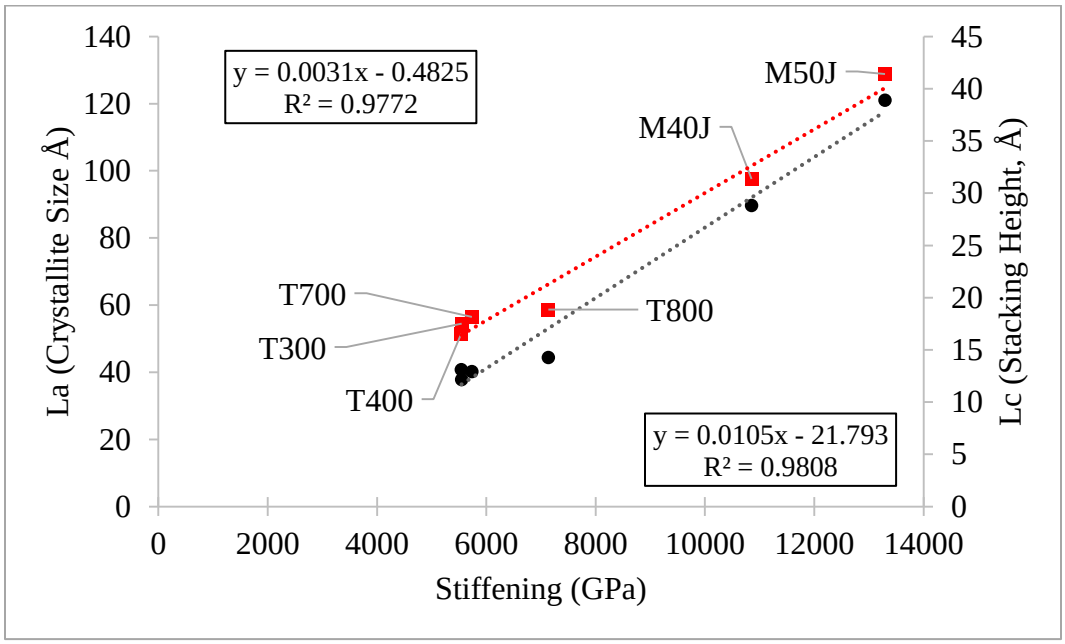

Figure 42: La (black circles) and Lc (red squares) versus Stiffening for PAN CF. The linear trend is listed for La in upper left and for Lc in the lower right.

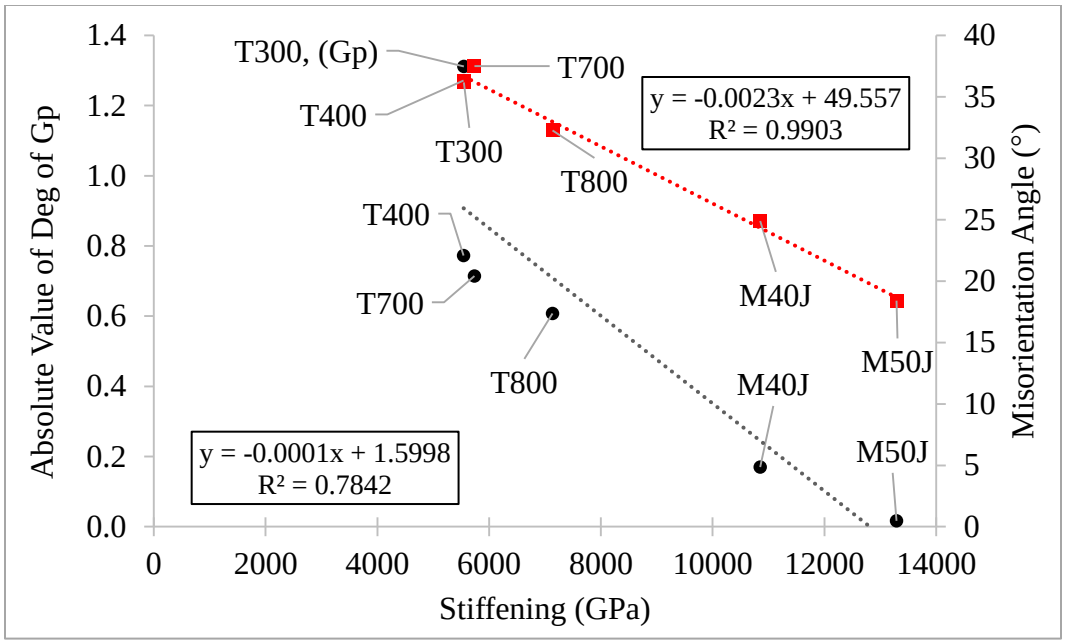

Figure 43: The Degree of Graphitization (black circles) and Misorientation Angle (red squares) versus Stiffening for PAN CF. The linear trend is listed for Deg. of Gp. in the lower left and for Misorientation Angle in upper right.

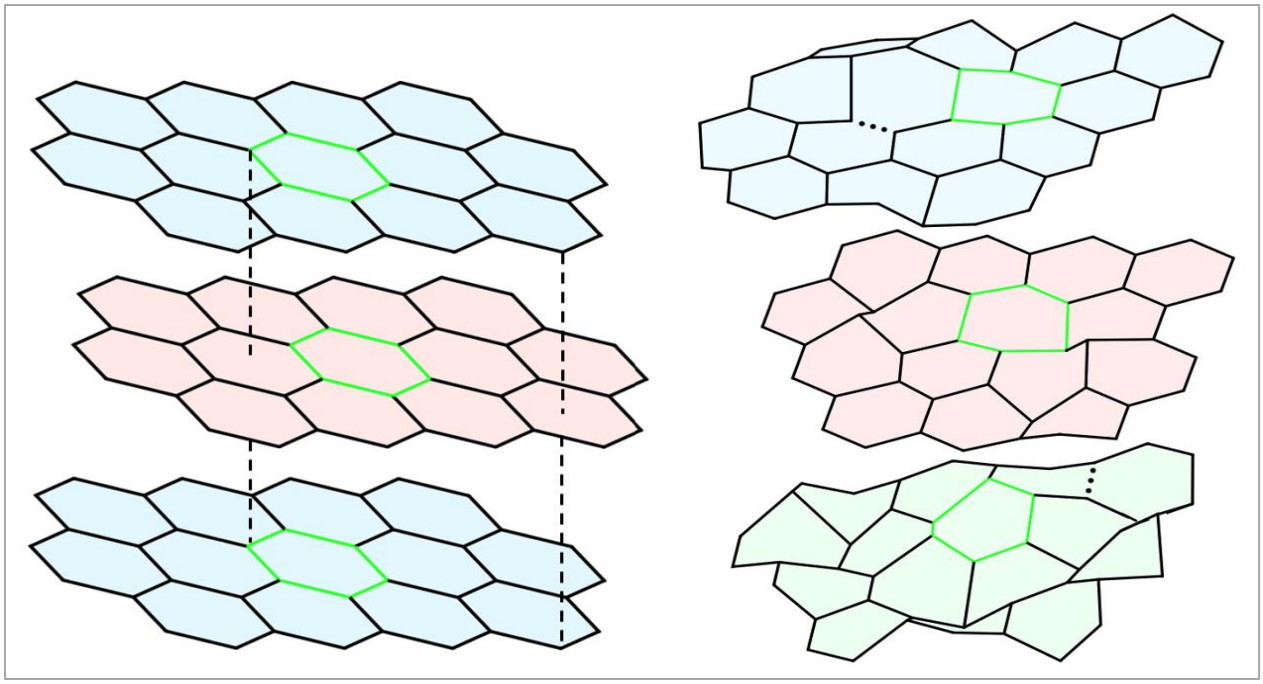

Figure 44: The basic lattice structure for graphite (left) and turbostratic carbon (right). Planes are colored to show stacking sequence. Graphite easily forms an AB sequence whereas turbostratic carbon does not always follow an AB sequence.

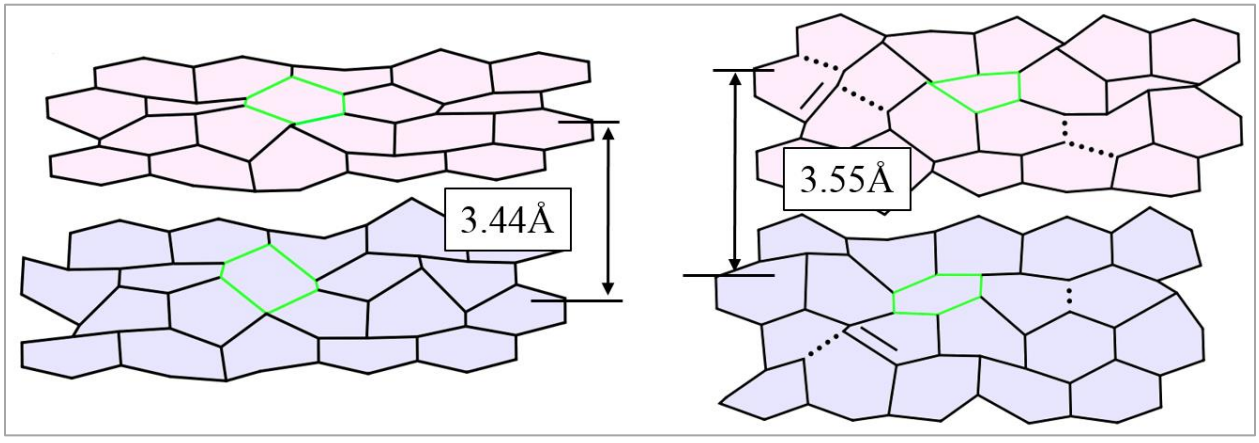

Figure 45: Diagram showing that as crystalline regions expand, the crystalline structure becomes more perfect and therefore d-spacings become smaller.

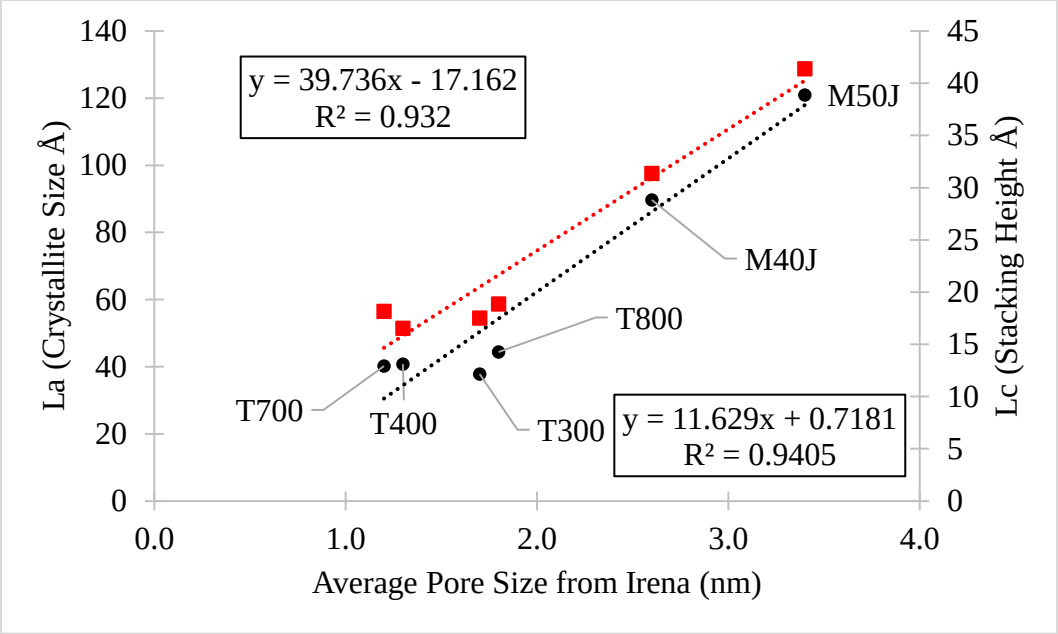

Figure 46: La (black circles) and Lc (red squares) versus Pore Size from Irena for PAN CF. The linear trend is listed for La in upper left and for Lc in the lower right.

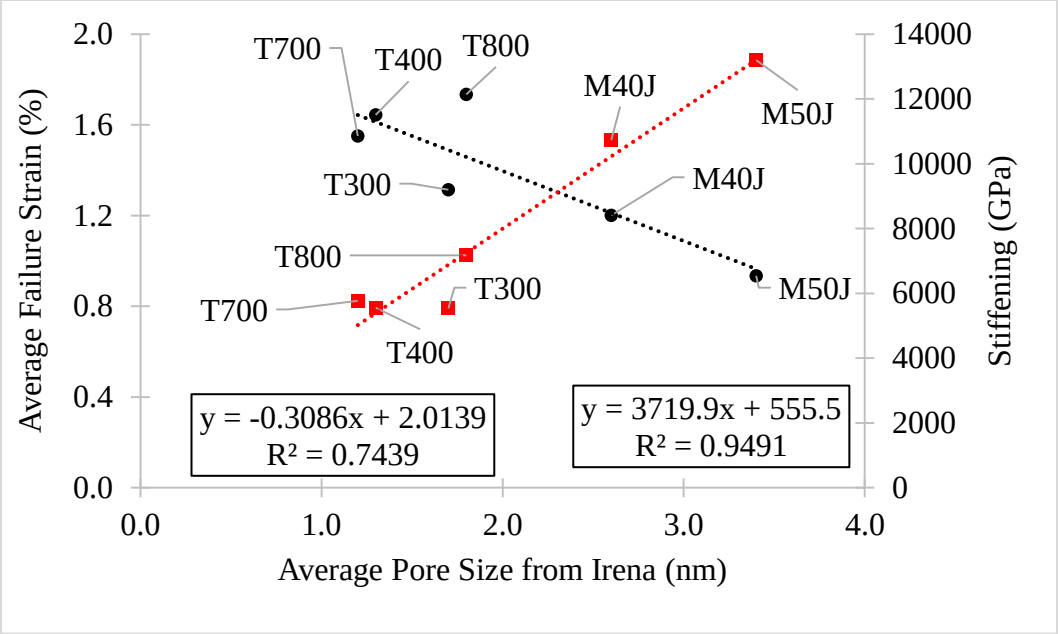

Figure 47: Average Failure Strain (black circles) and Stiffening (red squares) Pore Size from Irena. The trend is listed for Average Failure Strain in lower left and for Stiffening in the lower right.

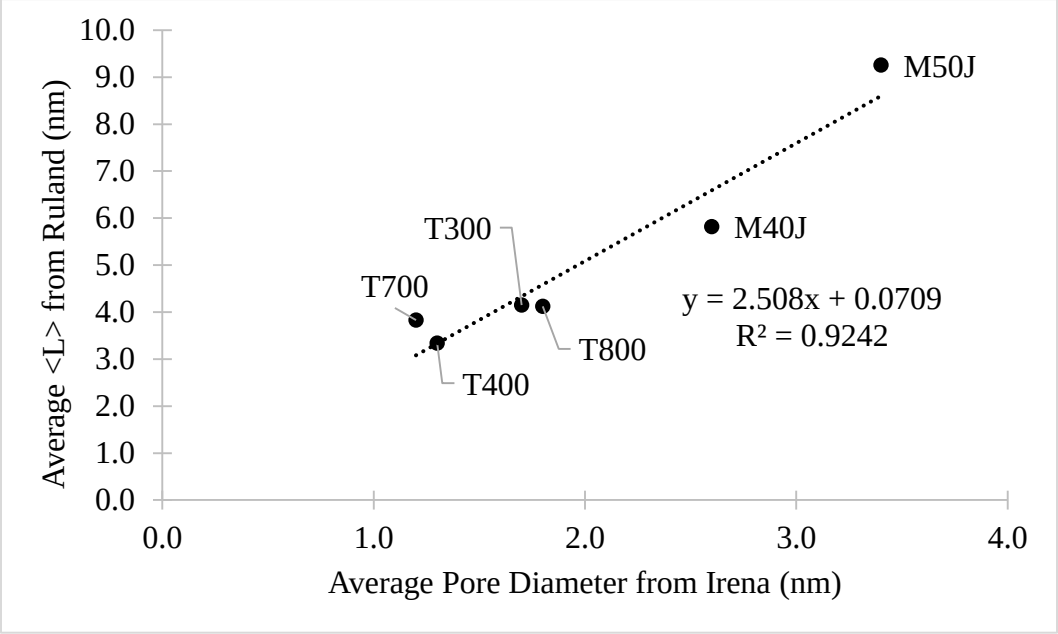

Figure 48: Average Pore Length from RSA versus Pore Diameter from Irena

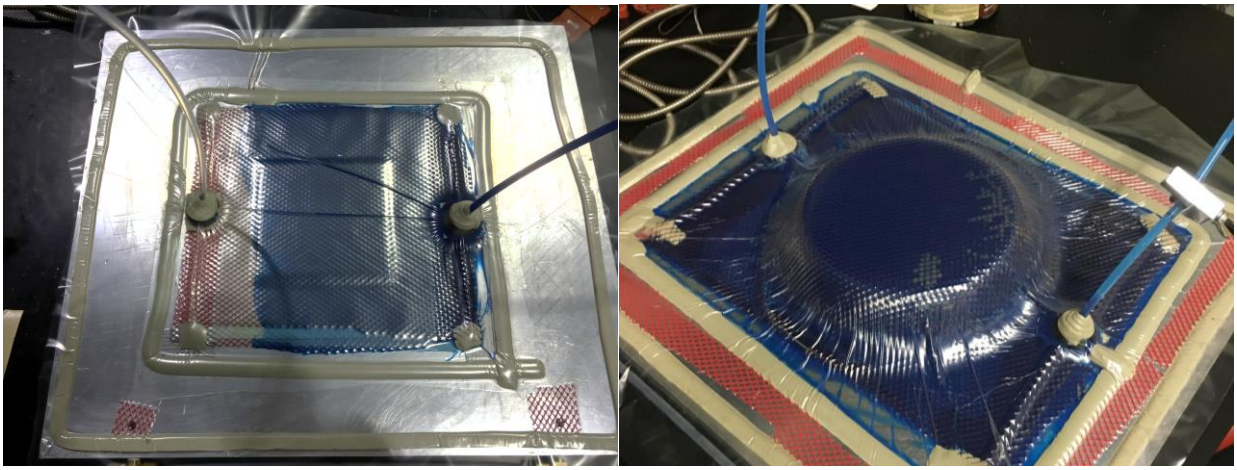

Figure 49: The VARTM system showing (A) a square panel and (B) part with complex geometry.

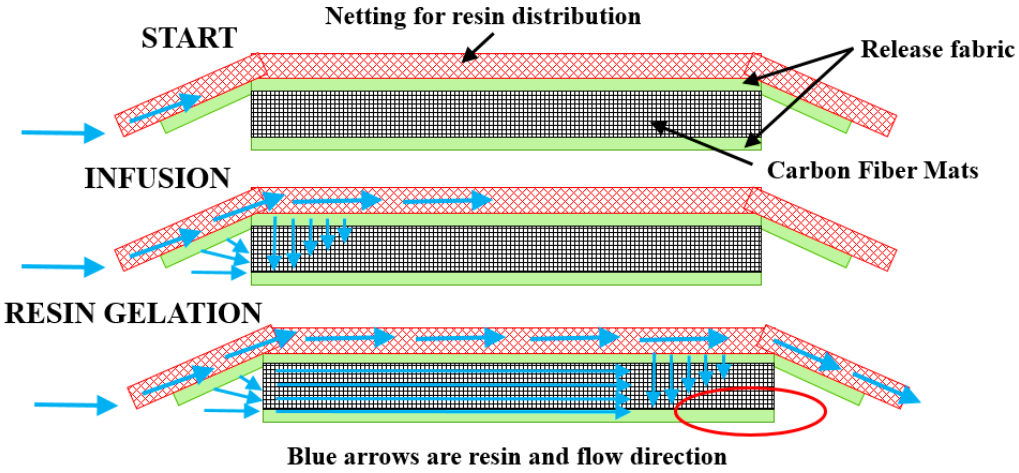

Figure 50: Diagram demonstrating infusion issues using a single resin flow media.

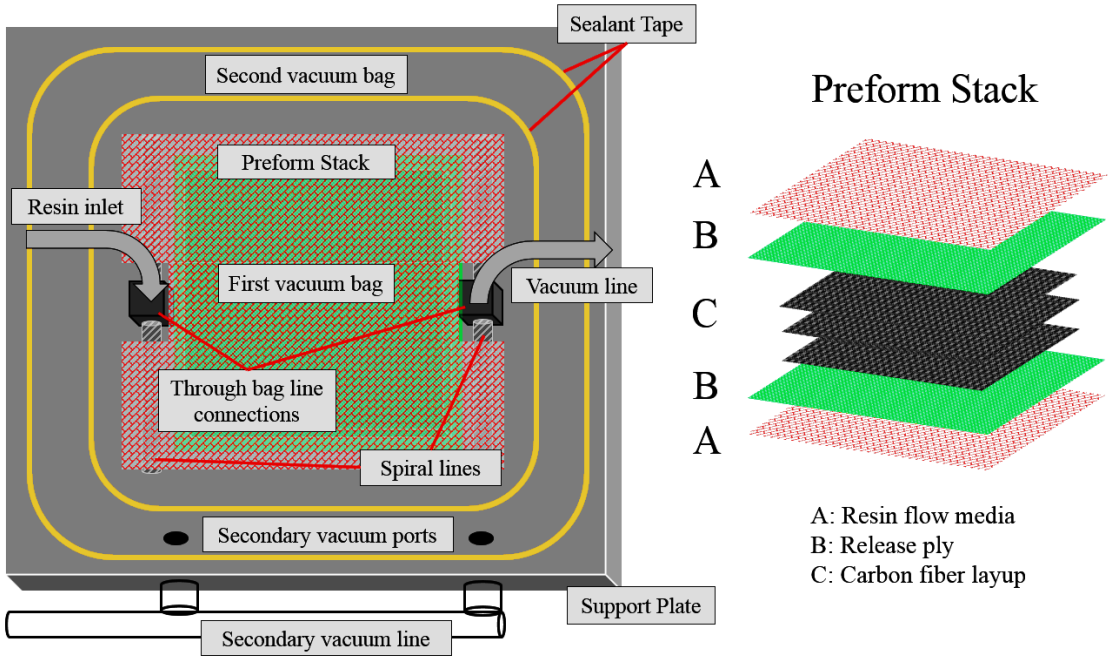

Figure 51: (left) a diagram of the VARTM system with components labeled and (right) an expanded view of the preform stack.

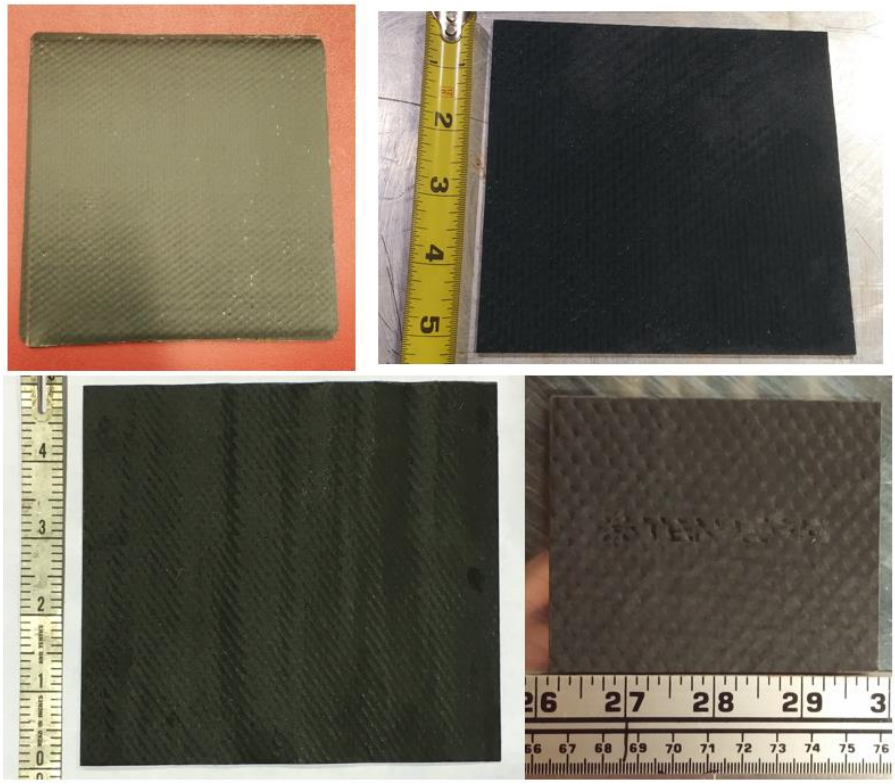

Figure 52: Four examples of produced composites using the VARTM technique.

VITA

Nathan Meek was born in Denver, CO on September 6th, 1990 to John Meek and Kristen Iversen and has one brother, Sean Meek. He spent his younger years in Golden and Littleton, CO before moving to San Jose for 3 years during middle school and then Memphis for high school. Nathan graduated from White Station High School with honors and advance placement. Beginning in 2008, he started his collegiate career at the University of Tennessee in Material Science and Engineering. Nathan started working in research for Dr. Dayakar Penumadu beginning in his sophomore year on microwave expansion of polystyrene. After graduating from his undergrad, he elected to pursue a master's with Dr. Penumadu in the development and characterization of lignin carbon fiber and production of composite materials, which he finished in 2016. This master's program focused on working with the Center for Renewable Carbon to characterize carbon fibers and refine chemical/manufacturing processes to produce high performance carbon fiber. On weekend he is often outdoors, at the gym, or woodworking.